Doctor of Philosophy Dissertation

Interaction-based nonlinear quantum metrology with a cold atomic ensemble

Author:
Mario Napolitano

Supervisor:
Morgan W. Mitchell

Institut de Ciències Fotòniques (ICFO)

Universitat Politècnica de Catalunya

No, what is important is neither linearity or non-linearity,
but the change, the degree of change
from something that doesn't move
to other events with different tempos in particular.

— Karlheinz Stockhausen, 1928 - 2007
German composer
a pioneer of electronic music

Abstract

In this manuscript we present an experimental and theoretical investigation of quantum-noise-limited measurement by nonlinear interferometry, or from another perspective, quantum-noise-limited interaction-based measurement. The experimental work is performed using a polarization-based quantum interface between propagating light pulses and cold rubidium-87 atoms trapped in an optical dipole trap.

We first review the theory of quantum metrology and estimation theory, and we describe theoretical proposals for nonlinear quantum metrology as developed by the group of Carlton M. Caves in the University of New Mexico.

We then describe our proposal, made in 2010, to implement the Caves group's ideas using nonlinear optical interactions in a cold atomic ensemble to implement a nonlinear spin measurement. To evaluate this proposal we develop two theoretical approaches, first an extension of the collective quantum variables approach, often employed to describe quantum interfaces and atomic spin ensembles, to nonlinear optical processes. This results in an effective Hamiltonian containing nonlinear terms of the form described by the Caves group, and demonstrates a qualitative equivalence of the two schemes. The second approach uses the Maxwell-Bloch equations to describe nonlinear propagation of pulses through an atomic spin ensemble, including inhomogeneities and relaxation effects. This latter method makes quantitative predictions about optical rotation signals under realistic experimental conditions.

We then describe the implementation of the proposal in a polarization-based light-atom quantum interface. We describe

the existing trapping and probing system, focusing on the characteristics that make it suitable for shot-noise-limited and projection -noise-limited atomic spin measurements. We then describe adaptations to use the apparatus with shorter, higher-intensity pulses as required for nonlinear measurement, as well as characterization of the photodetection system under these modified conditions. Calibration of the nonlinear polarization rotation versus probe laser detuning allows us to produce a nearly pure nonlinear rotation signal. Finally, experimental results are presented showing shot-noise-limited nonlinear rotation signals over three orders of magnitude in photon number N. The results are consistent with our theoretical models and confirm a major prediction of the Caves group's work, in that a two-photon interaction gives a scaling for the measurement sensitivity as $N^{-3/2}$.

A brief discussion relates this experimental observation to theoretical discussions of the "Heiseinberg limit" of quantum metrology, and possible further applications of nonlinear measurement techniques.

Resum

En aquest manuscrit presentem una recerca experimental i teòrica sobre mesures limitades pel soroll quàntic fetes mitjançant interferometria no lineal, o des de un altra perspectiva, mitjançant interacció. En el treball experimental es va fer servir una interfície quàntica de polarització entre polsos de llum en propagació i àtoms freds de rubidi-87 atrapats en una trampa òptica de dipol.

Primer, farem un repàs de la teoria de la metrologia quàntica i de la teoria de la estimació, descriurem la proposició teòrica sobre metrologia quàntica no lineal tal i com la va desenvolupar el grup de Carlton M. Caves al Universitat de Nou Mèxic.

A continuació descriurem la nostra proposta, feta al 2010, de com implantar la idea del grup de Caves fent servir interaccions òptiques no lineals en un conjunt d'àtoms freds amb la finalitat d'efectuar una mesura no lineal de spin. Per avaluar aquesta proposta vam desenvolupar dues aproximacions teòriques fent ús de dos mètodes diferents. En primer lloc vam estendre la tècnica de variables quàntiques col·lectives cap als processos òptics no lineals, aquesta tècnica sovint és utilitzada per descriure interfícies quàntiques i conjunts de spin atòmics. Això dóna com a resultat un Hamiltonià efectiu que conté termes no lineals de la forma descrita pel grup de Caves, i demostra una equivalència qualitativa entre el nostre esquema i el seu.

El segon mètode fa ús de les equacions de Maxwell-Bloch per descriure la propagació no lineal dels polsos a través del conjunt de spins atòmics, tenint en compte deshomogeneïtats i efectes de relaxació. D'aquesta manera podem fer prediccions quantitatives sobre senyals de rotació de polarització òptica en les condicions d'un experiment real.

Seguirem amb la descripció de com vam implementar al laboratori la nostra proposta teòrica mitjançant una interfície quàntica de polarització entre llum i àtoms. Descriurem el ja existent sistema de confinament i sondeig dels àtoms, concentrant-nos en les característiques que permeten fer mesures al limit del soroll quàntic i del soroll de projecció. Aleshores detallarem com vam adaptar el sistema per l'ús amb polsos més curts i intensos, tal i com requereix la mesura no lineal, i al mateix temps com vam calibrar el sistema de detecció de llum en aquestes diferents condicions. El calibratge de la rotació no lineal de polarització en funció de la freqüència del làser de sonda, ens permet obtenir un senyal de rotació casi purament no lineal. Finalment, presentarem els resultats experimentals que mostren senyals de rotació no lineal limitats pel soroll quàntic al llarg de tres ordres de magnitud en el número N de fotons. Tals resultats son consistents amb els nostres models teòrics i confirmen una important predicció del treball del grup de Caves, és a dir que la interacció de dos fotons dóna una llei d'escala de $N^{-3/2}$ per a la sensibilitat de la mesura.

Per concloure, una concisa discussió relaciona aquesta observació experimental amb discussions teòriques sobre el "limit d'Heisenberg" de la metrologia quàntica, i amb d'altres possibles aplicacions de tècniques de mesura no lineal.

Acknowledgments

Many people helped me during the years of my doctorate and they deserve all my gratitude.

I would like to thank Morgan for his advise, his trust in me and my work, his constant presence and availability for resolving doubts or problems, his meticulous sessions of talk rehearsal. He is a clever scientist, a genuine leader and an empathetic person, a very rare combination of characteristics. I appreciated and always remember all the conversations with him on the way from Barcelona to Castelldefels and back. I hope many more thesis supervisors would be like him.

I had the luck to share office and lab with fantastic fellows: the ones in my beginning Marcin, Marco, Ana, Sebastian, Brice and the latest ones Rob, Naeimeh, Giorgio, Ferran. As well as all the friends from the light lab Florian, Ale, Fede, Gianvito, Yannick, Joanna, Silvana and all the summer students and visitors which joined our group for a short period. I learnt a lot from all of you, and really enjoyed the time spent together, both at ICFO and outside.

ICFO is a great place to work because there are great persons working there. Thanks to all the researchers, students and professors who I met. In particular to all the fellows of the quantum journal club, who periodically hated me when I was asking to them about the next paper to present. A big thanks to all the members of Jurgen's group first and Hugues' group next, with whom I shared expertise and equipment. It was a great pleasure.

Thanks also to all ICFO technicians and management stuff. For sure without them my research at ICFO would have take twice the time it took.

De les persones conegudes al ICFO, un agraïment particular el vull fer al Marc, company de molts viatges i qui va ser a introduir-me als castellers de Sant Cugat, cosa que sense dubte m'ha canviat la vida. Crec que durant els nostres quotidians dinars amb l'Andreu vam tocar tots els temes, coneguts i desconeguts, de l'activitat castellera. Va ser una passada.

Un agraïment també a tots els amics i companys de Sant Cugat, que sempre em van animar sobretot durant la escriptura de la tesis. E un grazie enorme agli amici italiani a Barcellona: Annalisa, Claudia e Alex, i compagni del gruppo di musica, Roberto e Angela nei primi tempi a Barcellona. Grazie a tutti.

Per finire un ringraziamento all'appoggio incondizionato della famiglia napoletana, mamma e Pierpaolo in primis, appoggio che si è fatto sentire anche da lontano.

I gràcies a la Sole, que sempre sap trobar la forma de fer-me somriure. T'estimo.

Contents

Abstract 5

Acknowledgments 9

Chapter 1. Background on Quantum Metrology 13
1.1. Basic vocabulary 13
1.2. The quantum interferometer 15
1.3. From Standard Quantum Limit to Heisenberg Limit: entanglement 19
1.4. Some applications 24

Chapter 2. The formalism of nonlinear quantum parameter estimation 29
2.1. Estimation via estimators and their performance 30
2.2. Extending estimation theory by using quantum mechanics 34
2.3. QCRB and transformation generators 36
2.4. Composite probe system and the role of system size 37
2.5. Nonlinear Hamiltonian 39
2.6. Proposed implementations 41

Chapter 3. Nonlinear light-atom quantum interface 45
3.1. Collective variables for light-atom quantum interfaces 45
3.2. Stokes operators for light polarization 47
3.3. Spin variables for atomic ensembles 51
3.4. Tensorial polarizability Hamiltonian: the linear case 56
3.5. Degenerate perturbation theory for higher order interactions 60
3.6. Quantum Noise 65

Chapter 4. Numerical Simulations 69
4.1. Mechanisms of polarization rotation: Maxwell-Bloch equations 70
4.2. Single-atom master equation 74
4.3. A simple example 77
4.4. Steps and pulse dynamics 78
4.5. Simulating the nonlinear probing 82
4.6. Damage and nonlinearity 84
4.7. Geometrical mode-matching 87

Chapter 5. Experimental setup 93
5.1. Description of cold-atom machine 94
5.2. Probing the atoms via rotation of light polarization 96
5.3. Measuring the sample OD 101
5.4. Looking for the magic detuning 104
5.5. Shot-noise-limited detection 106
5.6. Optical pumping for atomic-state initialization 107

Chapter 6. Testing the nonlinear probe in an experiment 115
6.1. Calibration by sensing the same quantity 115
6.2. Calculating the sensitivity scaling 120
6.3. Comparison to the theoretical model 121
6.4. Excluding other sources of nonlinearity 123
6.5. Sensitivity comparison, a scenario-dependent issue 124

Conclusions and perspectives 127

Bibliography 131

List of publications 141

CHAPTER 1

Background on Quantum Metrology

Metrology is that part of science concerned with measurements. The interest in measurement has both a theoretical origin, because of the question about what is the fundamental meaning of performing a measurement, and a technological relevance since it will lead to improve instrumentation performances and standards.

In the context of quantum physics, quantum metrology develops high-resolution and highly sensitive measurements of parameters using quantum theory to describe the physical systems, and in particular exploiting quantum entanglement. The declared aim of quantum metrology is to develop new measurement techniques that provide better precision than the same measurements performed by classical means.

In this chapter we will introduce the key elements of this area of physics, how they interplay and what is the commonly used approach to improve the quality of the measurements.

1.1. Basic vocabulary

The man-in-the-street idea of performing a measurement is the following: there is a quantity that needs to be measured, e.g., the temperature of an object. Somebody is provided with an instrument that responds in someway to temperature, e.g., a thermometer. This somebody puts the instrument in contact with the object under measurement, and reads-out how the instrument, in particular some of its properties have been modified by the contact. From this read-out and some knowledge about the instrument, the person can infer the object's temperature.

This scheme is valid for the majority of measurements: there is an object of which we would like to measure a specific property.

We can refer to them as the *system* and its *parameter*, χ. Then, we have the measuring instrument, we call it the *probe*. The probe will *interact* with the system during some time and it will collect so some information about the parameter. Finally we can observe the probe, learn how it has evolved during the interaction and *estimate* the parameter.

The estimation process is typically not perfect, so that we will know the parameter with an error. It is better to say that we can have a *best guess* of the parameter, $\overline{\chi}$ and an *uncertainty*, $\Delta\chi$.

Imperfection has different origins. Measurements could be affected by systematic errors, e.g., a badly calibrated instrument was in use, or by statistical ones. We can refer to this random contribution as the *noise*. The noise can be present in the knowledge of the *state* of the probe, ρ_{probe}, i.e., the set of elements and quantities that defines the condition of the probe. Moreover, noise can play a role also at the stage of the interaction between the probe and the system, because of unknown, or not under control, mechanisms, e.g., how the room temperature affects the thermometer while it is measuring.

It is crucial to make a distinction between sources of noise. The sources of noise that are technical in principle can be minimized and avoided, while the ones that are fundamental come from physical principles, and can not be avoided. We will see this better in the following, in fact quantum metrology focuses on these fundamental sources of noise.

Finally we introduce the *sensitivity*, $\delta\chi$, which is a figure-of-merit of the estimation process: it is the a priori minimum uncertainty one can expect to have in the estimation process under consideration. The estimation will not give conclusive answer if intended for example to distinguish quantities which differ less than $\delta\chi$, and a better estimation technique should be used instead.

We are going to present all these concepts in the framework of interferometry as this technique is universally recognized as the ideal benchmark for studying quantum effects of metrological relevance [Hariharan and Sanders, 1996].

1.2. The quantum interferometer

Interferometry is a very powerful technique for performing measurements. It uses the principle of superposition to combine two waves and extract relative information regarding the difference between separate paths before the recombination. This is possible since the result of the superposition of two waves with the same frequency is determined by the phase difference between them:

(1.2.1)

$$\sin(\omega t+\phi_1)+\sin(\omega t+\phi_2) = 2\sin\left(\omega t+\frac{\phi_1+\phi_2}{2}\right)\cos(\phi_1-\phi_2).$$

Interferometers are widely used in science and industry for the measurement of small displacements, changes of refractive index [Woodruff and Yeung, 1982], surface irregularities [Barker, 1972; Heslehurst, 2009; Maji, 1995], etc. All these are examples of physical processes which induce a relative phase, ϕ, in the waves of the electromagnetic field. This phase shift can be measured relatively to a reference beam, as in a Mach-Zehnder (MZ) interferometer.

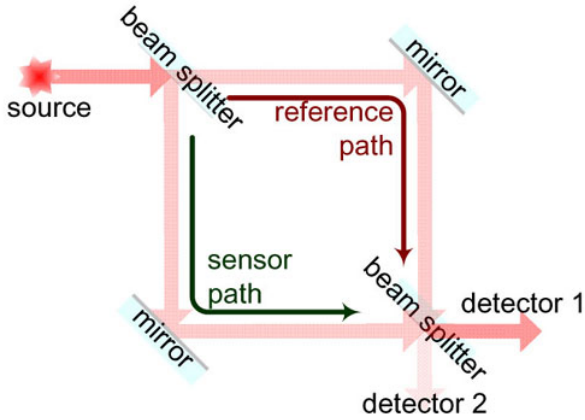

Figure 1.2.1. Mach-Zehnder interferometer.
Figure from an article in SPIE Newsroom by Martin *et al.*
doi:10.1117/2.1200610.0413

Quantum mechanics is of the uttermost relevance in interferometry, principally because of two reasons. The first is that to sense smaller and smaller quantities, a point will arrive where the elements of the interferometers show their quantumness: to give an example, in a gravitational-wave antenna, where displacements below 10^{-18} m matter, the interpretation of radiation pressure on the mirrors in the interferometer must include the fact that light is made of quanta, i.e., the photons, whose bouncing on the mirror surface has an intrinsic quantum randomness [Caves, 1980].

The second reason is more generic, and concerns the fact that every system is quantum in its nature. Unfortunately we are not used to such a vision and we do not worry about the quantum nature of the probes used to perform interferometric measurements, since the interference phenomena we commonly experience involve light, sound, radio signals, which evidently are waves. Conversely, there are interferometers which work with particles, atoms for example, as probes [Baudon et al., 1999; Cronin et al., 2009]. The wave-like behavior of atoms only can be understood in the framework of the wave-particle duality, which is at the basis of the quantum interpretation of microscopic objects.

Before proceeding, we need to clarify some more details about the terminology: in the vocabulary of quantum physics a *measurement* is a very specific process with a precise mathematical definition, which involves operations on Hilbert spaces. There is a correspondence between measurable quantities, i.e., observables like velocity, angular momentum, energy, etc., and Hermitian operators. The results of a measurement process are tied to the spectrum of its corresponding operator. A real process, e.g., the detection of photons by a photodetector with some level of electronic noise and dark counts, has its corresponding mathematical positive-operator-valued-measure (POVM) [Helstrom, 1976].

In this framework, we stress the difference between the *measurement* a user performs on the quantum probe after the interaction with the system under investigation, and the whole *estimation* process. Once this clarification has been made, I

want to apologize in advance for confusion in the usage of these two terms that the reader may find in the rest of the thesis, confusion originated by the similarity of the two notions in the common, classical, language.

Let us consider the wave-particle duality and analyze under this perspective an interferometer where a quantum system is used as the probing element. We can refer to such a device as a quantum interferometer.

We need to know, or we have to set, the initial state of the probe, $\rho(0)$, before the interaction with whatever system is the object of the estimation, even before the probe is sent into the input port of the interferometer. One pillar of quantum physics is the well known Heisenberg uncertainty principle: it says that specific sets of observable quantities can not be known simultaneously with infinite precision [Heisenberg, 1927; Robertson, 1929]. As a consequence it is possible that the initial state of the probe has a level of uncertainty, which is a source of noise eventually.

More in detail, if we think of the probe as an ensemble of N particles, the splitting into the two arms will lead to a binomial distribution so that the particles in each arm will be distributed around the mean value, $\overline{n}$, within an interval of size δn, with

$$\overline{n} = N/2 \quad \text{and} \quad \delta n = \sqrt{N}/2, \tag{1.2.2}$$

in case of having a 50:50 beam splitter at the input port. An alternative interpretation makes use of the quantum fluctuation of the electromagnetic field. Although no light is injected into the interferometer from the port opposite the one where the probe enters, there are vacuum fluctuations incident from this direction. They are responsible for the uncertainty $\delta n = \sqrt{N}/2$ in the distributions of particles in the two arms.

In the two arms of the interferometer, the wave behavior of the probe plays a role, and in the sensing arm the probe acquires a phase difference with respect to the reference one, exactly as in the classical case. The heart of what happens in the sensing arm is the interaction with the system under estimation, which can be formalized in the following way: let us assume an interaction Hamiltonian, $\hat{H}$, where the system parameter to

estimate, χ, is multiplied by an operator, or by a function of operators, describing observables of the probe system, $\hat{\mathcal{O}}$,

$$\hat{H} = \chi\hat{\mathcal{O}}. \tag{1.2.3}$$

This interaction, acting for an interval of time t, will evolve the probe state in this arm[1], through a unitary evolution operator $\hat{U} = e^{i\hat{H}t/\hbar}$.

Finally the two arms recombine and one should proceed to measure the final state of the probe system, in most of the cases by measuring the intensity in the two output arms. We can now think at the probe in the particle-like fashion because measuring intensity is very close to count the number of particles. The time arrival of photons on a detector is a random process following Poissonian statistics. Consequently, in any set of measurements there will be the following relation between the mean value of the number of photon counted, $\mu = \overline{n}$, and the uncertainty, calculated as the square root of the variance, $\delta n = \sqrt{\overline{n}}$.

All the processes described above that introduced uncertainty and imperfection in the interferometer are somehow fundamental, i.e. it is not for being an imperfect beam-splitter that the splitting process is more random than one would desire. We see that all this randomness follow the same square-root law, $\sqrt{N}$: in electronic this is something known as shot-noise, coming directly from the quantization of charge [Schottky, 1918].

From the shot-noise contribution to fundamental imperfection, we can calculate the sensitivity in the estimation of the phase, which finally sets the sensitivity in the estimation of the parameter χ. If N is the total number of particles and n_1, n_2 are the counts at the two output ports of the interferometer, then considering eq. 1.2.2 we have:

$$\overline{\phi} \propto \frac{n_1 - n_2}{N} \quad \text{and} \quad \delta\phi \propto \frac{\sqrt{N}}{N} = N^{-1/2}. \tag{1.2.4}$$

[1]The partition of the probe state can be more involved than simply identifying a sub-state in each arm. Indeed this is what entanglement vs. separability is about, that is a very important issue. Anyway, the details of this question are irrelevant at this point, where the goal is formalizing the effect of the external system.

Consequently, $\delta\chi$ will also scale as $N^{-1/2}$. This scaling law of the sensitivity with the number of particles is known as the Standard Quantum Limit (SQL) of parameter estimation [Braginsky and Khalili, 1992; Caves, 1985; Ozawa, 1988; Yuen, 1983].

1.3. From Standard Quantum Limit to Heisenberg Limit: entanglement

Another way of seeing the rise of fundamental uncertainties in metrology is through the Heisenberg uncertainty principle. In the majority of the cases, the principle avoids the full knowledge of the state of a quantum system. As a consequence, the setting of the initial state of a quantum probe has some level of uncertainty, and also the comparison between the probe state before and after the interaction cannot be complete, facts these that add some level of randomness to the estimation.

However, by using statistics we can make improvements: instead of one single probe, we can use N identical, independent probes, measure them, and average the results. According to the central limit theorem, for a large value of N, the error on the average decreases as $\Delta/\sqrt{N}$, where Δ^2 is the variance of the measurement results associated with each individual probe. Once again we find the SQL square root scaling law [Giovannetti et al., 2006].

We can show this in an example where the N probes are photons. Let us introduce a and $a^\dagger$ as the annihilation and creation operators for the optical mode A, and a similar notation for the other modes in Fig. 1.3.1

The beam-splitter transformations for annihilation operators, e.g., at the input port in Fig. 1.3.1, are the following:

$$a' = \frac{a + ib}{\sqrt{2}}, \quad b' = \frac{ia + b}{\sqrt{2}}. \tag{1.3.1}$$

Accounting also the relative phase ϕ acquired between the arms A' and B', we have for the output modes of the whole interferometer:

$$\begin{aligned} c = \frac{a' + ib'e^{i\phi}}{\sqrt{2}} &= a\frac{1 - e^{i\phi}}{2} + ib\frac{1 + e^{i\phi}}{2} = \\ &= -ie^{i\phi/2}\left[a\sin(\phi/2) - b\cos(\phi/2)\right] \end{aligned} \tag{1.3.2}$$

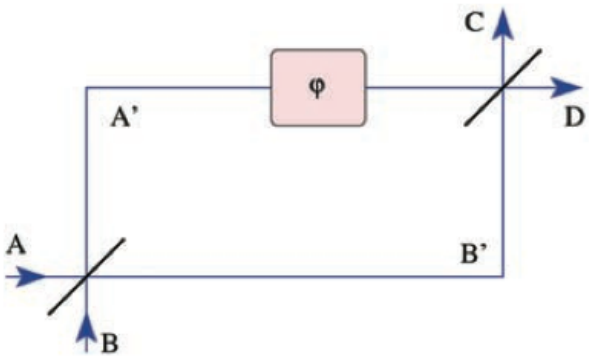

Figure 1.3.1. MZ interferometer. From an article by Giovannetti [Giovannetti, 2004]. The modes entering and exiting the beam splitter are labeled; a phase difference ϕ, encoding the signal to estimate, accumulates between the two arms.

and

$$d = \frac{ia' + b'e^{i\phi}}{\sqrt{2}} = ia\frac{1+e^{i\phi}}{2} - b\frac{1-e^{i\phi}}{2} = \\ = ie^{i\phi/2}\left[a\cos(\phi/2) + b\sin(\phi/2)\right]. \tag{1.3.3}$$

For the creation operators we have:

$$c^\dagger = ie^{-i\phi/2}\left[a^\dagger \sin(\phi/2) - b^\dagger \cos(\phi/2)\right], \tag{1.3.4}$$

$$d^\dagger = -ie^{-i\phi/2}\left[a^\dagger \cos(\phi/2) + b^\dagger \sin(\phi/2)\right]. \tag{1.3.5}$$

The intensity difference of the two output ports, corresponding to the operator

$$\hat{M} = d^\dagger d - c^\dagger c = \left(a^\dagger a - b^\dagger b\right)\cos\phi + \left(a^\dagger b - b^\dagger a\right)\sin\phi, \tag{1.3.6}$$

is the observable that is monitored for the read-out in estimating ϕ.

A photonic system can be described in different representations of states [Scully and Zubairy, 1997]: among the most

usual ones there are the Fock states, i.e., states with a well defined photon number. The vacuum state or the single-photon state are some examples.

Also very well used there are the coherent states, i.e., states with a well defined phase relation in the sinusoidal oscillation of the electromagnetic field. They are the most close description of the field coming out of a laser.

Both of those sets are a basis for the Hilbert space of a photonic mode meaning that every other state can be expressed via linear combination.

For the case of a Fock state with N photons entering into port A and vacuum in mode B, i.e., $\left|\psi^{(\text{in})}\right\rangle = \left|N\right\rangle_A \left|0\right\rangle_B$, we have:

$$\langle \hat{M} \rangle = N \cos\phi, \tag{1.3.7}$$

$$\text{var}(\hat{M}) = (\delta M)^2 = \langle \hat{M}^2 \rangle - \langle \hat{M} \rangle^2 = N \sin^2\phi. \tag{1.3.8}$$

Performing error propagation we calculate the sensitivity in the phase estimation to be:

$$\delta\phi = \delta M \left| \frac{\partial \langle \hat{M} \rangle}{\partial \phi} \right|^{-1} = \frac{1}{\sqrt{N}}, \tag{1.3.9}$$

that is the expected SQL.

Exactly the same will happen if instead of a Fock state we send a coherent state $|\alpha\rangle$ into port A, with $|\alpha|^2$ being the mean photon number N.

Now let us consider that we are able to manipulate the set of photons so that they are not independent anymore. The uncertainty they carry may probably not sum up in a trivial way because their fluctuations can be correlated. This is indeed what happens if collectively the N probes are in an initial entangled state. We can show that this leads to an enhancement in the sensitivity.

A possible entangled initial state can be the following:

$$\left|\psi^{(\text{in})}\right\rangle = \frac{1}{\sqrt{2}} \left(\left|N+1\right\rangle_A \left|N\right\rangle_B + \left|N\right\rangle_A \left|N+1\right\rangle_B \right). \tag{1.3.10}$$

This is a nonclassical state, with correlations between the inputs A and B modes that cannot be described by a local statistical model.

With this kind of states we have [Dowling, 1998]:

$$\langle \hat{M} \rangle = (N+1)\sin\phi, \tag{1.3.11}$$

$$\mathrm{var}(\hat{M}) = \cos(2\phi) + (N+1)^2 \sin^2\phi \tag{1.3.12}$$

and at least for small angles, using the same propagation error rules as before, one can easy calculate the sensitivity

$$\delta\phi|_{\phi=0} = \frac{1}{N}. \tag{1.3.13}$$

We can see that the sensitivity gains a square root factor more than in the SQL case. Such a sensitivity achievable with entanglement is known in the field as the Heisenberg limit (HL). To be specific, sometimes in the literature there is ambiguity about if the HL is referred to a particular value function of N, or only to the scaling law, i.e., the exponent -1 of N in contrast with the $-1/2$ of the SQL. Nowadays, the debate about an exact definition of the HL is still open [Zwierz et al., 2010, 2012; Hall et al., 2012; Hall and Wiseman, 2012; Berry et al., 2012].

The term HL was introduced during the nineties decade [Holland and Burnett, 1993; Lane et al., 1993; Sanders and Milburn, 1995; Ou, 1996], and the relation with the uncertainty principle was explained in terms of the relation between fluctuation in phase and photon number [Dirac, 1927]:

$$\Delta\phi\Delta n \geq 1 \tag{1.3.14}$$

In the original works it was clearly stated that the HL is not derivable directly from the uncertainty principle, because of the ambiguity in the definition of a phase operator from which deriving the relation (1.3.14) [Carruthers and Nieto, 1968; Dirac, 1927; Louisell, 1963; Pegg and Barnett, 1988; Torgerson and Mandel, 1996; Vorontsov and Rembovsky, 1999]. Nevertheless, outside the quantum metrology community the terms Heisenberg limit and uncertainty principle were mixed, confusion that helped in consolidating the idea for which the HL is the ultimate

limit for sensitive interferometric measurements. One of the results of this thesis is, in fact, the experimental demonstration that things are not as simple as that.

$1/N$ scaling would also be achieved if in the MZ interferometer the input beam-splitter is replaced with a device capable of preparing the highly entangled state

$$\frac{1}{\sqrt{2}}\left(|N\rangle_{A'}|0\rangle_{B'} + |0\rangle_{A'}|N\rangle_{B'}\right). \tag{1.3.15}$$

This kind of states are known as $N00N$ states and are very difficult to generate but even more difficult to preserve, since any small scattering event in one of the two modes can reveal the presence there of the photons and so make collapsing the wave-function onto a non-entangled state.

The experimental creation of the particular 2-$N00N$ state, sometime called a *diphoton*, is commonly performed with a two photons interference effect as in the seminal experiment by Hong, Ou and Mandel [Hong et al., 1987]. When two indistinguishable photons, usually generated with nonlinear optics techniques, reach a beamsplitter exactly at the same time, they join, i.e., the possibility of they exiting the beam splitter on different ports suffers destructive interference, because of the bosonic nature of photons. So the final state will be a superposition of both photons in one arm with both photons in the other arm.

$N00N$ states were proposed for improving the resolution in the context of lithography [Boto et al., 2000] because of the peculiar correlations among photons, in particular about their coincidence in the arrival time onto the target. In the context of metrology the same concept is applicable: using $N00N$ states the coincidence signal at the two outputs of an interferometer has N times faster dependance with ϕ, than in the case of the read-out of $\hat{M}$ with non-entangled state, boosting in such a way the sensitivity towards the Heisenberg limit.

Another way to improve on top of the SQL is manipulating the mode in the B port of the interferometer sending there what is known as a squeezed state, instead of leaving only the vacuum. The description of squeezed states can be found in any textbook of quantum optics [Scully and Zubairy, 1997; Bachor and Ralph, 2004; Loudon, 1983], and their use in metrology is widespread.

Also for squeezed states, improving on top of the SQL means using nonclassical resources. Squeezing is a feature of the macroscopic description of the whole ensemble of probes, while entanglement describes nonclassicality at the microscopic level. The two descriptions have been theoretically tied, before in the case of atomic systems [Sorensen and Mølmer, 2001] and recently also in the photonic case [Beduini and Mitchell, 2013].

1.4. Some applications

The research in quantum metrology during the last decades, in particular in the area of quantum optics or atomic physics, allowed to boost the performance in terms of sensitivity of many measurements. Here are some examples.

1.4.1. Gravitational antennas. Gravitational wave detection is one of those fields where the signals are expected to be incredibly small compared with the usual sources of noise. The distortion in space-time caused by a big astronomical event, e.g., a supernova exploding or two black-holes colliding, is expected to be of the order of 10^{-18} m. Laser interferometry starts to become a plausible option but only when used inside kilometer long arms. Interferometers of this size has been built in Italy, USA, Germany and Japan.

The geometry is the Michelson one (see Fig. 1.4.1), and usually the laser light is recycled in the long arms using cavities to boost the power up to hundred of Watts reducing in this way the effects of the photon shot-noise. The counterpart is that this huge power on the massive sensing mirrors creates problems because of thermal deformation of the surfaces and because of radiation pressure. An optimal power is thus found balancing these effects. This is the origin of standard quantum limit in this field. It was proposed [Caves, 1981] and has been recently demonstrated [The Ligo Scientific Collaboration, 2011] that squeezed light improves the sensitivity of such devices.

1.4.2. Time standards. Atoms have definite features that only depend on physical constants. One of these features, the electronic structure, can indeed be used as a reference for energy,

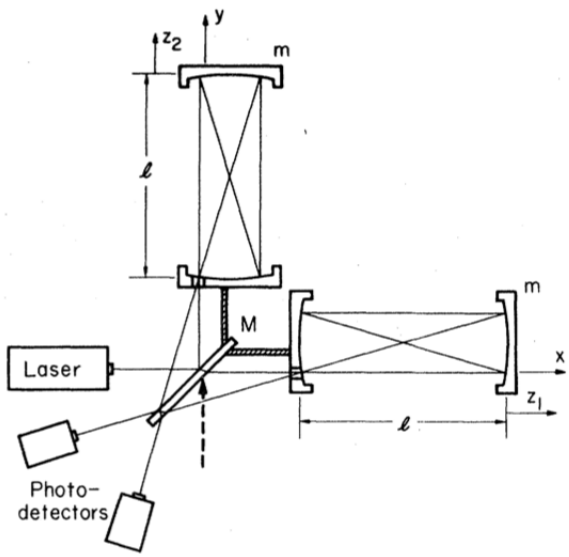

Figure 1.4.1. Michelson interferometer used for gravitational-wave detection. From the article by Caves about radiation pressure in interferometers [Caves, 1980]. In the two long arms there are recycling cavities. The dashed arrow is the unused port from into which squeezed light is injected.

and consequently for frequency, thanks to Planck's relation between energy and frequency, $E = h\nu$. This is at the heart of the modern atomic clocks for time standards.

The atomic interferometer [Essen and Parry, 1955; Sullivan, 2001] used for time standards works in the following way: an ensemble of atoms, the probe, is initialized in a specific energy level. A microwave pulse split the atoms sending half of them into a different energy state. Just after the splitting, the two ensembles have a definite phase relation specified by the phase of the microwave. This process is known as a $Pi/2$ pulse and it is the analogous of a beam splitter for photons.

The free evolution of the ensembles in the two different energy levels generates a phase difference $\Delta\phi = t(E_2 - E_1)/\hbar$ proportional to the time passing, t. Finally, a second $Pi/2$ pulse

recombines the ensembles and by counting the population difference between level 1 and 2, similarly to what is done in the optical case for the operator $\hat{M}$, one can read out the phase, and indirectly t.

This technique is called Ramsey interferometry, and its formalism is exactly the same as in the case of a photonic MZ. There are techniques, which are used to extend as much as possible the time between the two pulses, e.g. atomic fountain.

Another category of atomic interferometry uses the recoil got while scattering photons, for example in Raman processes, as a technique to split spatially the free falling wave-packet of atoms [Bordé, 1989; Kasevich and Chu, 1991]. With these recoil techniques the atomic beam can be also reflected, as photons from mirrors. In such interferometers where the arms are physically separated, atoms can experience gradient of forces, acceleration, etc.

1.4.3. Magnetometry. Some atomic species, alkali atoms for example, also are very good in probing magnetic fields, because of their dipole moment and spin. Ramsey technique can reveal the effect of magnetic field on atomic ensembles, but interferometry also plays a role in this kind of applications in the optical read-out of atomic properties, like the angular momentum of the atomic sensors.

In optical magnetometers the probing mechanism is the following: a magnetic field affects the angular momentum of a cloud of atoms, which can affect in turn light properties, e.g., polarization. A polarization interferometer uses a rotation of the polarization plane of an optical field, which can be interpreted as a phase shift introduced by a medium between two orthogonal circular components. This effect is usually known as Faraday rotation, when related to magnetic fields.

Squeezing in light polarization [Korolkova et al., 2002] has been demonstrated to be useful for improving sensitivity to magnetic field [Wolfgramm et al., 2010], as well as $N00N$ states and their induced super resolution [Wolfgramm et al., 2013]. Entanglement, in particular spin-squeezing [Kitagawa and Ueda, 1993], can also improve on the atomic side, since the precession

caused by the magnetic field can be resolved better if the quantum fluctuations are reduced in particular components of the angular momentum.

CHAPTER 2

The formalism of nonlinear quantum parameter estimation

In the previous chapter we introduced the basic ingredients of quantum metrology, i.e., the probe, the parameter, the sensitivity, and presented the Heisenberg limit, which ties the minimum detectable phase shift to the inverse of the number of probe particles N, or, equivalently to the inverse of the energy/resources employed in the probing process.

As already mentioned, there was some ambiguity about the definition of the Heisenberg limit, if it was stated in terms of a specific value [Holland and Burnett, 1993; Sanders and Milburn, 1995; Pezzé and Smerzi, 2008] or a scaling-law [Braunstein, 1994; D'Ariano and Paris, 1994; Luis, 2004; Giovannetti et al., 2006; Dorner et al., 2009]. Regardless of this ambiguity in the definition, there was the generalized idea that the Heisenberg limit was the ultimate bound to the precision of a measurement. Even if considered just as a scaling-law, it was thought to be the best possible scaling-law achievable.

In this chapter we will present the proposals that first introduced a different point of view about the hunting for ultimate limits in sensitivity. The group of professor Carton Caves at the University of New Mexico developed the new hypothesis that statements such as "the Heisenberg limit is the ultimate bound" apply only when the estimation is restricted to *linear* phase shifts, i.e., when the generator of the transformation, encoding the signal into the probe, is proportional to the probe-particle number operator.

They argued that other estimation strategies, which instead encode the signal via a *nonlinear* transformation, have quantum limits with a significantly different dependence on the number

of particles. We will see how for nonlinear transformations the uncertainty decreases with probe number more favorably than the rate established by the Heisenberg limit, even when using semiclassical input states.

Their arguments were about sensitivity scaling: other things equal, a scheme that scales as N^{-2} should in the long-term be attractive because, by increasing N, it will eventually outperform a scheme scaling as N^{-1}, regardless of the pre-factor.

For correctness, before the first article about overcoming the Heisenberg limit was published in 2007 by the group in New Mexico [Boixo et al., 2007], the use of nonlinearity for improved sensitivity was already spreading in the quantum metrology community. In particular, it is worth to mention the first works of professor Alfredo Luis at the Complutense University of Madrid, which were been published since 2004 [Luis, 2004; Beltrán and Luis, 2005; Luis, 2007].

We will start the chapter recalling the universally known formalism of parameter estimation and its quantum extension, and in this way introduce the concepts used in the articles by Caves and coworker. Then, we will present their argument, mentioning finally some possible experimental implementations, which the scientific community has proposed in the last years. Our proposal of experimental implementation is instead the topic of the next chapter.

In the next two sections I do not present anything new, I will just present what I think are the most useful points, for the understanding of this thesis, of a very well structured formalism: the theory of quantum parameter estimation [Helstrom, 1976; Holevo, 1982; Yuen and Lax, 1973; Helstrom and Kennedy, 1974; Braunstein and Caves, 1994; Braunstein et al., 1996].

2.1. Estimation via estimators and their performance

When up to now we were referring generically to uncertainty, precision and finally sensitivity, we were thinking about the very basic idea in experimental sciences that measurements are affected by errors. Let us now be slightly more formal and introduce the correct concepts to be used for dealing with sensitivity in the framework of quantum metrology.

Let us consider a very easy classical example. We have a quantity we want to estimate, let say the weight of a person, χ. We know that there is an instrument sensitive to this quantity, the balance. We perform a measurement using such an instrument and get an outcome, x, but since we have been told, by someone very wise, that measurements are noisy processes, we do not trust a single measurement and so we repeat the process some more times, say ν, getting in this way a set of outcomes, $\{x_i\}_{i=1}^{\nu}$.

Now that we have this ν outcomes, which may differ among each other, what do we choose as a good *estimator*, $\hat{\chi}$, of the real value of the quantity?

We see that the estimation process is not only using a measurement instrument and getting a number, but a series of steps, which combine possibly multiple measurement and data processing.

To judge the quality of various possible estimators and finally choose the best one, we have to make some reasonable assumptions for the model of noise that affects the measurement. For example, if we have consistency that the instrument always gives higher values than the real quantity, then we will say that our best estimator is probably the minimum among the set of outcomes:

$$\hat{\chi}_{\_} = \min\{x_i\}, \tag{2.1.1}$$

and maybe when we have money we could buy a better balance.

A different reasonable assumption for the noise is that this is Gaussian around the true value with a known, constant width, σ. In this case anyone, even if they have never heard the name Gauss, knows that a good option may be performing *the mean* of the ν outcomes:

$$\hat{\chi}_m = \frac{1}{\nu}\sum_{i=1}^{\nu} x_i. \tag{2.1.2}$$

Even with the same assumption for the noise, there may be other estimators different from the mean which would do the job. Can we say something about the performances of $\hat{\chi}_m$ in

doing the estimation? Is it the best possible estimator or there could be a better one?

To answer this question we introduce the concept of mean-square-error (MSE) of an estimator, which gives the *expected* distance between the guess provided by the estimator and the real value. The adjective *expected*, here as in what follows denoted with the brackets $\langle\cdot\rangle$, means averaged over any possible random set of measurement outcomes, which the estimator needs as input to guess the parameter:

$$(\delta\hat{\chi})^2 = \left\langle \left(\hat{\chi}\left(\{x_i\}\right) - \chi\right)^2 \right\rangle . \tag{2.1.3}$$

If the estimator is unbiased, i.e., its expected value is equal to the true value for any value of χ, then the MSE is simply the variance:

$$(\delta\hat{\chi})^2 = \mathrm{Var}\left[\hat{\chi}\right] = \left\langle \hat{\chi}^2 \right\rangle - \left\langle \hat{\chi} \right\rangle^2 . \tag{2.1.4}$$

The inequality known as the Cramér-Rao bound states that the MSE of any estimator is limited by the inverse of the Fisher information, $\mathcal{I}(\chi)$, and the number of observation, ν, performed.

$$(\delta\chi)^2 \geq \frac{1}{\nu\mathcal{I}(\chi)}. \tag{2.1.5}$$

The Fisher information (FI) is not a property of the specific estimator. Instead it is a property of the statistical model, which stays behind the observation process and returns, as the result of the measurement, the random outcomes $\{x_i\}$ given a particular value for the parameter χ.

To calculate the FI we start from the probability that we observe a particular outcome conditioned to a specific real value of the parameter, the likelihood function $p(x|\chi)$. We then take the logarithmic derivative, i.e., the fractional change [Hedrick, 1913], with respect to χ of the likelihood function, which takes the name of the score. Finally the second moment of the score

(or its variance, since its first moment is zero) is the sought FI:

(2.1.6)
$$\mathcal{I}(\chi) = \left\langle \left(\frac{\partial}{\partial \chi} \ln p(x|\chi) \right)^2 \right\rangle = \int dx \left(\frac{\partial}{\partial \chi} \ln p(x|\chi) \right)^2 p(x|\chi) = \\ = \int dx \frac{1}{p(x|\chi)} \left(\frac{\partial p(x|\chi)}{\partial \chi} \right)^2 .$$

If the logarithm of the likelihood function is twice differentiable than the FI is the expectation value of its curvature with a change of sign:

$$\mathcal{I}(\chi) = - \left\langle \frac{\partial^2}{\partial \chi^2} \ln p(x|\chi) \right\rangle . \tag{2.1.7}$$

This last aspect of FI has an interesting intuitive connection with the sensitivity of inferring a parameter: higher FI means sharper statistical model, i.e., big changes of the possible outcomes with respect to small changes of the parameter, which finally results in an easier distinguishability of the parameter. This is another way to interpret the Cramér-Rao inequality.

Coming back to the simple example we introduced above, let us try to apply the concepts presented up to now and say something about the quality of the mean as an estimator for the parameter of a Gaussian distributed measurement outcomes.

The Gaussian statistical model fixes the likelihood function:

$$p(x|\chi) = \frac{1}{\sigma\sqrt{2\pi}} e^{-\frac{(x-\chi)^2}{2\sigma^2}} . \tag{2.1.8}$$

and so, applying eq. 2.1.7, we can calculate for χ the FI, which is $1/\sigma^2$. The mean is an unbiased estimator so we only have to calculate its variance: we consider eq. 2.1.2 and the fact that the x_i are independent variables, each of them distributed with a variance σ^2. Then we have that the variance of the sum of independent variables is the sum of the single variances and we conclude that

$$\mathrm{Var}\left[\hat{\chi}_m\right] = \frac{1}{\nu^2} \sum_{i=1}^{\nu} \sigma^2 = \frac{\sigma^2}{\nu} . \tag{2.1.9}$$

By comparing eq. 2.1.5 and eq. 2.1.9 and accounting for the calculated FI of the Gaussian distribution, we see that the mean

saturates the Cramér-Rao bound, so we can state that it is the best estimator.

2.2. Extending estimation theory by using quantum mechanics

Everything said up to now regards the classical theory of parameter estimation. To add the possibility of using quantum mechanics for performing parameter estimation we have to include its peculiar features and extend the concepts consequently. A detailed explanation of such an extension can be found in the work by Braunstein and Caves of 1994 [Braunstein and Caves, 1994].

The usual case is when the probe is a quantum system: we start with a known initial state, ρ_0. This evolves under the influence of an unknown parameter χ. While χ is unknown, we know the effect that χ would have on the state ρ, which we describe as a map $\rho_0 \xrightarrow{\chi} \rho_\chi$.

The other big difference when we have to deal with quantum mechanics is that the sequence of actions, the recipe, defining an estimator is more involved. There are clearly two separate steps: the quantum measurement, i.e., the action of some Hermitian operator, an *observable*, on the probe density operator, and the classical data manipulation of the outcomes. With quantum mechanics the first step assumes a much more important role and we will see that this reflects in the explicit dependence of the Fisher information.

The parameter χ usually does not correspond directly to an observable, so several times we have to infer it from quantum measurement of other observables acting on ρ_χ.

As before, we say that a quantum estimator is thus the application of a chosen observable, or more generally a positive-operator valued measure (POVM), a set of positive semidefinite Hermitian operators $\{\Pi_x\}$, with $\int dx \Pi_x = \mathbb{I}$, followed by some algorithm on the outcomes.

To evaluate the performance of quantum estimators let us go with the calculation of Fisher information as defined in eq. 2.1.6. According to Bohr's rule by knowing the probe density operator

and the POVM we can calculate the likelihood function:

$$p(x|\chi) = \mathrm{Tr}\left[\Pi_x \rho_\chi\right]. \tag{2.2.1}$$

We can introduce an operator, which simplifies many calculations: the symmetric logarithmic derivative (SLD), $\mathfrak{L}_\chi$, implicitly defined in the following way,

$$\frac{\rho_\chi \mathfrak{L}_\chi + \mathfrak{L}_\chi \rho_\chi}{2} = \frac{\partial \rho_\chi}{\partial \chi}. \tag{2.2.2}$$

Using the SLD operator we can write the following relation:

$$\frac{\partial}{\partial \chi} p(x|\chi) = \mathrm{Tr}\left[\Pi_x \frac{\partial \rho_\chi}{\partial \chi}\right] = \frac{1}{2}\left(\mathrm{Tr}\left[\Pi_x \rho_\chi \mathfrak{L}_\chi\right] + \mathrm{Tr}\left[\Pi_x \mathfrak{L}_\chi \rho_\chi\right]\right), \tag{2.2.3}$$

which finally allows us to calculate the FI using the following formula[1]:

$$\mathcal{I}(\chi) = \int dx \frac{\mathrm{Re}(\mathrm{Tr}\left[\Pi_x \rho_\chi \mathfrak{L}_\chi\right])^2}{\mathrm{Tr}\left[\Pi_x \rho_\chi\right]}. \tag{2.2.4}$$

The FI, as before, fixes the limit for the sensitivity of any possible estimator which is constructed starting from a defined choice of a particular POVM, by any possible clever algorithm of classical data manipulation. As we mentioned before, the FI explicitly depends on the POVM, i.e., on the set of observables which defines the quantum measurement.

Conversely, if we were able to maximize the FI over all the possible POVMs, this procedure will lead to an ultimate limit on the sensitivity, independent of any possible measurement or classical data manipulation we can perform. The SLD operator makes it easy to do this maximization. Without presenting here all the steps of the demonstration, which can be found in [Braunstein and Caves, 1994], we can say that

$$\mathcal{I}(\chi) \geq \mathrm{Tr}\left[\rho_\chi \mathfrak{L}_\chi^2\right] = \mathfrak{I}(\chi). \tag{2.2.5}$$

The quantity $\mathfrak{I}(\chi)$, which is a lower bound for any possible Fisher information, is called the quantum Fisher information (QFI). It depends only on the initial probe state, ρ_0, more precisely on the geometrical property of the map which ties the

[1] We use the trace property $\mathrm{Tr}\left[ABC\right] = \mathrm{Tr}\left[ACB\right]^\star$, which is valid for the product of three self-adjoint operators.

parameter and the manifold of probe states, $\chi \xrightarrow{\chi} \rho_\chi$, in the neighborhood of the origin.

Using the QFI, we can state the ultimate limit for the sensitivity in the parameter. The quantum Cramér-Rao bound (QCRB) says that

$$(\delta\chi)^2 \geq \frac{1}{\nu\mathfrak{J}(\chi)}. \tag{2.2.6}$$

The term ν, which as we said above reports the number of times the observation has been repeated, accounts simply for the statistical improvement of repeating the measurement, and since it is a completely classical effect we will omit ν for the next of the presentation.

2.3. QCRB and transformation generators

The QFI can be simplified with some very generic assumptions. First, let us consider the case that the transformations of the probe state parametrized by χ are a unitary group, i.e., unitary operators transform the density operators and by consequence there should exist an Hermitian operator, K, which generates the transformation

$$\rho_\chi(t) = U_\chi(t)\rho_0 U_\chi(t)^\dagger, \quad U_\chi(t) = e^{-i\chi K_\chi(t)}. \tag{2.3.1}$$

The generator respects the following equation:

$$\frac{\partial\rho_\chi(t)}{\partial\chi} = -i\left[K_\chi(t), \rho_\chi(t)\right], \tag{2.3.2}$$

which is the parallel of what happens for the generator of the transformation in time, t, the well known Hamiltonian operator:

$$\frac{\partial\rho_\chi(t)}{\partial t} = -\frac{i}{\hbar}\left[H_\chi(t), \rho_\chi(t)\right]. \tag{2.3.3}$$

The second assumption is that the probe is in a pure state, $\rho_\chi^2(t) = \rho_\chi(t)$. If we differentiate this relation with respect to χ we have:

$$\rho_\chi(t)\frac{\partial\rho_\chi(t)}{\partial\chi} + \frac{\partial\rho_\chi(t)}{\partial\chi}\rho_\chi(t) = \frac{\partial\rho_\chi(t)}{\partial\chi}, \tag{2.3.4}$$

and, by comparing with the definition of SLD of eq. 2.2.2, we can write the following expression:

$$\mathfrak{L}_\chi(t) = 2\frac{\partial \rho_\chi(t)}{\partial \chi} = -2i\left[K_\chi(t), \rho_\chi(t)\right], \tag{2.3.5}$$

and as a consequence the QFI is:

$$\mathfrak{I}(\chi, t) = 4\mathrm{Tr}\left[\rho K^2 - \rho K \rho K\right] = 4\mathrm{Var}\left[K_\chi(t)\right]. \tag{2.3.6}$$

Finally the QCRB assumes the form:

$$(\delta\chi)^2 \geq \frac{1}{4\mathrm{Var}\left[K_\chi(t)\right]} \quad \Rightarrow \quad \delta\chi \mathrm{Var}\left[K_\chi(t)\right]^{1/2} \geq \frac{1}{2} \tag{2.3.7}$$

connecting indeed the optimal bound for estimating a parameter to the variance of the operator which generates translation in that parameter. The inequality in eq. 2.3.7 is an inequality known as a Mandelstam-Tamm kind uncertainty relation [Mandelstam and Tamm, 1945; Helstrom, 1976; Holevo, 1982; Dembo et al., 1991; Braunstein et al., 1996], or parameter-based uncertainty relation. Such relations, differently from the Heisenberg uncertainty relation, can be used to find the uncertainty, not only of operators, but also of parameters, e.g., the phase or the time, to which there does not correspond any operator.

2.4. Composite probe system and the role of system size

In this section and the next I will briefly present the argument developed in Caves' group, by Dr. Sergio Boixo in particular, about the scaling property of $\delta\chi$ with the size of a probe composed of N subsystems.

To approach the explicit dependence of $\delta\chi$ with N, we have to introduce a new norm for operators and apply it to the generator K. We say that the seminorm $||\cdot||$ of an Hermitian operator is the difference between its maximum and minimum eigenvalue. With the seminorm we can set an upper bound for the variance of the operators,

$$\mathrm{Var}\left[K_\chi(t)\right] \leq ||K||^2/4. \tag{2.4.1}$$

In this way eq. 2.3.7 becomes

$$\delta\chi \geq \frac{1}{||K||} = \frac{1}{M_K - m_K}, \tag{2.4.2}$$

where M_K and m_K are the maximum and minimum eigenvalues of K, respectively.

Finally we have to connect K to what describes the dynamics in time during the interaction between the probe and the system. A possible Hamiltonian for describing the evolution of the probe can be of the following form:

$$H_\chi = \hbar\left(\chi\mathcal{O} + \mathcal{A}(t)\right). \tag{2.4.3}$$

$\mathcal{O}$ is the part containing the probe operators directly connected to the parameter, while $\mathcal{A}$ contains the free-evolution part of the probe system plus eventual ancillae systems. Terms in $\mathcal{A}$ may have a metrological use in the optimization of the measurement part of the estimation strategy. For example ancillae system may allow one to easily implement a good POVM for approaching the ultimate bound of sensitivity. Boixo and coworkers demonstrated that all these auxiliary terms can be neglected when instead we want to calculate the QCRB: all the important factors for that calculation reside only in the generator of translation in χ, for which we have:

$$K_\chi(t) = i\frac{\partial U_\chi(t)}{\partial\chi}U_\chi^\dagger(t) = i\left(\frac{\partial}{\partial\chi}e^{-i\frac{t}{\hbar}H_\chi}\right)U_\chi^\dagger(t) = t\mathcal{O} \tag{2.4.4}$$

If $\mathcal{O}$ is a linear function of operators describing a composite probe system, i.e.,

$$\mathcal{O} = \sum_{j=1}^{N} o_j \tag{2.4.5}$$

where o_j is the single-unit operator for the $j-$th probe subsystem, with maximum and minimum eigenvalue Λ and λ, then using the triangle inequality for the seminorm we have that

$$\delta\chi \geq \frac{1}{||K||} \geq \frac{1}{tN(\Lambda - \lambda)}, \tag{2.4.6}$$

where we found back the Heisenberg limit (HL) scaling that we introduced in Chapter 1.

The seminorm is a function from Hermitian operators to real numbers. $||K||$ gives a state independent, lower bound on $\delta\chi$. To know the bound for a specific state, we instead have to compute the variance of K.

In composite probe system the inequality in eq. 2.4.1 is saturated by entangled states with wave function of the following form:

$$|\Psi_{ent}\rangle = \frac{|\Lambda\rangle \otimes \cdots \otimes |\Lambda\rangle + |\lambda\rangle \otimes \cdots \otimes |\lambda\rangle}{\sqrt{2}}. \tag{2.4.7}$$

With such a probe states the QCRB, and the HL, is achieved.

Without entanglement, e.g., with simple product states of the following form,

$$|\Psi_{prod}\rangle = \bigotimes_{j=1}^{N} |\psi_j\rangle \tag{2.4.8}$$

we can just say that the variance of K is additive, i.e., we sum the variances of the single o_j operators on the $|\psi_j\rangle$ part of the probe wavefunction, and like adding the single variances of independent random variables we get the classical square-root rule of the standard quantum limit (SQL):

$$\delta\chi \geq \frac{1}{2\mathrm{Var}\,[K]^{1/2}} \propto \frac{1}{\sqrt{N}}. \tag{2.4.9}$$

2.5. Nonlinear Hamiltonian

We are considering that the probe is a composite system made of smaller parties, e.g., a pulse of photons or a cloud of atoms. The way they interact as an ensemble with the system under observation makes a lot of difference, as we will see. In particular it matters if they act independently or by some kind of mutual intercorrelation at the moment of getting information from the system about the parameter to be estimates.

In the previous section, when dealing with linear interaction Hamiltonians we were considering the case of non-interacting probe particles. Let us now imagine that among the probes there are $k-$body interactions coupled to the parameter to estimate.

If we assume that the interaction is symmetric over all the probe particles, then the Hamiltonian has the following form:

$$H = \chi \mathcal{O}^k = \chi \sum_{\{j_1,\dots,j_k\}} o_{j_1} \cdots o_{j_k}. \tag{2.5.1}$$

As before, $\{o_j\}$ are the single-unit operators for the probe subsystems and the sum is running over all the possible combinations of k particles among the N composing the whole probe system. In bounding the seminorm of the generator K, by using the triangle inequality, we will thus have to find the maximum and minimum eigenvalues of K starting from the maximum and minimum eigenvalues of the single-unit operators. For example if k is odd or if Λ and λ have both the same sign, we will have:

$$\delta\chi \geq \frac{1}{||K||} \geq \frac{1}{N^k|\Lambda^k - \lambda^k|t}. \tag{2.5.2}$$

The case with k even and $\lambda \leq 0 \leq \Lambda$ is discussed in details in Boixo's article [Boixo et al., 2008b].

More generically, the nonlinear Hamiltonian can be a more structured $k-$degree polynomial, but only the highest order terms will be relevant, since for sensitivity scaling k will finally be the dominant factor at large values of N.

Also in the case of nonlinear interaction, the QCRB depends finally not just on the Hamiltonian but also on the probe state. The only states that can saturate the best bound permitted by the $k-$order dynamics are the maximally entangled ones, as before. An example is the state in eq. 2.4.7. For this kind of states we have:

$$\delta\chi|_{ent} = \frac{1}{N^k|\Lambda^k - \lambda^k|t}\,. \tag{2.5.3}$$

The interesting fact now is that if we consider only separable product state, such as the one in eq. 2.4.8, much more practical in experiments, then the QCRB in terms of scaling will lose only a factor of $1/2$ with respect to the optimal scaling with entanglement:

$$\delta\chi|_{prod} = f(|\psi\rangle)\frac{1}{N^{k-1/2}}\,, \tag{2.5.4}$$

where f is a factor accounting for the state of the individual probes. Minimum f, i.e., optimal sensitivity, is achieved typically when all the probes are in a state such as $|\psi\rangle = (|\Lambda\rangle + |\lambda\rangle)/\sqrt{2}$. More details about the demonstration of these last equations are presented in [Boixo et al., 2008b]. We see that SQL and HL for linear Hamiltonian are the particular case with $k = 1$ of the formalism presented in this section.

We also see that for the simplest two-body interactions, even product states may achieve a more favorable scaling than the HL scaling, possibly achieving the optimal $1/N^{3/2}$ scaling. We will refer to all such scalings coming from nonlinearities as super-Heisenberg (SH) scalings.

2.6. Proposed implementations

In the years since the argument of better sensitivity scaling using interaction begun to be discussed in the quantum metrology community, several groups have proposed different experimental realizations of such a scheme.

- Bose-Einstein condensate
  In the group of in New Mexico they considered spin-1/2 dynamics, angular momentum operators and possible implementation with Bose Einstein condensate [Boixo et al., 2009]. In the formalisms of the spins they were able easy to answer to the following important question: is the entanglement that in some cases is generated by the nonlinear dynamics responsible for the better sensitivity scaling? They compared two different nonlinear Hamiltonians, functions of the total spin operators

$$H_1 = \chi J_z^2, \quad H_2 = \chi J_0 J_z, \tag{2.6.1}$$

  where J_z is the $z-$component of the angular momentum and J_0 is the total spin, connected to the total number of atoms. Acting on the same product state, an equatorial state on the Bloch sphere, the first creates entanglement and the second does not. They shows that both Hamiltonians are able to achieve the 3/2 power-law scaling in the sensitivity of χ [Boixo et al., 2008a].

- Nano-mechanical resonators
  In 2008 Woolley, Milburn and Caves proposed to perform nonlinear metrology with nano-mechanical devices [Woolley et al., 2008]. In particular, flexural nano-mechanical resonators have an intrinsic Duffing nonlinearity due to extension on bending [Erbe et al., 2000]. The Duffing dynamics appears in systems where the resonance spectrum is curved by the nonlinearity, introducing phenomena of hysteresis, bistability and chaotic behavior [Kozinsky et al., 2007].

  This has some practical interests since the Duffing nonlinearity of a nano-mechanical resonator is an expression of the applied strain [Carr et al., 2001], and nonlinear micro electro-mechanical systems (MEMS) have already been used to make highly sensitive mechanical strain sensors and accelerometers; also they have implication for ultra-sensitive nano-mechanical detection of mass and force [Chaste et al., 2012]. Moreover, technology is progressing toward the point where these resonators can be cooled to near their ground state, making them interesting quantum devices.

- Double-pass optical magnetometers
  Another implementation was proposed in the context of magnetometry by Chase *et al.* [Chase et al., 2009]. Although their proposal has some similarities with our experimental apparatus, which as we will present in the following chapters is a magnetometer using alkali atoms, the approach to nonlinear quantum metrology is completely different.

  They describe a double-pass scheme of read-out light on the atomic magnetic sensor, where because of the mutual action of magnetized atoms and polarized light, and the recirculation of the light along different direction, the response becomes nonlinear with the magnetic field to be measured. Anyway, the authors do

not proceed to an analytic derivation of any possible effective Hamiltonian, which would be difficult to obtain due to the recursive effects involved. They instead apply a stochastic propagator treatment [Sarma et al., 2008] for the continuous measurement of the atomic angular momentum and back-action.

They claim that in specific regimes the improved scaling originated by the nonlinear dynamics is present, making preferable double-pass over single-pass schemes, even if such regimes are probably inaccessible in experimental settings. In any case, they admit having been constrained to simulate only a very small number of spins, ~ 150, when instead the expected collective spin size is of the order of millions of particles.

- Nonlinear optics
  Last but not least, at the beginning of this chapter we mentioned the work of Luis, one of the first scientist who approached nonlinear metrology. He analyzed different schemes and combinations of probe state, interaction dynamics and measurement for achieving SH scaling. His language is much closer to the traditional nonlinear optics treatment, e.g., quadrature, photon number, squeezing operators and higher order function of them, describing the interaction happening between photons inside nonlinear crystals.

  Although in our experiment we have atoms, as we mentioned, the nonlinear metrology scheme we realized and we are presenting in this thesis involves interaction between pairs of photons. In some sense, Luis' proposals are the closest ones to our experiment.

CHAPTER 3

Nonlinear light-atom quantum interface

In the previous chapters we have illustrated the nonlinearity as a new tool in quantum metrology in the way it was proposed by several groups with the mathematical derivation of the connection between order of nonlinearity and improved sensitivity scaling, as well as with some possible practical implementations.

The wide range of nonlinear phenomena, appearing when close-to-resonance photons travel through atomic samples, motivated us to look for a suitable implementation of nonlinear metrology in our experimental apparatus: a polarization based light-atom quantum interface.

The goal of this chapter is to present how we extended the theoretical model of light-atom quantum interfaces, which is in use by our group and others in the same field, and included atom-mediated photon-photon interactions while showing that those have the form of nonlinearities of the type proposed by Boixo *et al.* [Boixo et al., 2007].

To this aim, we will first briefly introduce the light-atom quantum interface formalisms, i.e., collective variable operators and polarizability Hamiltonian in the linear case. Then we will apply a more sophisticated perturbation theory approach to include nonlinearity and finally show the useful feature for metrology of the high order terms just identified in the extended Hamiltonian.

3.1. Collective variables for light-atom quantum interfaces

Interfaces between different systems capable to operate at the quantum regimes have been pursued by the scientific community during the last years for their applications in the field

of quantum network and quantum information. The most exhaustively investigated is the interface between light and atoms, where the first is a good means to transport information over long distances, and the latter are a good medium to store and process information.

A common application of a light-atom quantum interface in metrology is when an atomic sensor is used to probe an external field but the property of the sensor which is changing is difficult to be measured directly and needs an optical read-out.

The important features of light-atom quantum interfaces are many: scientists work to exploit for example versatility, i.e., the capability of operating under different conditions, spatial multimode for imaging application, bandwidth for time resolution, long coherence time for memory. A comprehensive summary of the field can be found in this review by Hammerer *et al.* [Hammerer et al., 2010].

Another important feature is the strength of the coupling between the photonic and the atomic systems. It is related to effectiveness of the resources involved to achieve the desired process: in the context of quantum memory the coupling strength is tied to the concept of fidelity between the information imprinted onto and retrieved from the atomic medium. In the context of metrology, good enough coupling between the two systems means that the optical read-out of the atomic sensor affects minimally the sensitivity to the quantity of interest, e.g., time, gravity, magnetic field, because the information is transferred with high fidelity from the atomic sensor to the light probe.

When single particles are used, cavities are commonly used to boost the coupling between the photon and the atom, but if one is not restricted to use single particles another way to achieve a high light-atom coupling is by working with ensembles, and usually the figure of merit of the coupling scales linearly with the number of photons N_P or number of atoms N_A at the interface.

Commonly used by the scientific community for describing such many particle systems, the relevant quantities are collective properties of the whole sample. We follow the approach of collective continuous variables (CCV), in which both light and

atoms are described by macroscopic quantum variables. For the particular system we have in our lab, an optical magnetometer, the variables of interest are the polarization of a pulse of photons and the angular momentum of the ensemble of rubidium 87 atoms. We will now introduce the collective operators for such observables.

3.2. Stokes operators for light polarization

The mathematical description of a light beam can be done in terms of its oscillating vectorial electric field. Furthermore, this can be seen as a superposition of several components, the modes, each one with its specific frequency, as well as a particular relation between spatial and temporal dependance of the phase, i.e., the wavefront profile.

The simplest example of such modes is the monochromatic plane-wave. Although it is not enough by itself to describe a real propagating pulse of light, this mode is instead enough for the goal of this section, which is to show the way to introduce quantum mechanics in the description of light, in fact a very well established formalism [Scully and Zubairy, 1997; Loudon, 1983; Saleh and Teich, 2001].

Considering the frequency to be ω and the wave-vector to be along the z direction with magnitude $k = \omega/c$, we have

$$\mathbf{E} = \boldsymbol{\mathcal{E}} + \boldsymbol{\mathcal{E}}^* = \mathcal{E} \sum_{p=-1,1} \alpha_p \mathbf{e}_p e^{-i\omega t + ikz} + \text{c.c.}, \tag{3.2.1}$$

where c is the speed of light.

Let us discuss one by one all the terms in eq. 3.2.1. We refer to $\boldsymbol{\mathcal{E}}$ as the positive frequency part, while its complex conjugate is the negative frequency part. This separation is useful for calculating time-averaged quantity such as the intensity, I, which is related to the modulus square of the electric field averaged over several oscillation cycles. We have $I = \langle |\mathbf{E}|^2 \rangle / Z_0 \approx 2\boldsymbol{\mathcal{E}}^* \cdot \boldsymbol{\mathcal{E}} / Z_0$[1], because of the cancellation of the terms $\boldsymbol{\mathcal{E}}^2$ and $(\boldsymbol{\mathcal{E}}^*)^2$ for fast oscillation at frequency 2ω. The free-space impedance, Z_0, is

[1]This is calculated using the Poynting vector concept and the fact that for a plane-wave propagating in free space the magnetic field has a simple expression in terms of the electric field, $\mathbf{B} = \mathbf{E}/c$.

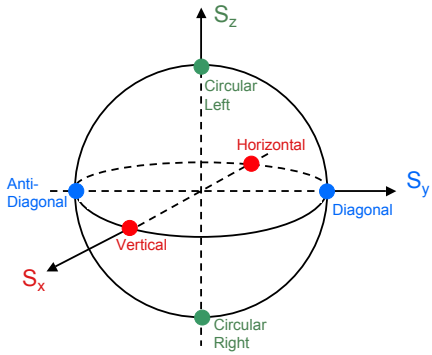

Figure 3.2.1. The Poincaré sphere for representing polarization.

equal to $1/(\varepsilon_0 c) \approx 376\ \Omega$, where ε_0 is the vacuum permittivity. The real number $\mathcal{E}$, with the dimension of an electric field, gives the amplitude of the field oscillation.

We also want to stress the vectorial feature of the polarization: we consider $\{\mathbf{e}_p\}$ being the unit vectors basis of a specific 2-dimension polarization space and $\{\alpha_p\}$ being the respective complex dimensionless amplitudes. Following the usual convention in atomic physics, by choosing the quantization axis along the propagation direction, z, we then have the two circular polarized beams, called $\sigma_\pm$ light, form a basis whose elements are

$$\begin{aligned} \mathbf{e}_+ &= \frac{1}{\sqrt{2}}(-\mathbf{e}_x + i\mathbf{e}_y) \\ \mathbf{e}_- &= \frac{1}{\sqrt{2}}(\mathbf{e}_x - i\mathbf{e}_y) \end{aligned} \tag{3.2.2}$$

with respect to the spatial x and y. Inverting the rules, linear polarized light propagating along z can be seen as coherent superposition of circular polarizations. Finally π polarization describe light with electric field along the quantization axis, which is only possible for light propagating perpendicular to the quantization axis.

In the expression for the intensity, the scalar product $\boldsymbol{\mathcal{E}}^* \cdot \boldsymbol{\mathcal{E}}$ can be developed giving as a result

$$I = \frac{2\mathcal{E}^2}{Z_0}(\alpha_+^*\alpha_+ + \alpha_-^*\alpha_-) = \frac{2\mathcal{E}^2}{Z_0}, \tag{3.2.3}$$

accounting that for fully polarized light $|\alpha_+|^2 + |\alpha_-|^2 = 1$. In addition to that, we can develop a comfortable way to deal with polarization: the Stokes vector $\mathbf{S}$, with which we can pictorially see the polarization as a point on a sphere, the Poincaré sphere[2], as in fig. 3.2.1.

Once we define intensities relatively to particular polarization components, e.g., $I_p = (2\mathcal{E}^2/Z_0)\,\alpha_p^*\alpha_p$, we have that the components of the Stokes vector are:

$$\begin{aligned} S_x &= I_x - I_y, \\ S_y &= I_{\diagup} - I_{\diagdown}, \\ S_z &= I_+ - I_-, \end{aligned} \tag{3.2.4}$$

to which we can add the total intensity, $S_0 = I_x + I_y = I_{\diagup} + I_{\diagdown} = I_+ + I_-$, which is independent of the choice of the basis. The Stokes vector can be synthetically defined as $S_i = (2\mathcal{E}^2/Z_0)(\alpha_+^*, \alpha_-^*)\sigma_i(\alpha_+, \alpha_-)^T$, with $\{\sigma_i\}$ being the Pauli matrices and σ_0 is the identity.

For having a quantum description of a light beam, we follow the second quantization rules that are substituting the dimensionless field amplitude in the positive frequency part of the field with annihilation operators and with creation operators in the negative frequency part:

$$\begin{aligned} \alpha_p &\to \hat{a}_p \\ \alpha_p^* &\to \hat{a}_p^\dagger, \end{aligned} \tag{3.2.5}$$

[2]Although for simplicity we use the common labeling $\{x, y, z\}$ in the coordinate frame for the Poincaré sphere and the Stokes vector, we have to say that the space where these entities live does not coincide with the usual real space. Indeed, some authors prefer a different labeling, e.g., $\{1, 2, 3\}$, to stress that the Stokes vector is defined within a virtual, conceptual space. As we will see later, our choice of using the common $\{x, y, z\}$ notation will result useful in connection with atomic spin systems and their symmetries in the real space.

with the canonical commutation rule $[\hat{a}_p, \hat{a}_q^\dagger] = \delta_{pq}$, where δ_{pq} is the Kronecker symbol.

We note that the factors $\alpha_p^* \alpha_p$, we have just introduced with the Stokes vector become $\hat{a}_q^\dagger \hat{a}_p$, which are operators relative to photon number. For a proper connection of concepts such as Stokes vector and photons, we need some consideration about the energy of the light beam.

The electromagnetic energy density for a plane-wave mode is $u = \varepsilon_0 |\mathbf{E}|^2 = 2\varepsilon_0 \mathcal{E}^2$. If, for example, we consider only circular plus polarized light, we have $S_z = 2\mathcal{E}^2/Z_0$, so we can express the energy density in terms of components of the Stokes vector, $u = \varepsilon_0 Z_0 S_z$.

Until now we have described intensive quantities. The photon number instead is an extensive quantity, so we have to include a mode volume for going from the energy density to the total energy. A finite volume for optical modes is easy identified inside cavities. For a propagating beam in free-space, a mode volume can be introduced for temporal defined pulses of light. With pulses of duration T, the length cT times the transverse area of the beam, A, is a good approximation for the mode volume.

Now, we can equate the classical energy, $u(cTA)$, and its quantum version in terms of photon number

$$\hbar\omega n_+ = \varepsilon_0 Z_0 S_z cTA \Rightarrow S_z = \frac{\hbar\omega}{TA} n_+, \tag{3.2.6}$$

where n_+ is the mean number of circular plus polarized photons, i.e., $n_+ = \langle \hat{a}_+^\dagger \hat{a}_+ \rangle$.

We can define the Stokes operators,

$$\hat{S}_i = (\hat{a}_+^\dagger, \hat{a}_-^\dagger)\sigma_i/2(\hat{a}_+, \hat{a}_-)^T, \tag{3.2.7}$$

or explicitly

$$\begin{aligned}\hat{S}_0 &= \frac{\hat{n}_+ + \hat{n}_-}{2},\\ \hat{S}_x &= \frac{\hat{n}_x - \hat{n}_y}{2},\\ \hat{S}_y &= \frac{\hat{n}_{\diagup} - \hat{n}_{\diagdown}}{2},\\ \hat{S}_z &= \frac{\hat{n}_+ - \hat{n}_-}{2}.\end{aligned} \tag{3.2.8}$$

expressed in terms of the photon number operators for specific polarizations, $\hat{n}_p = \hat{a}_p^\dagger \hat{a}_p$. The relation between components of the classical Stokes vector and the relative Stokes operator is

$$S_i = \frac{2\gamma}{Z_0} 2\hat{S}_i, \tag{3.2.9}$$

with $\gamma = \hbar\omega Z_0/(2TA)$. Comparing eq. 3.2.9 and eq. 3.2.3, we can identify $\sqrt{\gamma}$ as the amplitude of the electric field oscillation for a light pulse constituted by only one photon.

One can easy demonstrate that the Stokes operators follow angular momentum quantization rules $[\hat{S}_i, \hat{S}_j] = i\epsilon_{ijk}\hat{S}_k$, where $\{i, j, k\} \in \{x, y, z\}$ and $\hat{S}_0$ commutes with all the others. The corresponding uncertainty relation is

$$\mathrm{var}(\hat{S}_i)\mathrm{var}(\hat{S}_j) \geq \langle \hat{S}_k \rangle^2/4. \tag{3.2.10}$$

For light polarized along x, the expectation value of the relative Stokes operator is maximum, $\langle \hat{S}_x \rangle = N_P/2$, with N_P being the total number of photons in the beam. Thus, assuming equal uncertainties in the other Stokes components, i.e., what is known as a coherent polarization state, we have

$$\mathrm{var}(\hat{S}_y) = \mathrm{var}(\hat{S}_z) = N_P/4. \tag{3.2.11}$$

That is the way to interpret shot-noise in the polarization context.

3.3. Spin variables for atomic ensembles

For many atomic species and alkali atoms in particular, the angular momentum properties of the ground state is one of the

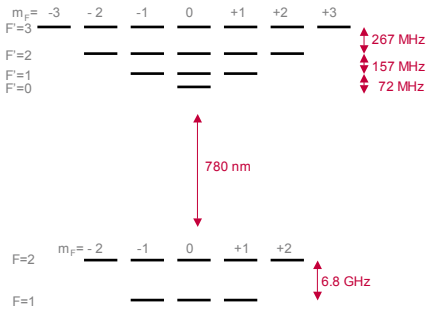

Figure 3.3.1. D_2 transition for ^{87}Rb. The 24 states, 8 ground and 16 excited, are labelled by the quantum numbers for the total angular momentum. The energy separation between levels is reported on the right.

key features defining the way the atom interacts with polarized light.

The total angular momentum of an atom is described by a set of quantum operators, $\{\hat{f}_i\}$, which get contributions from the orbital momentum of the electrons, as also from the intrinsic spin of electrons and nucleus. In the case of ^{87}Rb, the nucleus has spin $I = 3/2$ so that the electronic ground state $5S_{1/2}$ has two main quantum numbers for the total spin, $F = 1$ and $F = 2$, corresponding to levels with hyperfine energy splitting of $\Delta_{\rm hfs}/\hbar = 2\pi \times 6.8$ GHz. The first excited state, $5p$, has a fine splitting due to spin-orbit coupling, resulting in the well known alkali doublet D_1(795nm) and D_2(780nm) transitions, respectively $5P_{1/2}$ with two manifolds $F' = \{1, 2\}$ and $5p_{3/2}$ with four manifolds $F' = \{0, 1, 2, 3\}$, each F manifold having its $2F + 1$ magnetic sublevels. In fig. 3.3.1 we symbolize the 24 electronic states within the structure of the D_2 transition.

Here and in the rest of the thesis, we will use the notation $F \to F'$ to indicate transitions between ground and excited levels. For example $2 \to 1'$ will denote a transition from $F = 2$ to $F' = 1$.

The angular momentum of the whole ensemble of N_A atoms is thus the sum of all the single spins:

$$\hat{\mathbf{F}} = \sum_{l=1}^{N_A} \hat{\boldsymbol{f}}^{(l)} \tag{3.3.1}$$

The condition of indistinguishability of the atoms among them, translates into limiting the full Hilbert space of the sum of angular momenta only to the symmetric subspace, having as quantum number simply the sum of the individual quantum numbers, $F_{\text{tot}} = FN_A$. The dimension of the subspace then grows in a polynomial and not in an exponential way with the atom number, being $2FN_A + 1$.

The components of the spin for the ensemble, as quantum operators, obey to commutation relation rules:

$$\left[\hat{F}_x, \hat{F}_y\right] = i\hbar\hat{F}_z \tag{3.3.2}$$

and cyclic permutations.

The ensemble angular momentum is an important observable in magnetometry applications because it couples to the external magnetic field, $\mathbf{B}$, as in the simplest case of the linear Zeeman effect Hamiltonian, $\hat{H}_B = -\hbar g\mathbf{B}\cdot\hat{\mathbf{F}}$, which causes Larmor precessions.

Similarly as for Stokes operators, eq. 3.3.2 is the source of uncertainty relations such as

$$\text{var}(\hat{F}_i)\text{var}(\hat{F}_j) \geq \frac{\hbar^2\langle\hat{F}_k\rangle^2}{4}. \tag{3.3.3}$$

Also in a similar way as for light, the angular momentum state can be depicted as a vector pointing on a sphere, the Bloch sphere.

A coherent spin state (CSS) is the one where the angular momentum is maximum along a particular direction in space, let us say x for example,

$$\langle\hat{F}_x\rangle = \hbar FN_A \tag{3.3.4}$$

and has equal uncertainties in the other two perpendicular components[3]

$$\mathrm{var}(\hat{F}_y) = \mathrm{var}(\hat{F}_z) = \frac{\hbar^2 F N_A}{2}, \tag{3.3.5}$$

the standard level of noise, which in this context is known as projection noise.

3.3.1. Pseudo-spin 1/2 embedded into a higher F manifold. If we restrict the angular momentum operators into a manifold with a defined F, there it is possible to define another set of angular momentum operators. For example, let us consider the $F = 1$ ground state of ^{87}Rb: the operators defined as follows,

$$\begin{aligned} \hat{J}_x &= \frac{\hat{F}_x^2 - \hat{F}_y^2}{2}, \\ \hat{J}_y &= \frac{\hat{F}_x \hat{F}_y + \hat{F}_y \hat{F}_x}{2}, \\ \hat{J}_z &= \frac{\hat{F}_z}{2} \end{aligned} \tag{3.3.6}$$

respect the commutation relations $\left[\hat{J}_x, \hat{J}_y\right] = i\hbar \hat{J}_z$.

The $\{J_i\}$ operators so defined are indeed a representation of a collective pseudo-spin 1/2 system within the $F = 1$. This can be seen coming back from the collective down to the single-spin operators: also for the J operators the following relation is valid, $\hat{J}_i = \sum_l^{N_A} \hat{j}_i^{(l)}$. Let us just consider one spin, the basis of its Hilbert space is a set of states defined by the magnetic quantum number, $\{|\psi_{+1}\rangle, |\psi_0\rangle, |\psi_{-1}\rangle\}$, after a particular choice of a quantization axis, let say z. The pseudo-spin operators are defined at the single-atom level in the following way:

$$\hat{j}_i = \frac{\hbar}{2}(|\psi_{+1}\rangle, |\psi_{-1}\rangle)\sigma_i(\langle\psi_{+1}|, \langle\psi_{-1}|)^T \tag{3.3.7}$$

[3]The same argument is valid for any direction in the space and the perpendicular plane to it.

or explicitly

$$\hat{j}_x = \frac{\hbar}{2}\begin{pmatrix} 0 & 0 & 1 \\ 0 & 0 & 0 \\ 1 & 0 & 0 \end{pmatrix}, \quad \hat{j}_y = \frac{\hbar}{2}\begin{pmatrix} 0 & 0 & -i \\ 0 & 0 & 0 \\ i & 0 & 0 \end{pmatrix}, \tag{3.3.8}$$
$$\hat{j}_z = \frac{\hbar}{2}\begin{pmatrix} 1 & 0 & 0 \\ 0 & 0 & 0 \\ 0 & 0 & -1 \end{pmatrix}.$$

As a pseudo-spin 1/2 system, the atomic angular momentum has a strong analogy with the polarization of a photon described in terms of Stokes operators. We can close the analogy with the photonic system considering the single-atom operator defined using the 2-by-2 identity at the place of the Pauli matrix in eq. 3.3.7,

$$\hat{j}_0 = \frac{\hbar}{2}\begin{pmatrix} 1 & 0 & 0 \\ 0 & 0 & 0 \\ 0 & 0 & 1 \end{pmatrix}, \tag{3.3.9}$$

and the respective collective operator $\hat{J}_0 = \sum_l^{N_A} \hat{j}_0^{(l)}$, which counts all the atoms except the ones in the in the $|\psi_0\rangle$ state.

Let us consider the ensemble with all the atoms in the following superposition state

$$|\psi\rangle = \frac{|\psi_{+1}\rangle + |\psi_{-1}\rangle}{\sqrt{2}}; \tag{3.3.10}$$

This corresponds to the CSS with $\langle \hat{J}_x \rangle = \hbar N_A/2$ and uncertainty in the other components at the projection noise level,

$$\mathrm{var}(\hat{J}_y) = \mathrm{var}(\hat{J}_z) = \frac{\hbar^2 N_A}{4}. \tag{3.3.11}$$

The pseudo-spin operators just introduced are not only an elegant way to define spin 1/2 system. They have a close connection with the symmetries of the atomic ensemble. In particular they represent the *alignment* of the angular momentum of the sample, while the $\{\hat{F}_i\}$ operators represent the *orientation* of the angular momentum instead.

This implies that the $\{\hat{J}_i\}$ does not respond as simply as the $\{\hat{F}_i\}$ to an external magnetic field, i.e., precessing around it. Anyway, even if $[\hat{F}_i, \hat{J}_i] \neq 0$, they share at least one eigenvector,

meaning that a specific CSS, the one aligned to maximize $\langle \hat{J}_i \rangle$ is invariant under the effect of a B_i field.

In the rest of the chapter we will see how the complete parallelism, between the Stokes operator for light polarization and the pseudo-spin operators just introduced, matters at the moment of building the mathematical description of the interaction between the two systems.

3.4. Tensorial polarizability Hamiltonian: the linear case

As common in dealing with interacting quantum systems, the Hamiltonian[4] can be expressed as a term driving a well known and solvable free evolution, plus a small perturbation [Messiah, 1999; Sakurai, 1994]. Let first consider the single-atom case and then extend to the whole ensemble simply by replacing single-atom operators such as $\boldsymbol{f}$ with collective operators, $\mathbf{F}$. We can assume

$$h = h_0 + h_{\text{int}}. \tag{3.4.1}$$

The free evolution term, h_0 accounts for the relevant atomic energy levels and states, $\sum_k \hbar\omega_k \left|\phi_k\right\rangle \left\langle\phi_k\right|$. Similarly it includes the energy of the light field described by a single-mode model as in the quantized version of eq. 3.2.1.

$$\mathbf{E} = \boldsymbol{\mathcal{E}} + \boldsymbol{\mathcal{E}}^\dagger = \sqrt{\gamma} \sum_{p=-1,1} a_p \mathbf{e}_p e^{-i\omega t + ikz} + \text{h.c.}, \tag{3.4.2}$$

The main contribution to the coupling between the atom and the light is the electric dipole interaction, $h_{\text{int}} = -\mathbf{E} \cdot \mathbf{d}$. The dipole operator, $\mathbf{d} = e\mathbf{r}$, can be split into raising $\mathbf{d}_\uparrow$ and lowering part $\mathbf{d}_\downarrow$, connecting ground to excited levels and vice versa.

$$\begin{aligned} \mathbf{d}_\uparrow &= \sum_{\varsigma,\varsigma'} \left|\varsigma'\right\rangle \left\langle\varsigma'\right| \mathbf{d} \left|\varsigma\right\rangle \left\langle\varsigma\right| e^{i(\omega_{\varsigma'} - \omega_\varsigma)t} \\ \mathbf{d}_\downarrow &= \sum_{\varsigma,\varsigma'} \left|\varsigma\right\rangle \left\langle\varsigma\right| \mathbf{d} \left|\varsigma'\right\rangle \left\langle\varsigma'\right| e^{-i(\omega_{\varsigma'} - \omega_\varsigma)t}, \end{aligned} \tag{3.4.3}$$

[4] In this section, we will drop the hat above all the symbols for operators, for the sake of simplicity.

where ς stands for a particular combination of quantum numbers F and m_F identifying a specific ground state, while ς' does the same within the excited-state manifold.

We choose the origin of energy such that $\omega_{F=1} = 0$, and define $\Delta_{\text{hfs}} \equiv \omega_{F=2}$. We work in a frame rotating with the laser frequency ω and define detunings $\delta_{F'} \equiv \omega_{F'} - \omega$. Performing the rotating wave approximation [Loudon, 1983; Scully and Zubairy, 1997; Cohen-Tannoudji et al., 1992], the single-atom perturbation h_{int} is approximated as $h_{\text{int}} \approx \boldsymbol{\mathcal{E}} \cdot \mathbf{d}_{\uparrow} + \boldsymbol{\mathcal{E}}^{\dagger} \cdot \mathbf{d}_{\downarrow}$. Terms with annihilation operators for photons go with raising dipole operators and creation of photons goes with lowering dipole operators.

As described by several authors [Kupriyanov et al., 2005; Geremia et al., 2006; de Echaniz et al., 2008], a simple perturbation expansion method, known as adiabatic elimination, is applicable in the case of off-resonant light, i.e., when $\delta_{F'}$ is bigger than the splitting between the excited states. The adiabatic elimination is basically a second-order perturbation, where two ground states are connected by scattering two photons through a virtual excited state, without populating any real excited state (see fig 3.4.1).

This method gives rise to an effective Hamiltonian of the form $h_{\text{eff}} = \boldsymbol{\mathcal{E}}^{\dagger} \cdot \overset{\leftrightarrow}{\alpha} \cdot \boldsymbol{\mathcal{E}}$, where

$$\overset{\leftrightarrow}{\alpha} = \sum_{\varsigma'} \frac{\mathbf{d}_{\downarrow} |\varsigma'\rangle \langle\varsigma'| \mathbf{d}_{\uparrow}}{\hbar \delta_{\varsigma'}} \tag{3.4.4}$$

is the tensor polarizability operator. As shown by John K. Stockton in his thesis [Stockton, 2007], $\overset{\leftrightarrow}{\alpha}$ can be expressed in terms of the atomic pseudo-spin operators $\{j_i\}$, and the dyadic product can be expressed as a sum of irreducible terms of different rank, i.e., scalar, vectorial and tensorial.

In the effective Hamiltonian for the whole ensemble, the single atom operators sum up into collective operators and any tensorial term couple with a specific function of light Stokes operator. In particular we have

$$H_{\text{eff}} = 2\gamma \left[\alpha^{(1)} S_z J_z + \alpha^{(2)} \left(S_x J_x + S_y J_y \right) \right], \tag{3.4.5}$$

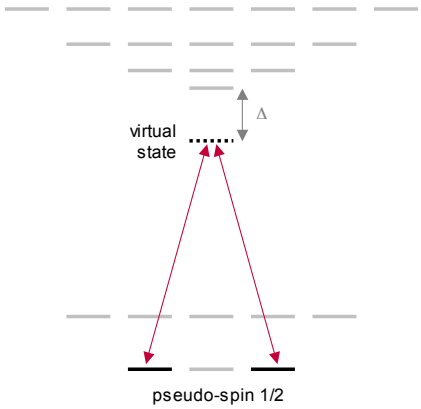

Figure 3.4.1. Adiabatic elimination. In this second order perturbation method, two ground states are connected via scattering photons through a virtual excited state. The real excited states remain not populated, and this allows their elimination in the treatment.

where $\alpha^{(1)}$ and $\alpha^{(2)}$ are the coefficients for the vectorial and tensorial polarizability [5], which are basically functions of Clebsh-Gordan coefficients and detunings from the atomic electronic structure. In the next section we will derive the explicit form for the two coefficients but using a different technique from the adiabatic elimination.

The light propagation axis, z in the considered case, fixes the roles of the different Stokes and pseudo-spin component. The ratio between vectorial and tensorial contributions can be tuned by adjusting the detuning, giving a variety of Hamiltonians interesting for quantum information tasks [de Echaniz et al., 2008],

$$\frac{\alpha^{(1)}}{\alpha^{(2)}} = \frac{5\delta_0\delta_1 - 5\delta_0\delta_2 - 4\delta_1\delta_2}{\delta_0\delta_1 - 5\delta_0\delta_2 + 4\delta_1\delta_2}. \tag{3.4.6}$$

Special detunings, which null one of the two coefficients, are particularly important and deserve to be mentioned (see

[5] In eq. 3.4.5 we have omitted all the rank-0, scalar terms, which do not cause rotations of the optical polarization since appear multiplied to S_0.

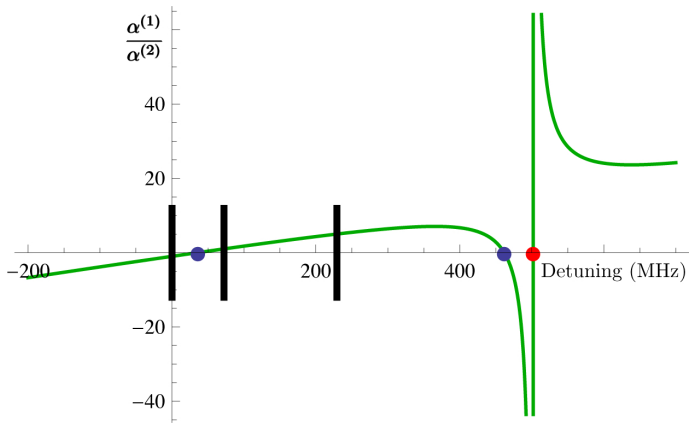

Figure 3.4.2. Tuning by frequency of the vectorial-to-tensorial polarizability. The three vertical bars mark the detunings corresponding to the three transition: $1 \rightarrow \{0', 1', 2'\}$. The zero-crossing points are marked with blue circles at ∼36 and ∼462 MHz, while a red circle marks the detuning of ∼502 MHz where $\alpha^{(2)} = 0$.

fig. 3.4.2). We sometimes refer to them as "magic" detunings. For the D_2 transition of ^{87}Rb, at 501.79 MHz $\alpha^{(2)}$ goes to zero, meaning that the polarizability Hamiltonians keeps only its vectorial term $S_z J_z$.

Even more important for the purpose of this thesis are the detunings where $\alpha^{(1)}$ goes to zero, instead. In the following chapters we will explain how we used the detuning corresponding to 461.71 MHz, distant from the resonances more than the one at 35.84 MHz, to make the probe insensitive, at a first order, to the atomic magnetization.

To understand the origin of these magic detunings, we give an intuition about the physics behind the interaction. Let us consider the vectorial term, $J_z S_z$. It accounts for the following effect: the two circular polarizations experience different indexes of refraction because of the population imbalance in the ground state, J_z, and the overall strength of the dipole moments relative to the transitions towards the several excited states.

The result is a phase-difference acquired between the two circular polarizations, which translate into a change in the polarization state of the interacting light.

The strength of the several transitions can be tuned adjusting the laser frequency, and at specific detunings the symmetry is so between left and right transitions that the index of refraction becomes insensitive to the population imbalance. These are the detunings where $\alpha^{(1)}$ goes to zero.

Although the index of refraction, linear polarizability, is balanced between left and right transitions, other effects may not be balanced, such as the saturation rate of the different transitions. These other effects can break the symmetry at higher probe light intensity, giving back sensitivity to the ground state population in a nonlinear way.

3.5. Degenerate perturbation theory for higher order interactions

We thus need a formalism which include nonlinear interaction. The most relevant interactions we want to describe are polarization effects of fast electronic nonlinearities including saturation and four-wave mixing.

To find such a formalism for nonlinear effects, we generalize the CCV method to the nonlinear optics regime, i.e., we include higher-order processes in the effective Hamiltonian. For this purpose, naïve application of the higher-order perturbation theory fails due to the appearance of vanishing resonance denominators, and the degenerate perturbation theory [Klein, 1974] is required. We did the calculations for ^{87}Rb, but the same formalism is valid for other alkali species.

We start from the explicit matrix form of the interaction Hamiltonian. The base we use is the D_2 transition manifold, with the following sorting: before the 8 ground states, $|F, m_F\rangle$ with $(F, m_F) = (1,-1), (1,0), (1,1), (2,-2), \ldots, (2,2)$, followed by the 16 excited states are $|F', m_{F'}\rangle$ with $(F', m_{F'}) = (0,0)$, $(1,-1), (1,0), \ldots, (3,3)$.

With this notation and considering the rotating wave approximation, we can write the unperturbed and interaction parts in the single-atom Hamiltonian of eq. 3.4.1. The unperturbed

Hamiltonian is

$$h_0 = \hbar(0\mathbb{I}_3 \oplus \Delta_{\text{hfs}}\mathbb{I}_5 \oplus \delta_0\mathbb{I}_1 \oplus \delta_1\mathbb{I}_3 \oplus \delta_2\mathbb{I}_5 \oplus \delta_3\mathbb{I}_7). \tag{3.5.1}$$

If $\mathcal{E}_\pm$ are the amplitudes for the sigma-plus/minus components, respectively, of the light field, then the matrix element of the perturbation part in the Hamiltonian, $V = h_{\text{int}}$, can be calculated starting from

$$\left\langle F', m_{F'} \right| V \left| F, m_F \right\rangle = \mathcal{E}_q \left\langle F', m_{F'} \right| er_q \left| F, m_F \right\rangle \tag{3.5.2}$$

with $q = m_{F'} - m_F$. Note that $q = 0$ transitions ($\pi-$transitions) are not considered because the $z-$propagating beam cannot contain this polarization. The dipole matrix elements are related to the "matrix element" $\langle J| \left|er_q\right| |J'\rangle \equiv D_{JJ'} \approx 3.58410^{-29}\text{C} \cdot \text{m}$ by angular-momentum addition rules. We follow the conventions given in Steck [Steck, 2009].

In this way, we arrive to the perturbation Hamiltonian

$$V = \begin{pmatrix} 0_8 & V_\uparrow^\dagger \\ V_\uparrow & 0_{16} \end{pmatrix} \tag{3.5.3}$$

where $0_d = 0\mathbb{I}_d$ and
(3.5.4)

$$V_\uparrow \equiv \sqrt{5} D_{JJ'} \begin{pmatrix}
\frac{\mathcal{E}_+}{\sqrt{30}} & 0 & \frac{\mathcal{E}_-}{\sqrt{30}} & 0 & 0 & 0 & 0 & 0 \\
0 & \frac{\mathcal{E}_-}{2\sqrt{6}} & 0 & \frac{\mathcal{E}_+}{10} & 0 & \frac{\mathcal{E}_-}{10\sqrt{6}} & 0 & 0 \\
\frac{\mathcal{E}_+}{2\sqrt{6}} & 0 & \frac{\mathcal{E}_-}{2\sqrt{6}} & 0 & \frac{\mathcal{E}_+}{10\sqrt{2}} & 0 & \frac{\mathcal{E}_-}{10\sqrt{2}} & 0 \\
0 & \frac{\mathcal{E}_+}{2\sqrt{6}} & 0 & 0 & 0 & \frac{\mathcal{E}_+}{10\sqrt{6}} & 0 & \frac{\mathcal{E}_-}{10} \\
\frac{\mathcal{E}_-}{2\sqrt{5}} & 0 & 0 & 0 & \frac{\mathcal{E}_-}{2\sqrt{15}} & 0 & 0 & 0 \\
0 & \frac{\mathcal{E}_-}{2\sqrt{10}} & 0 & \frac{\mathcal{E}_+}{2\sqrt{15}} & 0 & \frac{\mathcal{E}_-}{2\sqrt{10}} & 0 & 0 \\
\frac{\mathcal{E}_+}{2\sqrt{30}} & 0 & \frac{\mathcal{E}_-}{2\sqrt{30}} & 0 & \frac{\mathcal{E}_+}{2\sqrt{10}} & 0 & \frac{\mathcal{E}_-}{2\sqrt{10}} & 0 \\
0 & \frac{\mathcal{E}_+}{2\sqrt{10}} & 0 & 0 & 0 & \frac{\mathcal{E}_+}{2\sqrt{10}} & 0 & \frac{\mathcal{E}_-}{2\sqrt{15}} \\
0 & 0 & \frac{\mathcal{E}_+}{2\sqrt{5}} & 0 & 0 & 0 & \frac{\mathcal{E}_+}{2\sqrt{15}} & 0 \\
0 & 0 & 0 & \frac{\mathcal{E}_-}{\sqrt{10}} & 0 & 0 & 0 & 0 \\
0 & 0 & 0 & 0 & \frac{\mathcal{E}_-}{\sqrt{15}} & 0 & 0 & 0 \\
0 & 0 & 0 & \frac{\mathcal{E}_+}{5\sqrt{6}} & 0 & \frac{\mathcal{E}_-}{5} & 0 & 0 \\
0 & 0 & 0 & 0 & \frac{\mathcal{E}_+}{5\sqrt{2}} & 0 & \frac{\mathcal{E}_-}{5\sqrt{2}} & 0 \\
0 & 0 & 0 & 0 & 0 & \frac{\mathcal{E}_+}{5} & 0 & \frac{\mathcal{E}_-}{5\sqrt{6}} \\
0 & 0 & 0 & 0 & 0 & 0 & \frac{\mathcal{E}_+}{\sqrt{15}} & 0 \\
0 & 0 & 0 & 0 & 0 & 0 & 0 & \frac{\mathcal{E}_+}{\sqrt{10}}
\end{pmatrix}$$

As we have mentioned the adiabatic elimination does not work for higher terms in the perturbation expansion, basically because such terms will describe 4-photon processes, twice the process of going from the ground state to the virtual excited and back. An intermediate level in this process will be at the same frequency (degenerate) as the initial state meaning that vanishing denominators will appear.

We have to use a more general method for dealing with this nonlinear terms. The method, called degenerate perturbation theory, was introduced by Klein [Klein, 1974]. The notation of that work is somewhat obscure, so for ease of understanding we repeat the main results. From equation (A7) of that work, we

have the $t-$order contribution to the effective Hamiltonian

$$h_{\text{eff}}^{(t)} = \sum_{\{k\}} A_{\{k\}} O_{\{k\}} \tag{3.5.5}$$

Where $k_1, \ldots, k_{t-1}$ are non-negative integers, the A are real coefficients, the O, denoted "$(k_1, k_2, \ldots, k_t)$" by Klein, are operators, and the sum is taken over all $\{k\}$ satisfying $\sum_{l=1}^{t-1} k_l = t-1$. The A are given in Table I of that work and the O are given in equation (A1) as

$$O_{\{k_1,\ldots,k_{t-1}\}} \equiv P_0 V R^{(k_1)} V R^{(k_2)} \ldots V R^{(k_{t-1})} V P_0 \tag{3.5.6}$$

with P_0 being the projector onto the degenerate subspace $F = 1$, $m_F = \{-1, 0, +1\}$ and by equation (II.A.5)

$$R^{(k)} \equiv \begin{cases} P_0 & k = 0 \\ \left(\frac{1-P_0}{E_0 - H^{(0)}}\right)^k & k > 0 \end{cases} \tag{3.5.7}$$

where E_0 is the energy of the degenerate subspace. In our case we have chosen $E_0 = 0$.

We can then directly calculate the second- and fourth-order contributions. We are only concerned with h_{eff} as it acts on the $F = 1$ subspace, that is, with a 3×3 matrix, and it is convenient to express it in terms of the pseudo-spin operators j_0, j_x, j_y, j_z and the Stokes operators S_0, S_x, S_y, S_z defined above. Summing the second-order contributions we find $h_{\text{eff}}^{(2)}$, exactly like in 3.4.5. With $B \equiv -D_{JJ'}^2/24\delta_0\delta_1\delta_2\hbar$,

$$\begin{aligned} \alpha^{(1)} &= B(5\delta_0\delta_1 - 5\delta_0\delta_2 - 4\delta_1\delta_2) \\ \alpha^{(2)} &= B(\delta_0\delta_1 - 5\delta_0\delta_2 + 4\delta_1\delta_2) \end{aligned} \tag{3.5.8}$$

Similarly, the fourth-order contribution is, dropping terms in S_0^2,

$$\begin{aligned} H_{\text{eff}}^{(4)} = 4\gamma^2 \Big[&\beta_J^{(0)} S_z^2 J_0 + \beta_N^{(0)} S_z^2 N_A + \beta^{(1)} S_0 S_z J_z + \\ &+ \beta^{(2)} S_0 (S_x J_x + S_y J_y) \Big] . \end{aligned} \tag{3.5.9}$$

Note that the term in N_A arises because $h^{(4)}_{\text{eff}}$ contains a self-rotation term of the form $\beta^{(0)}_{m=0} S_z^2 P_{m=0}$ where $P_{m=0}$ is a projector onto the state $|F=1, m_F=0\rangle$. We express this in terms of J_0 and N_A using $\sum_i P^{(i)}_{m=0} = \sum_i (\mathbb{I}_3^{(i)} - j_0^{(i)}) = N_A - J_0$.

With $C \equiv D^4_{JJ'}/576\delta_0^3\delta_1^3\delta_2^3\Delta_{\text{hfs}}\hbar^3$, the coefficients, shown graphically in figure 3.5.1, are

(3.5.10)

$$\begin{aligned}
\beta_J^{(0)} &= C\left(12\delta_0^3\delta_1^2\delta_2^2 - 4\delta_0^3\delta_1\delta_2^3 + 12\delta_0^3\delta_1^3\Delta_{\text{hfs}} - 10\delta_0^3\delta_1^2\delta_2\Delta_{\text{hfs}} + \right.\\
&\quad -12\delta_0^2\delta_1^3\delta_2\Delta_{\text{hfs}} - 10\delta_0^3\delta_1\delta_2^2\Delta_{\text{hfs}} - 12\delta_0\delta_1^3\delta_2^2\Delta_{\text{hfs}} + \\
&\quad \left.+20\delta_0^2\delta_1\delta_2^3\Delta_{\text{hfs}} + 20\delta_0\delta_1^2\delta_2^3\Delta_{\text{hfs}}\right)\\
\beta_N^{(0)} &= C\left(-12\delta_0^3\delta_1^3\delta_2 - 24\delta_0^3\delta_1^2\delta_2^2 + 4\delta_0^3\delta_1\delta_2^3\right)\\
\beta^{(1)} &= C\left(-9\delta_0^3\delta_1^3\delta_2 + 6\delta_0^3\delta_1^2\delta_2^2 + 3\delta_0^3\delta_1\delta_2^3 + 35\delta_0^3\delta_1^3\Delta_{\text{hfs}} + \right.\\
&\quad -5\delta_0^3\delta_1^2\delta_2\Delta_{\text{hfs}} - 4\delta_0^2\delta_1^3\delta_2\Delta_{\text{hfs}} - 5\delta_0^3\delta_1\delta_2^2\Delta_{\text{hfs}} - 4\delta_0\delta_1^3\delta_2^2\Delta_{\text{hfs}} + \\
&\quad \left.-25\delta_0^3\delta_2^3\Delta_{\text{hfs}} - 20\delta_0^2\delta_1\delta_2^3\Delta_{\text{hfs}} - 20\delta_0\delta_1^2\delta_2^3\Delta_{\text{hfs}} - 16\delta_1^3\delta_2^3\Delta_{\text{hfs}}\right)\\
\beta^{(2)} &= C\left(3\delta_0^3\delta_1^3\delta_2 - 6\delta_0^3\delta_1^2\delta_2^2 + 3\delta_0^3\delta_1\delta_2^3 + 7\delta_0^3\delta_1^3\Delta_{\text{hfs}} + \right.\\
&\quad -15\delta_0^3\delta_1^2\delta_2\Delta_{\text{hfs}} + 16\delta_0^2\delta_1^3\delta_2\Delta_{\text{hfs}} - 15\delta_0^3\delta_1\delta_2^2\Delta_{\text{hfs}} + \\
&\quad \left.+16\delta_0\delta_1^3\delta_2^2\Delta_{\text{hfs}} - 25\delta_0^3\delta_2^3\Delta_{\text{hfs}} + 16\delta_1^3\delta_2^3\Delta_{\text{hfs}}\right)
\end{aligned}$$

Terms containing the parameters β are quadratic in $\mathbf{S}$, indicating photon-photon interactions as expected. As in the linear case, the frequency dependence of the nonlinear terms provides considerable flexibility in designing a light-matter interaction.

Following the arguments of Chapter 2, when applied to quantum metrology, these terms may produce super-Heisenberg scaling, because they are nonlinear in the S_i collective variables, with the atomic variables J_i as well as N_A playing the role of the parameter.

The terms containing $\beta^{(0)}$ and $\beta^{(1)}$ are analogous to Hamiltonians considered by Boixo *et al.* [Boixo et al., 2007]. The vectorial term containing $\beta^{(1)}$, which is $\propto S_0 S_z$, in particular, achieves SH scaling without input or generated entanglement [Boixo et al., 2008a]. Moreover, as well as the linear term containing $\alpha^{(1)}$, it is an example of a quantum non-demolition

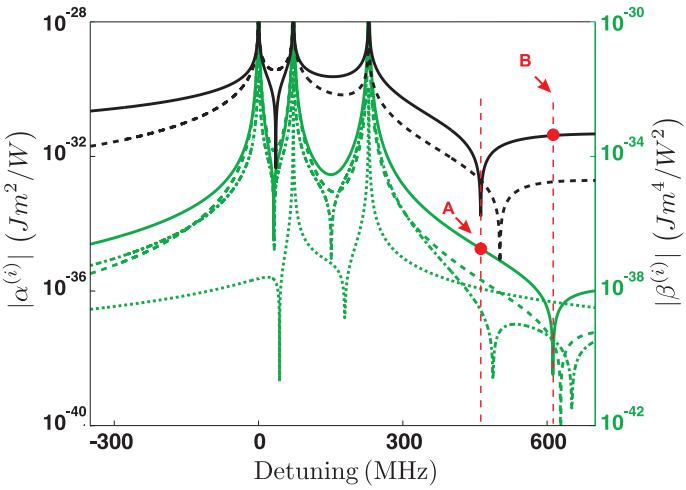

Figure 3.5.1. Spectra of the Hamiltonian terms. The first two curves from the top, the left axis: continuous, $\alpha^{(1)}$; dashed, $\alpha^{(2)}$. Lower curves, the right axis: continuous, $\beta^{(1)}$; dotted, $\beta_N^{(0)}$; dashed, $\beta^{(2)}$; dot-dashed, $\beta_J^{(0)}$. Detuning (MHz) is relative to the transition $1 \to 0'$ of ^{87}Rb D_2 transition. Points A and B indicate detunings at which $\alpha^{(1)}$ or $\beta^{(1)}$ vanish.

(QND) Hamiltonian because commutes with J_z, allowing measurement of this variable without affecting it.

The term containing $\beta^{(2)}$ describes a nonlinear tensorial contribution, and does not appear to have been considered yet for nonlinear metrology.

3.6. Quantum Noise

In fact, for claiming anything about the possible metrological use of such nonlinear Hamiltonian terms, we have to investigate how they deal with quantum noise. To understand the quantum noise in this system, as common in the collective-continuos variable literature [Mølmer and Madsen, 2004; Koschorreck and Mitchell, 2009], in the Heisenberg picture we look at input-output equations for the operators transformed by Hamiltonians. From these equations we derive the variances of the operators and discuss the noise-related aspects.

A typical input state, a coherent state, has $\langle(S_x, S_y, S_z)\rangle = = (N_P/2, 0, 0)$ and $\mathrm{var}(S_i) = N_P/4$. Evolution under the effective Hamiltonian 3.5.9 produces, to first order in the interaction time t_0,

$$S_y^{(\mathrm{out})} = S_y^{(\mathrm{in})} + \frac{t_0}{\hbar}(\alpha^{(1)} + \beta^{(1)} 2\gamma S_0) 2\gamma S_x^{(\mathrm{in})} J_z^{(\mathrm{in})} \tag{3.6.1}$$

plus terms containing $S_z^{(\mathrm{in})} J_x^{(\mathrm{in})}$ that are negligible for the given input coherent state of the light. This evolution physically corresponds to a paramagnetic Faraday rotation of the input linear polarization. In a metrological scheme one would measure this polarization rotation and from it estimate the atomic variable J_z.

For small rotation on the Poincaré sphere, i.e.

$$\phi \equiv S_y^{(\mathrm{out})}/S_x^{(\mathrm{in})} = 2\gamma t_0 \hbar^{-1}(\alpha^{(1)} + \beta^{(1)} 2\gamma S_0) J_z^{(\mathrm{in})} \ll 1, \tag{3.6.2}$$

we note that the input polarization noise dominates:

$$\mathrm{var}(S_y^{(\mathrm{out})}) = \mathrm{var}(S_y^{(\mathrm{in})}) + \phi^2 \mathrm{var}(S_x) \approx \mathrm{var}(S_y^{(\mathrm{in})}) = N_P/4, \tag{3.6.3}$$

and that the signal-to-noise ratio equals one when $\langle S_y^{(\mathrm{out})}\rangle^2 = \mathrm{var}(S_y^{(\mathrm{in})})$, i.e., when

$$\frac{t_0^2 \gamma^2}{\hbar^2} N_P^2 \left(\alpha^{(1)} + \beta^{(1)} \gamma N_P\right)^2 (J_z^{(\mathrm{in})})^2 = \frac{N_P}{4}. \tag{3.6.4}$$

We can identify the value of $J_z^{(\mathrm{in})}$ that solves eq. 3.6.4 as the sensitivity, or precision of the estimation, δJ_z. We find

$$\delta J_z = \hbar \left| t_0 2\gamma (\alpha^{(1)} N_P^{1/2} + \beta^{(1)} \gamma N_P^{3/2}) \right|^{-1}. \tag{3.6.5}$$

Thus the sensitivity will have a transition from shot-noise to SH scaling with increasing N_P. As indicated in figure 3.5.1, there are points in the spectrum where either $\alpha^{(1)}$ or $\beta^{(1)}$ vanish, allowing pure nonlinear or pure linear estimation of the same atomic variable.

Moreover, an unpolarized input state $\langle(S_x, S_y, S_z)\rangle = (0, 0, 0)$ gives rise to dynamics dominated by the $\beta^{(0)}$ terms $\propto S_z^2$, sometimes called the "one-axis twisting Hamiltonian." This describes a self-rotation of the optical polarization, and can be used to generate polarization squeezing and also to obtain sensitivity

scaling as $N_P^{-3/2}$ in the estimation of $\beta_J^{(0)} J_0 + \beta_N^{(0)} N_A$, using an entanglement-generating strategy described in reference [Boixo et al., 2008a].

CHAPTER 4

Numerical Simulations

In the previous chapter we presented the analytic model for our proposed implementation of nonlinear metrology using light-atom quantum interfaces. We derived a nonlinear effective Hamiltonian and, following Boixo's guidelines, we guessed an expected dependence of the sensitivity, δJ_z, on the number of probing photons, N_P.

With this chapter we want to communicate that having considered only this analytic model was not enough, and we needed to verify other aspects before betting on the experimental reliability of our estimation protocol.

In particular for this experiment, there are phenomena not accounted for in the effective Hamiltonian which could lead to significantly different results. Examples are temporal dependence of the electronic excitation, relaxation and spontaneous emission effects as well as geometrical matching of the light and atomic systems.

Our interest was thus in predicting the performances of our metrology protocol in a scenario which is as close as possible to the real one in the experiment. The approach we took and which we will describe next is the following:

- We begin with the geometrical and propagation issues and we learn how to connect the overall result of the interaction, i.e., the polarization rotation, ϕ, due to the quantity J_z, to the spin dynamics of a single-atom when this is excited by the probing light.
- We proceed to numerically solve the single-spin evolution under different illumination conditions. In this way we can follow in time the development of dipole polarizations within the electronic structure of the atom.

We can also study the final state of the atom when the light excitation has ended, and investigate incoherent process effects.

- Finally we come back to the geometry matching of the light and atoms, using the knowledge about single-atom to calculate an overall response from the whole cloud.

The approach of the calculations in this chapter is semiclassical, which in the language of radiation-matter interaction means that the atoms are treated as quantum objects but the field is assumed to be classical. Such an approach gives correctly the average rotation angle, $\langle\phi\rangle$, but is insufficient for calculating the noise, $\delta\phi$. To account for this we maintain the simple model of the light shot noise, presented in the previous chapter, which gives $\delta\phi = N_P^{-1/2}$.

As concerns the sensitivity and the metrological relevance of the interaction the rotation angle we are talking about is proportional to the quantity under estimation. In this case, a simple propagation of errors gives:

$$\delta J_z = \langle J_z\rangle \frac{\delta\phi}{\langle\phi\rangle}. \tag{4.0.6}$$

A non-trivial dependence of $\langle\phi\rangle$ on N_P, which will result from the calculations, will have as a consequence the improved sensitivity scalings.

4.1. Mechanisms of polarization rotation: Maxwell-Bloch equations

In Sec. 3.6 of chapter 3, we introduced input-output equations for the system of collective operators, mutually interacting under the action of the effective Hamiltonian,

$$\begin{aligned} H_{\text{eff}} = 2\gamma\Big[&\big(\alpha^{(1)} + 2\gamma\beta^{(1)}S_0\big)S_zJ_z + \big(\alpha^{(2)} + 2\gamma\beta^{(2)}S_0\big) \\ &\big(S_xJ_x + S_yJ_y\big)\Big] + 4\gamma^2\big(\beta_J^{(0)}S_z^2J_0 + \beta_N^{(0)}S_z^2N_A\big). \end{aligned} \tag{4.1.1}$$

For example in the case of the Faraday rotation, i.e., linear polarization rotating into a different plane, the rotation angle about the z axis of the Poincaré sphere is

$$\phi \equiv S_y^{(\text{out})}/S_x^{(\text{in})} = 2\gamma t_0\hbar^{-1}(\alpha^{(1)} + \beta^{(1)}2\gamma S_0)J_z^{(\text{in})}, \tag{4.1.2}$$

and as reminder, $\gamma = \hbar\omega Z_0/2TA_0$. We would like to predict the quantity ϕ by calculating the output Stokes components knowing the input polarization and initial atomic state, as well as experimentally relevant details of the interaction, i.e., geometry, intensity, detuning, density of atoms, etc.

We immediately see that to calculate ϕ we have to know more details about the interaction, for example the effective area A_0. Also we notice that the time dependance is not trivial, since two time factors appear in the formula: the characteristic time of the light mode, T, and the interaction time t_0. In the simple assumption of having a constant Hamiltonian kept ON for a well defined duration, much longer than any characteristic response of the atoms, the two factors coincide. But this is not always the case.

Indeed, we are interested in the probing light not in a slow, quasi-static regime. We think that a fast pulsed probing regime is preferable for many reasons: first of all, we expect that a probing regime faster than relaxation time of the atoms will put more in evidence meteorologically useful nonlinearities, which otherwise would be wiped out by incoherent relaxation processes.

Moreover, with a pulsed probe we can perform time-resolved metrology and follow interesting time dynamics of the system under investigation, i.e., directly the atoms and indirectly the magnetic field. Pulsed probing also facilitates suppression of low-frequency electronic and technical noise, i.e., fluctuating laser intensity, via comparing the results of two successive observations.

When we assume for the light system a time-varying profile of the intensity, as a consequence we also have to consider that such a pulse propagates over the region of space where the atomic system is located. Anyway, we will always be in the regime where the atomic cloud is well contained within the spatial extension of the pulse of photons: our atomic sample is few millimeters long and the pulses we consider are not smaller than nanoseconds, which correspond to length of tens of centimeters. This fact simplifies all the propagation issues.

More in detail, we will proceed with integrating the Maxwell-Bloch equations in three spatial dimensions $\mathbf{x} = (x, y, z)$ plus

time t. Considering the slowly-varying-envelope approximation and using retarded coordinates $\zeta \equiv z$ and $\tau \equiv t - z/c$, the field envelope $\boldsymbol{\mathcal{E}}(\mathbf{x}, \tau)$ and the single-atom density operator $\rho(\mathbf{x}, \tau)$ obey the coupled equations

$$\mathcal{D}\boldsymbol{\mathcal{E}} = \frac{k^2}{\varepsilon_0}\boldsymbol{\mathcal{P}} \tag{4.1.3}$$

$$\partial_\tau \rho = \frac{i}{\hbar}[\rho, h(\boldsymbol{\mathcal{E}})] + \mathcal{L}_\Gamma(\rho). \tag{4.1.4}$$

For the field envelope as well as for the polarization envelope, $\boldsymbol{\mathcal{P}}(\mathbf{x}, \tau)$, we are considering only the positive frequency part, for simplicity.

The first equation is the well known paraxial wave equation (PWE), where $\mathcal{D} \equiv \partial_x^2 + \partial_y^2 + 2ik\partial_\zeta$ and k is the wavenumber. The second one is commonly known as the Lindblad master equation for the density matrix, ρ, where h is the single-atom dipole interaction Hamiltonian and $\mathcal{L}_\Gamma$ is the Liouvillian describing relaxation. The two equations are coupled by the Hamiltonian, which depends on the light field envelope, and by the polarization envelope, which is calculated on the atomic state,

$$\boldsymbol{\mathcal{P}} \equiv n\mathbf{p} = n\mathrm{Tr}[\rho \mathbf{d}_\downarrow], \tag{4.1.5}$$

where n is the local atomic number density and $\mathbf{d}_\downarrow$ is the dipole operator describing downward transitions.

We can interpret the system of coupled equations observing that while, according to eq. 4.1.3, the atomic polarization acts as a source of radiated field, at the same time, according to eq. 4.1.4, the light excites atomic polarization. The process explaining the polarization rotation, which is valid both for linear and nonlinear interaction, is indeed the interference happening in the forward propagating direction between the incoming light and the new, i.e., with a different phase, light coming from the excited, polarized atoms.

We assume that the field radiated by the polarized sample is a small perturbation with respect to the total light field, i.e., the rotation angle $\langle\phi\rangle \ll 1$. Thus we solve to first order in N_A as follows: We identify a solution to the zero-atom equation $\mathcal{D}\boldsymbol{\mathcal{E}} = 0$ as the input field $\boldsymbol{\mathcal{E}}^{(\mathrm{in})}$. Specifically, we can take

for example a vertically polarized input field and factorize the spatial mode, $M(\mathbf{x})$, from the temporal envelope. We thus have $\boldsymbol{\mathcal{E}}^{(\mathrm{in})} = \mathcal{E}_0 \mathbf{e}_V M(\mathbf{x})\sqrt{T(\tau)}$, where $\mathbf{e}_V$ is the unit vector in the vertical direction, and $|\mathcal{E}_0|^2$ is the total energy of the pulse. For the intensity temporal envelope we can imagine having a Gaussian pulse

$$T(\tau) = \frac{2}{w_\tau\sqrt{2\pi}} \exp\left[-2\tau^2/w_\tau^2\right] \tag{4.1.6}$$

with FWHM equal to $w_\tau\sqrt{2\ln 2}$.

We find numerically the solution to eq. 4.1.4 with $\boldsymbol{\mathcal{E}} = \boldsymbol{\mathcal{E}}^{(\mathrm{in})}$ as the lowest-order atomic response $\rho^{(1)}$, and from this we calculate $\boldsymbol{\mathcal{P}}^{(1)}$. We will fully describe in the next section our numerical approach for Lindblad master equation and its results.

The evolving atomic polarization $\boldsymbol{\mathcal{P}}^{(1)}$ generates a field $\boldsymbol{\mathcal{E}}^{(1)}$, which can be calculated using the Green function, G, for the PWE. We can write

$$\boldsymbol{\mathcal{E}}^{(1)}(\mathbf{x},\tau) = \frac{k^2}{\varepsilon_0}\int d^3x'\, G(\mathbf{x},\mathbf{x}')\boldsymbol{\mathcal{P}}^{(1)}(\mathbf{x}',\tau), \tag{4.1.7}$$

where G solves the PWE for a delta-function source, $\mathcal{D}G(\mathbf{x},\mathbf{x}') = \delta^3(\mathbf{x}-\mathbf{x}')$.

Specific knowledge of the field in a particular location, i.e., a 2D integral on the surface of a photodetector, S_d, can be reconstructed upstream in the beam using Green function techniques [Mitchell, 2009], finally arriving to a 3D integral of its sources:

$$\int_{S_d} d^2x d\tau\, \mathcal{E}_i^{(\mathrm{in})^*}\mathcal{E}_j^{(1)} = \frac{k}{2i\varepsilon_0}\int d^3x d\tau\, \mathcal{E}_i^{(\mathrm{in})^*}\mathcal{P}_j^{(1)}, \tag{4.1.8}$$

where with the suffix i and j we denote a specific polarization component.

In the exemplary case of linearly polarized input field along the vertical direction, we expect a rotation towards a diagonal direction. The detector will be thus responding to the S_y Stokes component, whose expression in terms of the light field in the specific H,V polarization basis is $S_y = I_{\diagup} - I_{\diagdown} = \mathcal{E}_V^*\mathcal{E}_H + \mathcal{E}_V\mathcal{E}_H^*$. The only possible field in the horizontal direction is the one radiated from the atoms, so the detected signal is the mean value of the operator, $\langle S_y\rangle \equiv (\hbar\omega Z_0)^{-1}\int d^2x d\tau\, \mathcal{E}_V^{(\mathrm{in})^*}\mathcal{E}_H^{(1)} + c.c.$,

and from the above discussion this signal is connected to the atomic polarization in the following way:

$$\langle S_y \rangle = (\hbar\omega Z_0)^{-1} \frac{k}{2i\varepsilon_0} \int d^3x\, n \int d\tau\, \mathcal{E}_V^{(\mathrm{in})^*} p_H^{(1)} + c.c. \tag{4.1.9}$$

The rotation angle results from the ratio of this value with the mean value of the input operator,

$$\langle S_x \rangle = (\hbar\omega Z_0)^{-1} \int d^2x d\tau\, |\mathcal{E}_V^{(\mathrm{in})}|^2 = (\hbar\omega Z_0)^{-1} |\mathcal{E}_0|^2. \tag{4.1.10}$$

4.2. Single-atom master equation

Let us focus in this section mainly to the temporal integral in eq. 4.1.9, that is like we consider no spatial dependance of the atom density or the light field, while calculating $\langle S_y \rangle$, as we were probing only one atom. Later on we will come back to the spatial integral and the geometrical issues.

As we said previously, the difficult part of the calculations is solving the Lindblad master equation 4.1.4 to find $\rho^{(1)}$, and calculating $\mathbf{p}^{(1)}$. The master equation itself is a differential equation for the single-atom density matrix,

$$\partial_\tau \rho = \frac{i}{\hbar}[\rho, h] + \mathcal{L}_\Gamma(\rho) \equiv \mathcal{L}(\rho). \tag{4.2.1}$$

The linear super-operator $\mathcal{L}$, called the Liouvillian operator, accounts for coherent dynamics as well as relaxation of the excited levels because of spontaneous emission. In particular, the non-unitary part of the Liouvillian acts on the density matrix in the following way:

$$\mathcal{L}_\Gamma(\rho) = -\frac{\Gamma}{2}(P_e\rho + \rho P_e) + \Gamma(\boldsymbol{\epsilon}^* \cdot \mathcal{D}_\downarrow)\rho(\boldsymbol{\epsilon} \cdot \mathcal{D}_\uparrow), \tag{4.2.2}$$

where P_e is the projector on the excited state manifold, which are the states affected by spontaneous decay, $\boldsymbol{\epsilon}$ is the unit vector in the spherical basis of polarization and $\mathcal{D}_\downarrow$, $\mathcal{D}_\uparrow$ are the lowering and raising operators, proportional to the dipole operator vector.

For the coherent part we decided to consider two contributions to the Hamiltonian: $h = h_\mathcal{E} + h_B$. The first one, which accounts for the interaction with the light field $\mathcal{E}$, is the rotating-wave-approximated, dipole-interaction Hamiltonian, calculated following the well known literature about alkali atom electronic

structure, e.g. Steck [Steck, 2009], exactly as done in section 3 of chapter 3.

With the second one we wanted to include the possibility of simulating the presence of a constant, weak[1] magnetic field. We consider a Zeeman-like Hamiltonian in the following way

$$h_B = -\mu_B g_F \mathbf{B} \cdot \mathbf{F} \tag{4.2.3}$$

where $\mathbf{F}$ are the angular momentum operators, μ_B is the Bohr magneton, and g_F are the hyperfine Landé g-factors for each F or F' manifold.

The usual approach consists in flattening the density matrix in a vector of all its elements, $\vec{\rho}$. If d is the dimension of the Hilbert space, 24 in the case of the D_2 line of ^{87}Rb, the flattened density matrix is a d^2 vector. In this way we have a system of d^2 differential equations,

$$\partial_\tau \vec{\rho} = \overrightarrow{\mathcal{L}}\, \vec{\rho}, \tag{4.2.4}$$

where $\overrightarrow{\mathcal{L}}$ is a $d^2 \times d^2$ matrix, acting on the flattened density matrix, which includes in a convenient way the action of several operators from the corresponding side they are supposed to act.

All these calculations involving operators, super-operators and flattened matrices are done very easy using a MATLAB toolbox dedicated to quantum-optics [Tan, 1999].

In the case of a time-independent Hamiltonian, the toolbox provides a very simple way to calculate the evolution at time t of a density matrix, giving an initial condition. At the basis of the method there is the diagonalization of the Liouvilian, which in our case is still a rather easy calculation with the Liouvilian being a $24^2 \times 24^2$ matrix. For the flattened density matrix we have the following exponential series:

$$\rho_j(t) = \sum_l (e^{\mathcal{L}t})_{jl} \rho_l(0) = \sum_k V_{jk} \left(\sum_l V_{kl}^{-1} \rho_l(0) \right) e^{s_k t}, \tag{4.2.5}$$

$$\vec{\rho}(t) = e^{\overrightarrow{\mathcal{L}}t} \vec{\rho}(0) = V e^{St} V^{-1} \vec{\rho}(0), \tag{4.2.6}$$

[1] We say that a magnetic field is weak if the energy shifts which causes are much smaller than the hyperfine splitting.

where S is the diagonal matrix of eigenvalues, $\{s_k\}$, of $\overleftrightarrow{\mathcal{L}}$ and V is the square matrix, built column-by-column from its normalized eigenvectors.

With the knowledge of the density matrix at any successive time, we can calculate the expectation values of all the most interesting operators and how those evolve: for example the population of specific levels, the coherences between two levels, the single particle pseudo-spin operators, and so on.

In the language of the MB equation treatment we presented in the previous section, we can calculate the atomic polarization as the lowest-order atomic response, i.e., the expectation value of the dipole operator, $\mathbf{p}^{(1)} = \mathrm{Tr}[\rho^{(1)}\mathbf{d}_{\downarrow}]$, and calculate the rotation per atom.

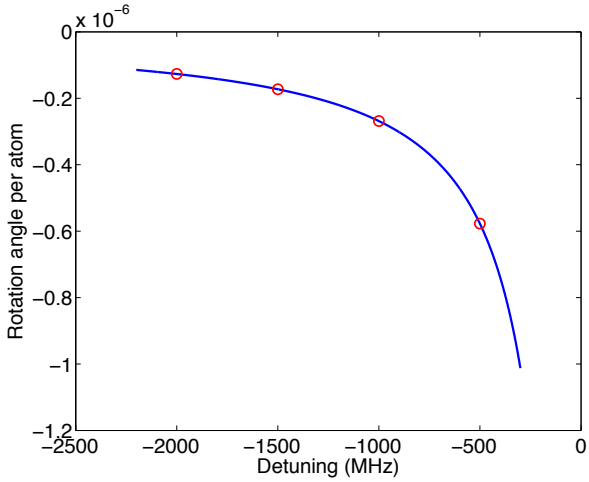

Figure 4.2.1. Comparison of analytic and numerical models for Faraday rotation versus detuning in the linear probing regime. The blue curve reflects the dependance on detuning of $\alpha^{(1)}$ in the analytic expression of $\phi(\Delta)$, and the red circles correspond to $\phi^{(i)}$ numerically calculated at four different detunings. The mismatch, relatively small $\{|\phi^{(i)} - \phi(\Delta_i)|\} = \{0.6, 0.8, 1.3, 3\} \times 10^{-10}$, comes from numerical precision.

In fig. 4.2.1 we can see the perfect agreement of the two approaches, the analytical effective Hamiltonian and the MB equations numerically solved, for predicting the polarization rotation caused by a single atom. We compare them in a regime of illumination where the atomic response is certainly linear. We consider 10^4 photons distributed over 1 ms in a light beam with 6×10^{-6} cm^2 of effective area, which correspond to a maximum intensity of 4×10^{-4} mW/cm^2, i.e., four orders of magnitude smaller than the saturation intensity for the D_2 transitions. Moreover we look at the comparison in a far-off resonant frequency regime. The value of J_z of a single, polarized atom is $1/2$; the initial state used in the script is $\rho(0) \equiv |F = 1, m_F = 1\rangle \langle F = 1, m_F = 1|$.

4.3. A simple example

In this section we want to give an idea of the things we can monitor or calculate using the numerical solving techniques for the Maxwell Bloch equation system in some simple scenario. For example we can simulate the effect of a magnetic field on the atom. We can imagine the atom initially in the $F = 1$ ground state and polarized as before to maximize J_z. We can set a magnetic field of 0.1 Gauss along the $x-$axis, which for our atom corresponds to a Larmor precession of 70 kHz.

We can also add the presence of light field: In Fig. 4.3.1 we see the population evolution of the 3 magnetic sublevels of the $F = 1$ manifold: blue for $m_F = 1$, green for $m_F = 0$ and red for $m_F = -1$. We can compare three different light illumination regimes: no light (solid line), intensity of the order of I_{sat} and -2 GHz (dashed line), and finally the same intensity but a much closer detuning of 462 MHz (dot-dashed line), for which the incoherent processes caused by the more aggressive illumination condition are strongly evident.

While we are on the topic of incoherent processes, it is a good moment to introduce the concept of damage, η. The damage is related to how different the state of the atom is after a period of illumination, T. With the simulations we can easy calculate a quantity to quantify such a change. In the space of the density

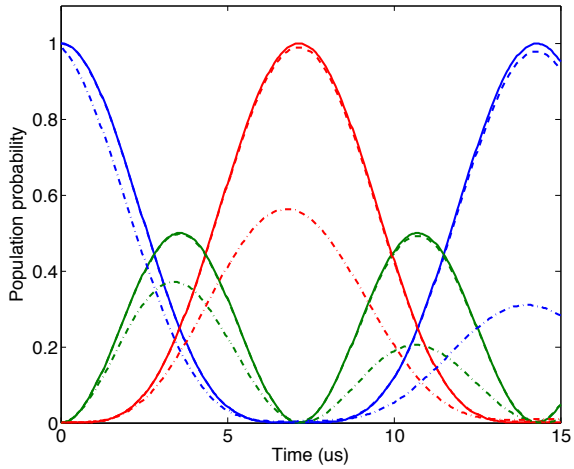

Figure 4.3.1. Illustration of atomic state decoherence due to probe-induced spontaneous scattering (simulation). The population evolution of the three magnetic sublevels in the $F = 1$ ground state: $m_F = 1$ in blue, $m_F = 0$ in green and $m_F = -1$ in red. Solid lines are for probing light off, dashed lines are for light OFF and far detuning, dot-dashed lines are for probing light ON and closer detuning.

matrices, in fact, the fidelity introduced by Jozsa [Jozsa, 1994],

$$F(\rho,\sigma) = \left(\mathrm{Tr}\left[\sqrt{\sqrt{\sigma}\rho\sqrt{\sigma}}\right]\right)^2 \tag{4.3.1}$$

gives the possibility of defining a distance between quantum states. We take this distance as our definition of damage of to the atomic state,

$$\eta = 1 - F(\rho(0), \rho(T)). \tag{4.3.2}$$

4.4. Steps and pulse dynamics

Until now we have presented the simulations in a regime of constant illumination. Conversely, as we said at the beginning of the chapter, a pulsed probing regime is closer to a real experimental situation. We had to modify the strategy to solve the master equation 4.1.4. Simply, we choose to split the evolution

in steps of length dt sufficiently small for considering the illumination constant and applying in this way the exponential series method presented above, step-by-step:

$$\vec{\rho}(t_{i+1}) = e^{\overrightarrow{\mathcal{L}}dt}\vec{\rho}(t_i). \tag{4.4.1}$$

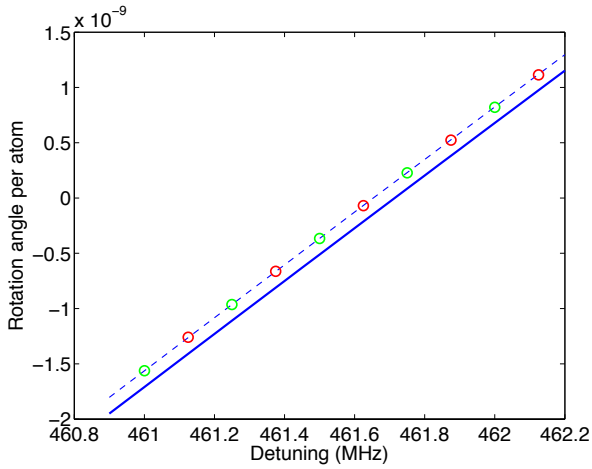

Figure 4.4.1. Comparison of Faraday rotation versus detuning as predicted by simulation (pulsed and CW) and by analytic model. Red circles are results of simulation assuming constant illumination regimes, and green circles are for 1 ms FWHM Gaussian pulse. The blue line is the expected rotation depending on the detuning as from the analytic expression. The dashed line is for comparing the small mismatch between both numerical methods and the analytic one. The detuning is referred to $1 \to 0'$ transition.

This strategy is definitively time consuming: for example 100 steps are calculated in about 5 minutes. Anyway most of the scenarios we are interested in simulating do not involve the $F' = 3$ excited level. If we neglect this level the Hilbert space dimension reduces to 17 and this speeds up the calculation time by a factor of 5-6. For our purposes this is an acceptable trade-off between time and accuracy. Anyway probably better performances could be obtained applying some kind of 4th order

Runge-Kutta method for density matrices, or performing the numerical resolution in a C++ code external to MATLAB.

We can evaluate the performances of calculations in the pulsed regime by comparing their results and the ones with constant illumination regime in a linear probing scenario. For example we can look for the zero crossing of the rotation angle in the proximity of the magic detuning.

In figure 4.4.1 we show the results of three different calculation methods: the solid blue line is the rotation vs. detuning predicted via the analytic expression of $\alpha^{(1)}$. The green circles are the results of simulations with the illumination having a Gaussian time dependance, with 1 ms of FWHM divided into 100 steps, for a total number of 10^4 photons in the pulse. The red circles are instead the results of simulations assuming a constant illumination regime with intensity equivalent to the average intensity of the pulsed regime.

We can see that the two numerical methods give the same results, although there is a small mismatch with the analytic calculations. Indeed, the analytic zero crossing is expected at 461.714 MHz, while the numerical seems shifted by the equivalent of 61 kHz (depicted in the graph by the shifted dashed line). Anyway the mismatch is small if we account typical experimental laser linewidth ($\sim$ 200 kHz) and in the vertical axis it is of the same amount as for the far off-resonant regime (see caption of fig. 4.2.1).

As mentioned, we want to have simulation results in situations as close as possible to the experimental conditions. In our lab we create pulses of light using acousto-optical modulators, as we will see better in the following chapters. We needed to do simulations including the non-zero raising/falling time of the physical pulses.

We can generate a stepwise rising edge profile which simulates the switching ON of an AOM by an accumulating sum of a Gaussian function, in analogy of the well known error function. We can define:

$$T_{EF}(t_{i+1}) = T_{EF}(t_i) + T_G(i\,dt - \tau_0), \tag{4.4.2}$$

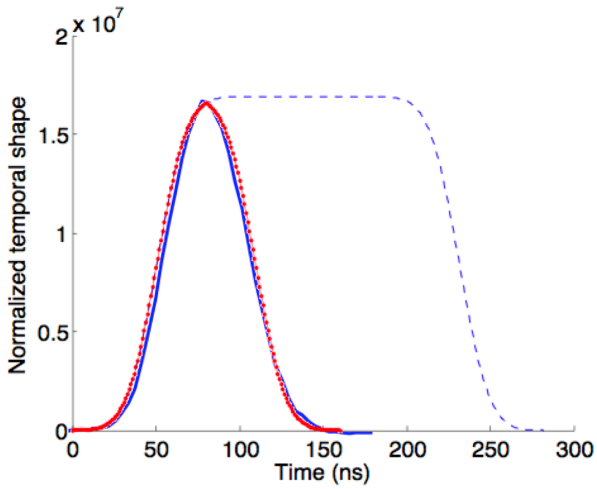

Figure 4.4.2. Illustration of the the pulse shape function used in the simulations. In dashed blue a possible curve for simulating a long AOM pulse, with its rising, constant and falling profiles. Red dots are for the specific shortest 54 ns FWHM stepwise profile we used in the simulations. In blue, a vertical rescaled trace from a photodetector for comparison with the real experiment.

where $T_G(\tau)$ is a Gaussian time profile such as the one in eq. 4.1.6 parametrized by its waist w_τ. We set $T_{EF}(t_0) = 0$, dt is the step size of our chosen time discretization and τ_0 is equal to two w_τ. In this way the relation between the 10-90 rise time of T_{EF} and w_τ is $\approx$1.28 to 1.

We can join to the rising edge profile an interval where the value of the pulse is constant, even with a different numerical resolution if we need so, and finally we can join a falling edge reproducing symmetrically the initial behavior.

The shortest pulse we can physically create in our lab has 54 ns of FWHM. Its shape is very close simulated by stopping the rising profile T_{EF} at 98% of the maximum value and immediately joining a symmetric falling edge (see fig. 4.4.2). This will be the time profile we used for simulating the nonlinear probing, explained in the following sections.

4.5. Simulating the nonlinear probing

We used the described stepwise integration technique for simulating the nonlinear response of the atom to the incoming probe light. We expect to see that the rotation depends on the photon number, as from the analytic prediction,

$$\phi = 2\gamma t_0 \hbar^{-1}(\alpha^{(1)} + \beta^{(1)} 2\gamma S_0) J_z^{(\mathrm{in})}, \tag{4.5.1}$$

where $S_0 = N_P/2$. We would like to make evident the nonlinear contribution of the rotation, for this reason we do the simulation at the detuning where we expect to suppress the linear susceptibility, i.e., $\alpha^{(1)} \approx 0$.

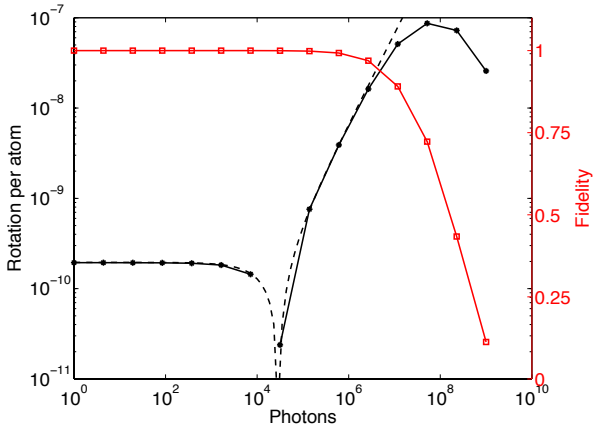

Figure 4.5.1. Numerical and analytical predictions for Faraday rotation angle and fidelity between initial and final atomic state as a function of photon number at the "magic" detuning. The black points are the absolute value of the calculated rotation. The dashed curve is the expected rotation calculated with the analytic formula. Both black dataset are split into two curves because of a change of sign not visible in the log scale. The red points are the fidelity between the atomic state before and after the probing pulse.

As we learn from the graph in fig. 4.4.1, the detuning of 461.65294 MHz satisfies this requirement for a ms long pulse. We choose to keep this detuning also for the 54 ns long pulse,

even if in that condition a residual linear susceptibility is present due to the different spectral properties of the shorter pulse. A finer choice of the detuning could have removed such a residual linear susceptibility; anyway in a real experiment, claiming a detuning precision of few Hz, when the pulse bandwidth is of some tens of MHz is somehow unphysical.

We simulated pulses with photon number up to 10^9. In fig. 4.5.1, we clearly see the rotation angle depending on the incoming photon number. The graph is in a log-log scale to better identify the power-law dependance, for the logarithm to be showed correctly we plot the absolute value of the rotation angle.

We identify three regions: below 10^3 photons the residual linear susceptibility dominates until the nonlinear response start to become comparable around 10^4. Because the linear and nonlinear act in different directions this produces a change of sign. In the range from 10^5 to 10^7 photons we see a clear proportionality of the rotation with the photons, sign of the expected nonlinear susceptibility.

For the comparison with the analytic expression of eq. 4.1.2 we have to consider that the intuitive correspondence between the two temporal factors t_0 and T is not valid anymore as for the simple linear case with long probing pulses. Keeping the two factors as free parameters, we found that the analytic expression matches the simulations with the following choice: $t_0 = 150$ ns and $T = 112.5$ ns. dashed curve in the figure.

In the last region, with photon number above 10^7, the rotation significantly deviates from the analytic expression. We interpret this as an effect of the change in the atomic state because of incoherent scattering due the high levels of illumination. For this reason we also plot in red the calculated fidelity between the initial and final atomic state, noticing that the deviation from the expected rotation is correlated with the fidelity going below 80%. We investigated more details about the damage and its relation with the nonlinearity. This will be the argument of the next section.

4.6. Damage and nonlinearity

As we said before our understanding of what happens at very high photon number, i.e., the deviation from the predicted dependance of the rotation on the number of probes, is that incoherent scattering changes the atomic state. Such optical pumping effects at high level of illumination can be easy demonstrated by observing the evolution of population in other levels different from the initial atomic state. In fig. 4.6.1 we see how the population of the excited states evolves during the pulse, how the atoms accumulate into the $F = 2$ manifold, and how the atoms change magnetic sublevel within the $F = 1$ manifold.

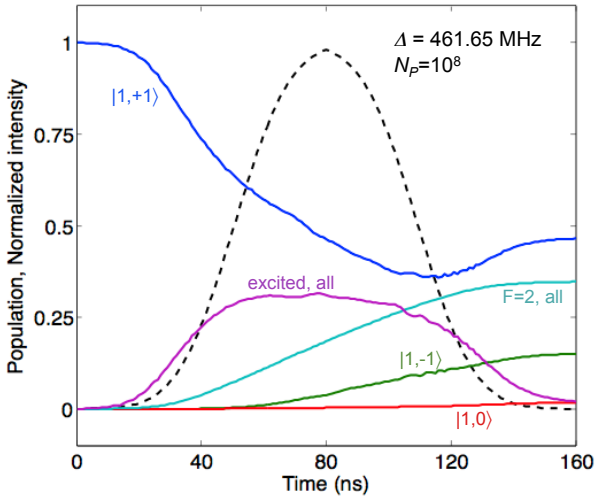

Figure 4.6.1. Evolution of the atomic population among the hyperfine level manifold in a specific probing condition (detuning and photon number). Blue, green and red lines are the populations of the three magnetic substates in $F = 1$, as labelled. Light blue line is the sum of all the population in the $F = 2$. Purple line is the sum of all the population in the excited states. Dashed black line is the normalized light intensity profile.

At high levels of illumination, the fact that the rotation is affected by such optical pumping effects is itself a nonlinear response of the atoms: more photons means more optical pumping which results in more rotation changing. How to distinguish between these nonlinearities, which we can denote as bad ones, from the one we instead want to use to sense the atoms? How can be sure that the response we simulated in the range between 10^5 and 10^7 are not caused by optical pumping nonlinearities?

We played some tricks to investigate these questions. In the script is relatively simple to make the probe insensitive to specific sublevels: It is just a matter of arbitrarily putting to zero the matrix elements of the dipole operator between the sublevels we want to "silence", and the excited state manifold.

We apply this strategy for silencing the effect of the atom pumped into the state $|m_F = -1\rangle$ as well as for silencing all the effects from the $F = 2$ manifold. We compare the results and find no significant difference caused by the optical pumping in the range of interest.

Another tool we have in the scripts for tweaking the effects of incoherent processes is to artificially change, for example to reduce, the decay rate Γ. Such a change has two effects. First of all the off resonant scattering rate, hence the damage, reduces consequently. Under the same probe intensity, damage goes proportionally to $(\Gamma/\Delta)^2$ [Grimm et al., 2000; Foot, 2005].

Unfortunately also the signal reduces. We can see this from the analytic expression of the coefficients inside the Hamiltonian, see eq. 3.5.8 and 3.5.10 of chapter 3. The αs coefficients are proportional to the square of the D_2 transition dipole matrix element $\langle J|\,|er_q|\,|J'\rangle \equiv D_{JJ'} \propto \Gamma^{1/2}$. The βs coefficients instead are proportional to $D^4_{JJ'}$. Summarizing, the αs are proportional to Γ and the βs to Γ^2.

An interesting question is the trade-off between nonlinear signal and damage. In the simulations, we have seen that by increasing the photon number the response of the atoms in term of rotation angle increases, until the point where the damage, we can visualize it from the plotted fidelity, stops this trend. By the proportionality argument it seems that having a lower scattering rate would be compensated by a lower β. There should

be no relevant change in the value of the maximum achievable signal obtained from an atom before the damage starts playing its undesired effects.

We simulated this hypothetical scenario by changing the value of Γ from the correct one for ^{87}Rb of ≈ 6 MHz to the arbitrary value of ≈ 6 kHz, indeed reducing it by three orders of magnitude. We can in part confirm the analytic argument about the absence of any improvement by comparing fig. 4.6.2 (A) and fig. 4.5.1.

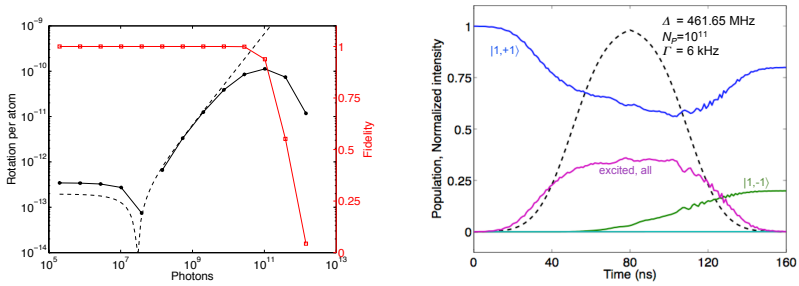

(a) Train of long pulses **(b)** Single short pulse

Figure 4.6.2. Nonlinear probing assuming kHz decay rate. (A): With respect to the case of normal conditions for Γ, simulations reproduce qualitatively similar results, both in the rotation and in the fidelity, but at higher photon number. The roll-off of the rotation happens at lower damage instead, reducing the range of exploitable nonlinearity. (B): In comparable conditions of fidelity as for fig. 4.6.1, the final atomic population is only shared between the two states $|1, \pm 1\rangle$ connected via coherent processes. The contribution of $|1, 0\rangle$ as well as the $F = 2$ state is not appreciable at all.

In addition, the simulations with the fictitious Γ return a worse trade-off. The deviation of the simulated rotation angle from its predicted value seems sensitive to smaller level of damage. Moreover, by looking at the population distribution after the pulse in fig. 4.6.2 (B), we can find evidences for a dominant role of coherent processes, such as Raman scattering, which populates the state $|1, -1\rangle$, at the expense of incoherent relaxation

processes, which should for example populate the $F = 2$ manifold.

4.7. Geometrical mode-matching

We have shown how to use numerical computation power to get information about the interaction of a single atom with a probing light field. In this last section of this chapter we come back to the 3D model of the interaction. We now want to account for the fact that the atoms have a specific density distribution inside the trap, at the same time that they are probed by photons within a specific light mode. Finally, we would like to know how the single-atom response, which we are able to calculate numerically, translates into a global response of an inhomogeneous interface of atoms and photons.

Let us recall the main result of the calculations in section 4.1: the equation by which we can calculate the signal from the atoms. In the case of calculating rotation of linear polarization we have for example:

$$\langle S_y \rangle = (\hbar\omega Z_0)^{-1} \frac{k}{2i\varepsilon_0} \int d^3x\, n \int d\tau\, \mathcal{E}_V^{(\mathrm{in})*} p_H^{(1)} + c.c.\,, \tag{4.7.1}$$

where, as a reminder, $\mathcal{E}_V^{(\mathrm{in})} = \mathcal{E}_0 \mathbf{e}_V M(\mathbf{x}) \sqrt{T(\tau)}$.

Using the previously described stepwise integration technique, we know how to calculate the temporal overlap integral in eq. 4.7.1, for a specific pulse energy $|\mathcal{E}_0|^2$ and a specific initial atomic state, assuming $M(\mathbf{x}) = 1$.

Now that we want to account for the spatial distribution instead, we can proceed in the following way: via interpolation, for example, we can convert the discrete results from a set of simulations at different pulse energies, $\{|\mathcal{E}_0|^2\}_i$, into an explicit continuous, analytic functionality of the temporal overlap integral with directly the total photon number and the beam spatial distribution:

$$\left\{ \int d\tau \left(\mathcal{E}_V^{(\mathrm{in})*} \right)_i p_H^{(1)} + c.c. \right\}_i \overset{\text{interp.}}{\longrightarrow} \Theta\left(N_P, M(\mathbf{x})\right). \tag{4.7.2}$$

We can thus predict the overall response from the whole atomic cloud by calculating the following 3D overlap integral,

$$\int d^3x\, n(\mathbf{x})\, \Theta\left(N_P, M(\mathbf{x})\right), \tag{4.7.3}$$

where we can include the total number of atoms and all the geometrical relevant parameters of the interface. As we will show in the next chapter, in the analysis of the experiment we finally used this approach for providing a model to the data.

4.7.1. A qualitative study. At this point, we know that the single atom polarizability has a complicated dependence on the incoming field, in particular at high field intensity, where optical pumping happens. Regardless, there is some useful information we can still extract from the 3D integral assuming the simplest nonlinear response of the atoms.

Let us consider the single atom polarizability up to the first non-zero nonlinear order. For the goal of this qualitative study we can neglect any tensorial description of how the various polarization components interplay and simply deal with scalar field and polarizability:

$$p^{(1)} = A\mathcal{E}^{(\mathrm{in})} + B|\mathcal{E}^{(\mathrm{in})}|^2\mathcal{E}^{(\mathrm{in})}, \tag{4.7.4}$$

where we can easily identify a linear and a nonlinear contribution to polarizability. The temporal integral of eq. 4.7.1 will thus simply results in a part proportional to the field intensity, $I \propto |\mathcal{E}^{(\mathrm{in})}|^2$, and another to the field intensity squared.

Having said that, for the spatial dependence we can consider the two following overlap integrals:

$$\mathcal{O}_L = \int d^3x\, n(\mathbf{x}) I(\mathbf{x}) \tag{4.7.5}$$

$$\mathcal{O}_{NL} = \int d^3x\, n(\mathbf{x}) I(\mathbf{x})^2. \tag{4.7.6}$$

A priori, we see see that the geometrical properties of the interface will have different effects on the linear and the nonlinear probing. How much is this relevant? Another interesting question is for example the comparison between a fully homogeneous model for the interface of both the atomic and the photonic system, and any real non trivial spatial distribution.

For the atom distribution, let us consider a Gaussian with FWHM $w_r\sqrt{2\ln 2}$ and $w_z\sqrt{2\ln 2}$ in the transverse and longitudinal directions, respectively:

$$n(\mathbf{x}) = 2\sqrt{2}(\pi^{3/2} w_z w_r^2)^{-1} \exp[-2r^2/w_r^2] \exp[-2z^2/w_z^2] \tag{4.7.7}$$

where $r^2 \equiv x^2 + y^2$. This cigar-like distribution is a first simple guess of the shape of the atomic cloud as this is held in a single beam optical trap. It is calculated in the case of the thermal energy much smaller than the potential well, approximating the trapping potential with quadratic functions. Describing the experiment in the next chapters, we will see that this guess is not far from being correct, with the difference that in the longitudinal axis the real shape is instead closer to a Lorentzian function. For the moment, we can continue assuming a Gaussian longitudinal profile without much complications.

Moreover we can consider that the light field mode is a simple Gaussian beam,

$$M(\mathbf{x}) = \sqrt{\frac{2}{\pi w^2(z)}} \exp[-r^2/w^2(z)] \exp[i\psi(r,z)] \tag{4.7.8}$$

where $w^2(z) = w_0^2(1 + z^2/z_R^2)$, w_0 is the beam waist at the focus, $z_R = \pi w_0^2/\lambda$ is the well known Reyleigh length, and ψ is the wave-front phase,

$$\psi(r,z) = -k\left(z + \frac{r^2}{2z\left(1 + z_R^2/z^2\right)}\right) + \arctan\left(\frac{z}{z_R}\right). \tag{4.7.9}$$

We can also introduce an effective area

$$A_0 \equiv \int dxdy\, |M(x,y,z)|^2 / |M(0,0,z)|^2 = \pi w_0^2/2. \tag{4.7.10}$$

We can assume that the focus of the light mode coincides with the center of the atomic cloud, as well as the main axis, but other scenarios can be considered without much complication. We can reasonably expect that the relevant parameters would be the Gaussian waists, i.e., the ratios between them. For example if we choose a typical aspect ratio for the cigar-shape atomic cloud of 150:1, and we quantify the matching between the atom

size and the light mode with the parameter ζ,

$$\zeta = \frac{w_0}{w_r}, \tag{4.7.11}$$

being the ratio between the two waists, we can plot how $\mathcal{O}_L$ and $\mathcal{O}_{NL}$ depend on ζ (see fig. 4.7.1). For the homogeneous model,

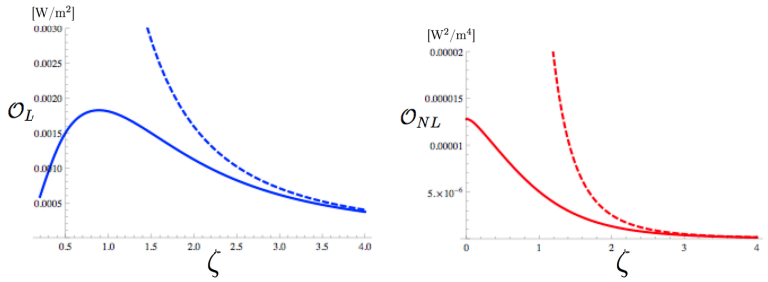

Figure 4.7.1. Linear and nonlinear overlap integrals as a function of transversal mode matching. The blue curves in the plot on left correspond to the linear signal. The red ones, on the right, are for the nonlinear signal. The dashed lines are for the homogeneous model. $\zeta = w_0/w_r$.

the dashed lines in fig. 4.7.1, we consider that the light mode is a cylinder of area A_0, and all the atoms are inside the cylinder. Since we are considering that the atom density is normalized in the whole space and the intensity in any transversal plane, i.e.,

$$\int d^3x\, n(\mathbf{x}) = 1\,, \quad \int dxdy\, I(\mathbf{x}) = 1\,\mathrm{W} \tag{4.7.12}$$

we thus have that $\mathcal{O}_L^{(hom)} = 1\ \mathrm{W}/A_0$ and $\mathcal{O}_{NL}^{(hom)} = 1\ \mathrm{W}^2/A_0^2$.

Regarding the case of the linear interface, we learn from the maximum in the curve that matching the transversal dimensions of the two systems is important for indeed maximizing the signal. The case is different for the nonlinear signal where the maximum is theoretically expected at infinite focusing of the light probe in the middle of the atom cloud. We can explain this last situation because the nonlinear signal is proportional to the intensity square, which means inversely proportional to w_0^4. Conversely, the relevant volume in a Gaussian mode is roughly $w_0^2 z_R$, where

the Rayleigh length is proportional to w_0^2. The optimality is thus simply established by the atom distribution, which in our case is highest in the center.

Of course this last result is misleading, since does not account for the fact that above some levels of intensity the response from the atoms degrades for the reasons explained in the previous sections.

Finally we can look at fig. 4.7.2 for analyzing inhomogenous vs. homogeneous interface. The main point is that close to the optimal matching condition $t \approx 1$ to 2, $\mathcal{O}_L$ is only a fraction, 20 to 60 percent, of what should be in the case of homogeneous interface. The situation for $\mathcal{O}_{NL}$ is accentuated. This fact can be interpreted as if the atoms in the cloud do not contribute all in the same way to the signal, and this in average reduce the signal. In particular the atoms in the center, where the beam is focused, contribute more than the atoms in the tails, and this is much more relevant for the nonlinear probe.

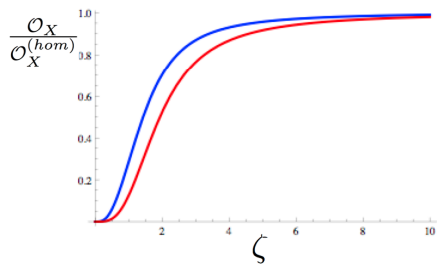

Figure 4.7.2. Comparison between homogeneous and inhomogeneous interface. The blue curve corresponds to the ratio of the signals from the two models in the case of the linear interface. Similarly, the red one is for the nonlinear interface.

To simplify the argumentation, our goal is to estimate the collective variable, e.g., the total spin, of the sample, but in fact by using the linear or the nonlinear atomic response to probe light we gather information about two differently weighted functions of the collective atomic variable.

In any classical scenario, this is not a problem. In particular, if we always guarantee that the variable is homogeneously distributed among the whole sample, then the two measurements will only differ by a constant factor. For the scope of our experiment, it is ok having a simple constant factor, for example when calibrating the nonlinear measurement using the linear one. In the next chapters, when describing the initial state preparation via optical pumping, we will further discuss the achievable homogeneity we can expect.

CHAPTER 5

Experimental setup

In this chapter I will present the details of the apparatus with which we implement in our lab the polarization-based quantum interface between light and cold atoms.

In chapters 3 and 4, we proposed nonlinearity in the light-atom interfaces as a resource for metrology from a theoretical perspective. In the way that we developed the theory, for example the interaction Hamiltonian, it was easy to identify the collective pseudo-spin component J_z as the candidate to be the object of the metrological investigation.

Now that we want to focus more on experimental issues, we decided instead to stress on the real spin component F_z, because it has for example more direct connections with magnetometry. Anyway, it is just a matter of convenience since the two quantities only differ by a numerical factor, $J_z = F_z/2$.

The description will follow all the requirements, a sort of check-list, for the experiment to succeed. From what said in the previous theoretical chapters, what we need is the following:

- Efficient polarization-based quantum interface between atoms and light. This means that we are able to collect enough atoms, prepare the correct pulse of photons and make both systems interacting as predicted theoretically. A high optical depth, the figure of merit of the quality of the interface, indicates that the desired nonlinear dynamics will show up before other undesired effects and in such a way we can expect that the only relevant noise sources are the fundamental, quantum ones.
- Easy addressing and switching between different probing regimes. We do it by controlling the intensity, the

time profile and the detuning of the photon pulses used for interrogating the atoms.
- Shot-noise-limited detection; so that the electronic or technical noise of the used photodetectors do not affect the sensitivity, in the range of photons where we expect to see better-than-Heisenberg scaling.
- Good control of the atomic sample magnetization, with particular care to the uniformity of the spin polarization all over the cloud for simplifying the relation between the linear and the nonlinear measurement.

On this scheme we will structure the rest of the chapter.

5.1. Description of cold-atom machine

As in the majority of experiments with cold atoms, most of the time in the lab is spent on taking care of the system for generating and trapping the atomic cloud. The apparatus we work with in our lab has passed through many hands and has been used for many experiments since its beginning. Before I started the PhD, the vacuum system, for example, was physically moved twice: from Innsbruck to Barcelona and after a couple of years from downtown Barcelona to ICFO's actual location in Castelldefels. The vacuum never got broken and for this reason Jürgen Eschner, the professor who started the trap, is proud to say that there is still good, Austrian vacuum inside.

The atomic trap is described in details in the thesis of previous students. Matthias Schulz [Schulz, 2002] and Herbert Crepaz [Crepaz, 2007] built in Innsbruck the vacuum system, and both the magneto-optical and the dipole traps with the goal of collecting single atoms; Marcin Kubasik [Kubasik, 2009] upgraded the dipole trap for working with many atoms, instead, and built the polarization interferometer demonstrating control of the initial atomic preparation via optical pumping. Marco Koschorreck [Koschorreck, 2011] implemented an absorption imaging system and by working on magnetic field compensation he enhanced the coherent time of atomic preparation. This, together with a two-polarization probing, which Marco

also implemented, was the way to achieve spin-squeezing. During my PhD I overlapped with both Marcin and Marco, working together in this continuous effort in taking care of the "baby".

The final stage of the ^{87}Rb ensemble is a cloud of about one million atoms, held in a single-beam far-off-resonant dipole trap (FORT) [Grimm et al., 2000]. Its trapping potential is not enough to efficiently load room-temperature atoms, so the initial stage of the loading is done with a magneto-optical trap (MOT) [Metcalf and van der Straten, 1999], where the kinetic energy of the atoms is removed via an optical molasses.

Long trap-lifetime and a high loading speed are two features that depend in opposite ways on the background pressure in vacuum system. This is why our MOT is in fact a two-stage MOT. Two regions of the vacuum chamber are kept at different pressure by differential pumping. In the region with higher pressure, a two-dimensional MOT collects atoms from the background. Along the free dimension, the atoms are sent by a pushing beam into the region of the chamber having lower pressure. Here, a three-dimensional MOT captures the incoming atomic beam. The loading rate of the 3D MOT is about few 10^7 atoms per second. The temperature is fixed by the spontaneous decay rate of the excited level, $\Gamma \approx 2\pi \times 6 \times 10^6$ s^{-1}, corresponding to the Doppler limited temperature of 146 μK.

We cannot perform experiments with long coherence time of the ensemble of atoms in a running MOT, because of its very close to resonance laser beams and strong magnetic-field inhomogeneity. This is why we finalize the process of preparing the atomic ensemble into the FORT. The working principle of this trap is the following: the dipole interaction with light changes the ground state energy of atoms; this effect is known as the AC-Stark shift. In a focused beam a potential is then created, and the atoms can be attracted towards or repelled from the region of more intensity, respectively for red or blue detuning. In our case of laser beam at 1030 nm (the Rubidium doublet is at 780-795 nm), focused down to a waist of 52 μm, a power of 6 W creates a potential well equivalent to a temperature of 200 μK, $U = k_B T$.

Such a potential is capable of trapping the atoms from the MOT, but for the transfer to be very efficient a stage of sub-Doppler cooling is required. During the last milliseconds of the MOT loading the detuning of the cooling light is increased from 2Γ to 15Γ, the repumper light is dimmed to let the atoms accumulate into the lower energy ground state $F = 1$ and the quadrupole coils are switched off achieving in this way a pure molasses phase. The temperature is then lowered down to almost 25 μK, a good portion (almost 10%) of the atoms are transferred into the dipole trap and all the laser of the MOT are switched off.

In an optimized working regime, two seconds of loading time are enough to trap up to 1 million of cold atoms, ready to be used for the designed experiment. The lifetime on the atoms in the dipole trap exceeds the 30 seconds, allowing the possibility of repetitive experiments without the need of recapturing atoms.

Moreover an important advantage of having the atoms in the dipole trap is the shape of the ensemble. The geometry realized with a single focused beam ends up in a cigar-shape cloud. Using imaging techniques, both in fluorescence and in absorption, we measured a transversal Gaussian profile with a FWHM of 19.5 μm and a longitudinal Lorentzian profile with a FWHM of 3 mm [Koschorreck et al., 2011; Koschorreck, 2011].

With such a shape the atoms demonstrate a very high on-resonance optical depth (OD), a figure of merit of the high light-atom coupling, when illuminated along the longitudinal axis. As I will explain better in the following sections, we measured OD of the order of 50 with about 1 million atoms. To give a comparison, free-falling atoms from a MOT show typically OD one order of magnitude smaller.

5.2. Probing the atoms via rotation of light polarization

In this section I will describe the part of the apparatus we use for measuring the angular momentum of the atomic ensemble via the polarization of the light interacting with it, as described theoretically in chapter 3. We can divide the path of the probing

light in three big parts: the preparation, the interaction, and the analysis stage.

5.2.1. The preparation stage: linear and nonlinear probe. In the preparation stage we set all the light properties relevant for the experiment, e.g. detuning or timing. Of course polarization is also a critical feature, but I will comment more on its preparation in the following stage, the interaction one.

We have two different operational regimes for the probe light:

- Long (μs timescale) pulses, far detuned ($\approx$ GHz). We refer to this as the *linear* probing regime. For such linearity, typically the signals from several pulses in a train are combined.
- Short ($\approx$ 50 ns) pulses, higher peak intensity, hyperfine-splitting range detuning ($\approx$ 400 MHz). We refer to this as the *nonlinear* probing regime.

We create the probing pulses with acousto-optic modulators (AOM). In Fig. 5.2.1 the temporal dependence of the probing light power is plotted as measured by a calibrated reference detector.

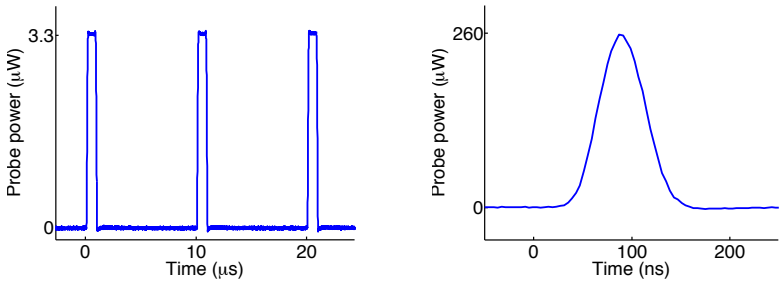

(a) Train of long pulses **(b)** Single short pulse

Figure 5.2.1. Different probing regimes. Left: Train of pulses for linear probing. Right: Short, intense pulse for nonlinear probing. Both curves are recorded by a calibrated reference detector and averaged 65 times.

The light frequency in the two probing regimes is set in two different ways: in the case of nonlinear pulses we want the specific detuning $\Delta_0 = +461.7$ MHz from the transition $1 \rightarrow 0'$. We use light from the same laser that we use for all the rest of processes resonant with the transitions from $F = 1$, e.g., the repumper light for the MOT, or the light for the initial atomic preparation via optical pumping. The laser (we refer to this physical laser as the "repumper" laser) itself is locked via FM saturated absorbed spectroscopy to the crossover between transitons $1 \rightarrow 1'$ and $1 \rightarrow 2'$, meaning that its frequency is already 72.2+156.9/2=151 MHz. The missing 311 MHz can be easy achieved with an AOM in double-pass configuration [Donley et al., 2005]. In a following section we will explain the strategy we used for fine tuning the frequency and getting exactly the specific condition of a null linear susceptibility. The electronics driving the AOM is stable enough that the only residual frequency instability comes from the laser source linewidth, which is around 200 kHz.

In the case of the linear probe, the desired detuning is too large for an AOM to function as an efficient frequency shifter. We thus use the technique of frequency offset locking between the repumper laser, which will be our reference laser, and an independent external-cavity diode laser, which we will finally use as the source of the far-off-resonant probing light.

A small amount of light from the probe laser is made to beat against a portion of light from the reference laser, by sending the two beams into the same single-mode fiber. The fiber output is monitored with a fast detector, whose signal is used instead of the voltage-controlled oscillator (VCO) in a phase-locked loop (PLL) circuit. We use the output of the PLL to feed back the piezo voltage and current of the probe laser and keep the frequency stabilized at an offset from the reference laser. The PLL can be programmed very easily via computer and the frequency lock established with an offset ranging from 300 MHz to 3 GHz. We can change between blue or red detuning, simply changing the polarity of the control loop.

Unfortunately the linewidth of the offset-lock laser is bigger than that of the reference laser. Ideally, similar offset-lock techniques can achieve a perfect phase-lock between the two lasers [Appel et al., 2009], which is a crucial requirement for Raman or EIT like experiments. Anyway, in our experiment the large detuning from resonance makes enough just simple frequency lock, with drifts in the beating frequency of few MHz.

5.2.2. The interaction stage. Now that we have well prepared in time and frequency the probe light, we have physically to deliver it to the atoms and make the two systems interacting. All the laser lights for the experiment, including the probing light, arrive close to the atom trap trough polarization maintaining fibers: this is basically for improving alignment stability. We clean the polarization at the fiber output using good polarizers (extinction ratio $\sim 10^{-5}$), so polarization maintaining fibers are also needed to minimize power fluctuations.

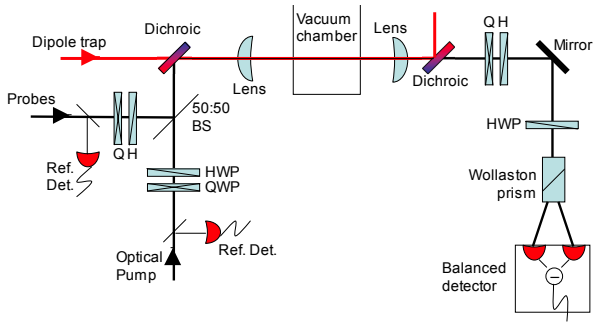

Figure 5.2.2. Schematic of the optics at the interface with the atoms.

We want to send the probing light along the longitudinal direction of the sample. Usually, for experiments in our lab we define a reference frame, and as a consequence a quantization axis, with respect to the dipole trap longitudinal direction; we call this the $z-$axis. The $x-$axis is in the vertical direction and the y is in the horizontal one transversal to the dipole trap.

The overlap of the 780 nm probe beam with the 1030 nm, powerful, laser beam that traps the atoms, is realized on a

dichroic surface. Downward in the path, the two co-propagating beams are gently focused into the vacuum chamber at the center of the 3D MOT with the same achromat, 8 mm lens. With this lens we generate the dipole trapping potential and as a consequence, the focus of the probe beam appears located in the same plane as the trap potential minimum. The diameter of the probe beam is chosen to have the focused waist of about 20 μm, matching in this way the transverse size of the atomic cloud.

After the chamber a second achromat lens, making a 1:1 telescope with the previous one, collimates again the two beams. A pair of dichroic beamsplitters are placed later on to divert the trapping light away from the detection. The polarization dependent transmission of all these optical elements must be taken into account when calculating any polarization rotation, and if possible any birefringence must be compensated.

Three sets of Helmholtz coils surround the location of the atoms to apply designed magnetic fields.

After the fiber delivering the light we have a set of zero-order wave-plates for pre-compensating the changes until reaching the atoms: using polarizer filters placed as close as possible to the glass cell containing the atoms, we can set the polarization of the probe to be linear with an extinction ratio of one part in 10^4. Towards the detection we have again wave-plates to compensate the birefringence especially of the pair of dichroics, which divert the trapping light.

We can perform such a polarization correction only without the presence of the powerful trapping beam, because the need of using the high quality filters made with plastic. Anyway, in an external setup we observed not important polarization change due to heat deposited by the trapping beam on the involved optics, in particular on the dichroic surfaces. The only thermal effect noticed was a loss in the degree of polarization of the pulse, meaning the same of having few percents of a randomly polarized photons.

5.2.3. The analysis stage. We want to measure changes in the polarization of the light. Just before reaching the atoms

we can assume that the Stokes vector has basically one component which is macroscopically populated:

$$\langle S_x \rangle = N_P/2, \quad \langle S_y \rangle = \langle S_z \rangle = 0 \tag{5.2.1}$$

$$\mathrm{var}\,(S_x) = 0, \quad \mathrm{var}\,(S_y) = \mathrm{var}\,(S_z) = N_P/4, \tag{5.2.2}$$

where the total number of photons in the pulse, N_P, is measured via splitting a portion of light just after the fiber and using a photo-detector (Thorlabs PDA10A) calibrated against a power-meter.

After the cell, the dichroic beamsplitters and the optics for pre-compensating the polarization, the probe light meets a half-waveplate at 22.5 degrees with respect to the vertical direction, and a Wollaston prisms to measure the two orthogonal diagonal polarizations. The intensity difference between the two beams exiting the Wollaston is indeed related to the Stokes component S_y. For each pulse, the resulting energy difference in the two beams is measured with two photodiodes (Hamamatsu S3883) in a balanced configuration. The subtracted photocurrent is then integrated with a charge-sensitive amplifier (Cremat CR-110), and pulse-shaper (Cremat CR-200) as final stage gives at the output a clean signal in volts reproducing the time evolution of the imbalance in photon-flux on the two diodes.

We save the signal from the balanced photo-detector with a real time oscilloscope (LeCroy WaveRunner X64), together with the signal coming from the reference detector located before the trap for the information about the incoming photon number, N_P.

5.3. Measuring the sample OD

As a normal operation, we check the coupling of light to the atomic ensemble. We quantify the strength of the coupling by measuring how much a fully magnetized sample rotates the polarization of probe light at a particular detuning. A strong reduction of this value from the typical one indicates that alignment, imaging or state preparation have problems and need to be optimized again. We will describe now this measurement because it is useful for having a global view on the probing mechanism.

After having collected atoms into the dipole trap, we set them all in the magnetic sublevel $|1,+1\rangle$ by means of optical pumping with $1 \to 1'$ circular polarized light along the trap axis ($z-$axis, the chosen quantization axis).

During the pumping and the following probing phase a magnetic field of about 100 mG along the $z-$axis is kept on. We can assume that the sample becomes fully magnetized, $\langle F_z \rangle = N_A$. At the end of the chapter we will discuss more details about the optical pumping and its efficiency.

We stabilize in frequency the probing light with the offset lock and generate pulses of $1\,\mu$s with an AOM in a train with $10\,\mu$s of separation between two subsequent pulses. The resulting detuning (locking+AOM) in this measurement normally ranges from -600 MHz to -1500 MHz from the transition $1 \to 0'$.

After having interacted with the magnetized sample, the pulses arrive at the polarimeter with the polarization rotated. We extract the information about the polarization rotation from a collection of 100 pulses (1 ms long train). In terms of the Stokes components, i.e., on the Poincaré sphere, the rotation angle is calculated for each pulse by

$$\phi^{(i)} = \frac{\langle S_y \rangle^{(i)}}{\langle S_x \rangle^{(i)}} = 2\frac{\langle S_y \rangle^{(i)}}{{N_P}^{(i)}}. \tag{5.3.1}$$

The principal effect going on in the off-resonant probing is the linear, paramagnetic Faraday rotation from the QND interaction,

$$\phi = 2\gamma t_0 \hbar^{-1} \alpha^{(1)} \frac{F_z}{2} = \frac{\omega Z_0 t_0}{A_{\text{eff}} T} \alpha^{(1)} \frac{F_z}{2} = G_1 \frac{F_z}{2}. \tag{5.3.2}$$

The coefficient G_1, also referred to as coupling constant, depends on the detuning as well as on all the interaction geometry issues, which are reassumed in the effective area, A_{eff}. By using the analytic expression of $\alpha^{(1)}$ as from eq. 3.5.8, the relation between the transition dipole matrix element, $D_{JJ'}$, and the decay rate Γ for $^{87}\text{RbD}_2$ transition (see eq. (38) in Steck [Steck, 2009] and references therein), and finally assuming $t_0 \equiv T$, we can

write explicitly the coefficient,

$$G_1(\Delta, A_{\text{eff}}) = \frac{\Gamma\lambda^2}{16\pi A_{\text{eff}}}\left(-\frac{4}{\delta_0(\Delta)} - \frac{5}{\delta_1(\Delta)} + \frac{5}{\delta_2(\Delta)}\right), \tag{5.3.3}$$

where $\delta_{f'} = \Delta - \Delta_{0f'}$ are the detuning from each involved excited state.

At the end of each measurement we take an absorption image of the trap to count the total number of atoms, N_A. To do this, we first switch off the dipole trap, then we illuminate from the side the cloud with light on resonance with the transition $2 \to 3'$, together with repump light $1 \to 2'$ from the MOT beams. We collect the shadow image on a CCD camera (Basler Scout-f) for $300\,\mu$s.

After 70 ms, the time needed by the camera to read-out the CCD sensor, we collect the reference image, with the same illumination conditions as in the shadow image. We also take a dark image to account for and subtract ambient/background light. For the same number of atoms we repeat the experiment for collecting statistics.

We repeat the whole procedure on different number of atoms in the trap. To achieve this we do not change anything in the loading phase, but instead we switch off the dipole trap few hundreds of microseconds to release some atoms ($\approx 15\%$) before the next pumping and the following probing phases. We fit with a linear function the rotation vs. the number of atoms and from the slope we get the coupling constant G_1 with its uncertainty.

For example at detuning $\Delta = -600$ MHz we measure $G_1 = 1.54 \times 10^{-7}$. For a figure of merit of the coupling, we better want a detuning independent quantity, which only accounts for the geometry of the interaction for example. We can extract the effective interaction area A_{eff} from the detuning dependence of G_1.

Comparing A_{eff} with the theoretical on-resonance scattering cross-section ($\sigma_0 = \lambda^2/\pi \approx 1.94 \times 10^{-13}$ m^2), calculated at the maximum atom number ($N_A = 8.5 \times 10^5$) we are able to trap, we deduce an optical depth, d_0, of the order of 40, by using the

following expression

$$d_0 = \frac{\sigma_0}{A_{\text{eff}}} N_A. \tag{5.3.4}$$

5.4. Looking for the magic detuning

We present now another measurement, which we performed using the linear, parametric Faraday rotation. In fact, the goal of this measurement was to minimize the effects of the linear susceptibility, and in this way achieve the condition of detuning desired for the nonlinear probing regime.

As already mentioned we generate the nonlinear probe pulses with an AOM, and we proceeded to an empirical search of the magic detuning, monitoring the paramagnetic Faraday rotation from a polarized sample as we were changing the RF frequency applied to the AOM.

We temporarily extended the probe pulse duration to have similar illumination condition as for the far-off-resonant, linear probe. We pumped the atomic sample, as normal, maximizing the value of $\langle F_z \rangle$ to the total number of atoms, N_A.

In this condition, by tuning the AOM frequency, we scanned the probe frequency and observed the coefficient G_1 across the analytically predicted magic detuning at 461.7 MHz, looking for the point where the rotation changed sign. In the experiment the crossing point was found at 468.5 MHz, instead. We explain the origin of this mismatch with a combination of the energy shift that the dipole-trap light induces on the ground state and the Zeeman shift from the guiding field.

We have not saved data of when we performed this measurement. For this reason we repeated in a second moment the search of the magic detuning, with the difference that we took the new dataset with the laser normally in use for the far-off-resonant, linear probe. As explained before, it is locked with the frequency offset lock, whose precision is worse that the one achieved by simply a spectroscopy locked laser shifted with an AOM.

In Fig. 5.4.1 we show the results. Each point is a measured G_1 for the specific detuning coming from a linear regression of the variable S_y measured on the balanced detector vs. the total

number of atoms in the trap, measured with quantitative absorption imaging. The error bars come from the uncertainty in the fit.

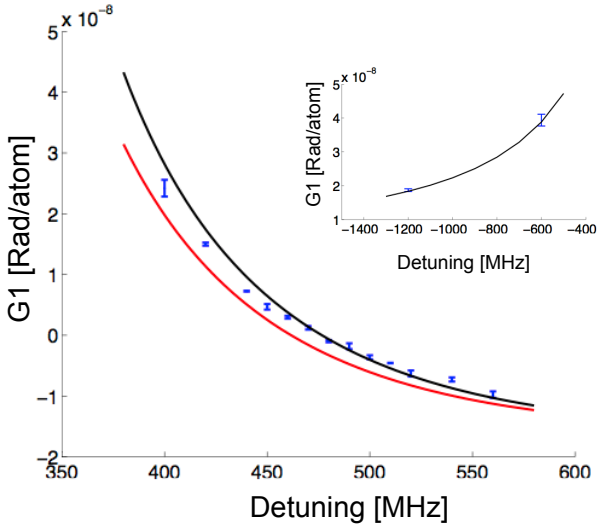

Figure 5.4.1. Spectrum of the linear susceptibility. Across the magic detuning the sign of the measured linear susceptibility changes sign. The black line is a fit to the data keeping a shift in the detuning as a free parameter. The red line is the analytic expression without detuning correction and scaled with the value at large red detuning (inset). Error bars come from the uncertainty in the fit.

The results are compared with the theoretical dependance of G_1 on the detuning, and with the absolute value calculated using a similar measurement but at far off resonant detuning of -1.2 GHz and -0.6 GHz, as shown in the inset of Fig. 5.4.1.

There is a difference of 13 MHz between the theory to the data, the difference between the red and black curve in Fig. 5.4.1. We explain the mismatch as a combination of the light shift induced by the trap and the error in the precision of the offset-lock.

5.5. Shot-noise-limited detection

The photodetector, which measures the light polarization rotations after the interaction with the atoms, is critical for the overall sensitivity of the spin detection. We typically need to know two of its characteristics, which summarize its performance in revealing quantum properties of light: the photon-to-electron conversion gain and the electronic noise floor.

We already mentioned that the detector is designed to work with pulsed light, and usually it works in a balanced configuration: the response of two photodiodes is subtracted and then converted into a readable electric signal. For calibrating the conversion gain, we analyze the response of the two photodiodes separately, instead.

We integrate in time each of the electric pulses resulting from a train of photon pulses in front of one of the two diode, for example the one which gives output signals with positive voltage. For background DC subtraction, we also integrate the signal corresponding to periods without light pulses in an equal time bin. The results after being averaged over several pulses are correlated with the input photon number per pulse, measured with a power meter and corrected knowing the duty cycle of the train of pulses. We repeat the same procedure for the diode giving negative outputs. We take the average of the two separate measurements as the overall conversion gain for the balanced configuration. We say that for each pulse of light entering in the polarimeter the photodetector reads out photon imbalance between the two diodes with a typical gain of 1.78×10^{11} Photons/(V·s), a value which for light at 780 nm is equivalent to a responsivity of 22.1 V/μW.

We also typically measure a difference of 2.3% between the gains of the two diodes. For an ideal balanced photodetection, we would like to have exactly the same value. This difference could be a problem for the nonlinear metrology experiment, because it makes the electric signal from the detector not only proportional to photon imbalance, i.e., polarization rotation, but also to the total flux of photons. In the next chapter we will show how in the experiment we excluded any possible fictitious nonlinearity coming from the instrumentation.

For calibrating the noise property we use a different method. We use the fact that we can produce pulses of light in a shot-noise-limited polarization state. We use this resource as a reference. We send pulses with energy ranging from 10^4 photons to 10^8, and we measure the variance in the imbalanced photons on the polarimeter, var (S_y). From the theory of quantum noise we expect $4\text{var}\,(S_y) = N_P$. On a log-log chart we can clearly distinguish the region where the detector is dominated by electronic noise, from where the detector is well behaving and the increasing variance is due simply to the shot-noise of the incoming light.

By calculating the proportionality factor in the region where the electric signal variance is linear with the photon number we have an alternative method to calculate the conversion gain, which finally results consistent with the previous value. By extrapolating the variance data at very low photon number, we can measure the photon equivalent electronic noise floor. We noticed that this value depends on the pulse length. In Fig. 5.5.1 we present the variance analysis for the case of a 50 ns long pulse, for which we can say that the detector is shot-noise limited starting from 4×10^5 photons.

In previous test [Koschorreck, 2011], the performance of the detector was checked with different light pulse-widths, starting from 250 ns. For the case of 1 μs long pulses, corresponding to the condition of the linear probe, the detector starts to be shot-noise limited from 3×10^5. Technical noise in the light or in the detector has a quadratic dependence on N_P, or equivalently a slope 2 in the log-log plot: In the region of N_P under investigation, we do not detect any evidence of technical noise.

5.6. Optical pumping for atomic-state initialization

In this last section of the chapter we want to explain some more concepts about the optical pumping process.

For setting the atoms in a desired initial state, we send laser light resonant with a particular transition through the cloud of atoms: the direction of propagation and the polarization of the light define which states of the hyperfine-split ground and excited states are connected by a transition and which are not.

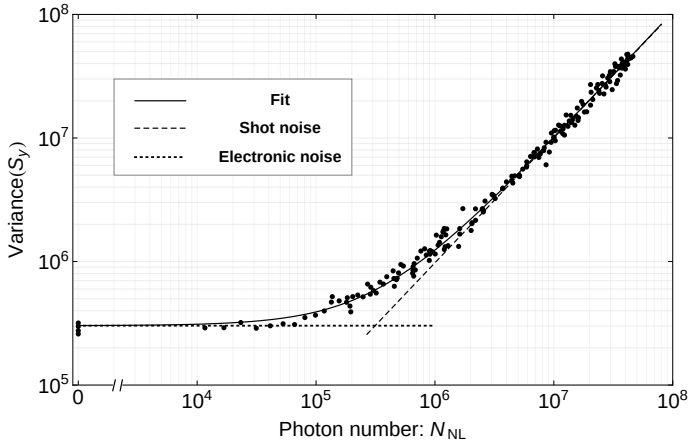

Figure 5.5.1. Noise performance of the photodetector. The data show a transition between dominant electronic noise and dominant shot-noise.

In such a way, atoms in some particular states of the ground level do not scatter photons, and are thus *dark* for that particular light. Atoms that decay because of spontaneous emission into such states, accumulate there since not anymore capable of being excited.

We mainly perform optical pumping on the $1 \rightarrow 1'$ transition in the D_2 line. We can send such light along the $z-$, quantization axis with circular left polarization, obtaining in such way σ_+ transitions. In this way we can initialize the cloud in a state having macroscopic magnetization $\langle F_z \rangle = N_A$.

We can also send pumping light along the $y-$axis, i.e., transversely with respect to the trap, with linear polarization, specifically vertical, orthogonal to the quantization axis which results in a coherent superpositions of sigmas transitions. This other optical pump initializes the atoms in a macroscopic J_x state.

Ideally, the pumping is a cumulative process and giving a certain time, which depends on the light intensity, all the atoms are sent into the particular dark state. Unfortunately, during the pumping process, atoms can decay into the undesired ground

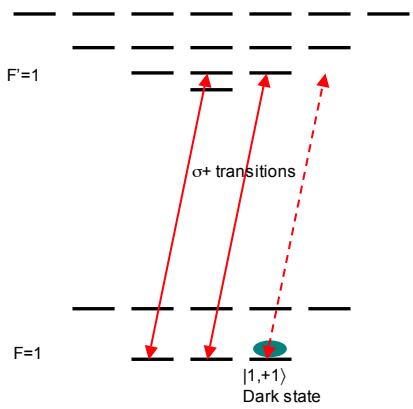

Figure 5.6.1. Resonant circular-polarized light for optical pumping. Frequency and polarization of the pumping light set the dark state.

state level with different energy, because the spontaneous emission does not distinguish between the two 6.8 GHz separated manifold. For this reason, efficient optical pumping needs to be supported by an auxiliary light resonant with the undesired ground state to recycle the atoms accumulating there: we call this auxiliary light "optical repump". It is tuned on the transition $2 \rightarrow 2'$ and reaches the atoms from the 6 directions of the MOT beams.

For pumping into F_z macroscopic state we typically use 30 nW of resonant light switched ON for approximately 30 μs, corresponding to 3.6 millions of photons. We also send optical repumping light for a total intensity at the center of the trap of about 100 W/m^2, counting 6 mm for the MOT beam waist.

The pumping beam, although being aligned with the focusing telescope on top of the dipole trap beam, has a focus spot wider (100 μm waist) than the cloud dimensions. This is for having a better uniform distribution of the pumping light over the size of the cloud.

In the lab, we empirically see that such settings maximize the response of the cloud, e.g., the far-off resonant paramagnetic Faraday rotation. Anyway we performed some simulations

for better supporting considerations about optical pumping efficiency and uniformity over the cloud.

5.6.1. Simulation for optical pumping. We use techniques presented in Chapter 4 to simulate the optical pumping dynamics of a single atom illuminated by laser light with defined frequency, polarization and intensity. In addition, we can account for the case of having two lasers at different frequencies, for example one tuned close to the transitions from the ground level $F = 1$ and the other laser, 6.8 GHz away, tuned close to the transitions from $F = 2$. This can be achieved performing two successive RWAs on the dipole Hamiltonian, with the only restriction that the dynamics of interest must be much slower that the inverse of the frequency separation between the two lasers.

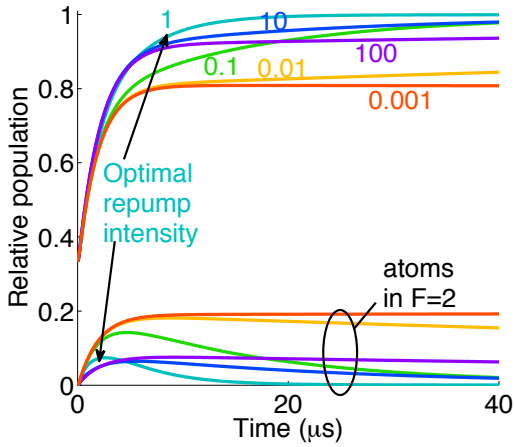

Figure 5.6.2. Pumping dynamics as a function of optical repump intensity. We plot the population of the dark state as well as the population in the $F = 2$ level for different intensity of the optical repump. There is an optimal value for the optical repump intensity.

We can simulate for example the dynamics of the optical pumping process with circular plus polarized light starting from an initial mixed state of the three magnetic sublevels in $F = 1$. The pumping light is chosen to be resonant with the $1 \to 1'$. In

this way the level with $F = 1$ and $m_F = 1$ is a dark state. We include also optical repumping light resonant with the $2 \to 2'$ transitions. In the simulation, we define the polarization of the repumping light to be an equal superposition of σ plus/minus and π polarization: this is an approximation of the experimental situation where the light is coming from the 6 direction of the MOT beams.

We set the intensity of the pumping light similarly to typical experimental conditions. In fig. 5.6.2 we show the results of such simulations. The population of the dark state starts from $1/3$ and grows towards unity. At the same time also the probability of populating $F = 2$ increases. We found that 8 W/m^2 of repump light is the optimal intensity for maximizing the pumping efficiency into the dark state. The simulations for higher or lower intensity of repumper show still enough probability of accumulating atoms into $F = 2$.

For the optimal repumping intensity the dynamics mimics a trend with a combination of two exponential decays, as shown in Fig 5.6.3 . For example the population of the bright state, $P^{(b)}(t)$, can be approximated with the following analytical expression

$$P^{(b)}(t) = \left(\frac{2}{3} - K_0\right) e^{-\frac{t}{\tau_1}} + K_0 e^{-\frac{t}{\tau_2}} \tag{5.6.1}$$

with $K = 0.13$, $\tau_1 = 1.8\,\mu$s, $\tau_2 = 5\,\mu$s. As shown in Fig. 5.6.3, lowering the pumping intensity, I_{pump}, the consequences are an overall slower dynamics:

I_{pump}	τ_1
I_0	$1.8\,\mu$s
$I_0/2$	$4\,\mu$s
$I_0/5$	$12\,\mu$s
$I_0/10$	$24\,\mu$s

while the optical repump mechanisms works better, as made evident by the less number of atoms accumulating at any moment in $F = 2$ and by the fact that the second exponential decay is not appreciable at all.

5.6.2. Pumping an optically thick sample. As mentioned before, for pumping the sample into a macroscopically F_z

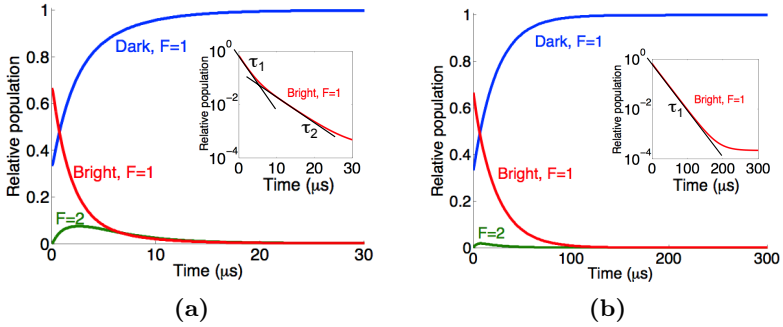

Figure 5.6.3. Competitive effects of optical pumping and repumping light on the population in $F = 2$. Evolution of the population for the dark state, the two bright states, and the whole set of $F = 2$ states. In the insets, semi-log plots to show decaying time-scale of the bright state population. (A): the case of $I_{\text{pump}} = I_0 = 1.9$ W/m^2 with $\tau_1 = 1.8$ μs and $\tau_3 = 5$ μs. (B): the case $I_{\text{pump}} = I_0/10$ with only appreciable $\tau_1 = 24$ μs.

polarized state we send circular polarized resonant light along the quantization axis, the direction that corresponds to the longitudinal size and the high optical depth of the cloud. This means that the light is strongly absorbed by the initial part of the cloud, which shadows the following atoms until enough atoms populate the dark, transparent state.

The pumping process in the dipole trap happens thus slower than in the single-atom simulations. Trying to model and quantify what happens, we simulated the sample split in several slices. The first slice is illuminated with the total, constant intensity of the pumping light, $I_1(t) = I_0$, one of the free parameter in the model. The population of the slice evolves toward the dark, transparent state. As a consequence the transmission of the light towards the next slice also increases, and so on the process is iterated. We note that the results converge quite quickly with the number of slices, so we finally work with 100 slices.

A second free parameter in this toy-model is the total optical depth of the sample, d_0. We consider an optical depth for each

slice, $d_i(t)$, as a fraction of the total optical depth and moreover depending on the corresponding population of the bright states, $P_i^{(b)}(t)$. Knowing $d_i(t)$ we can easy calculate the intensity illumination on the next slice, $I_{i+1}(t)$.

$$d_i(t) = \frac{d_0}{N} P_i^{(b)}(t) \tag{5.6.2}$$

$$I_{i+1}(t) = I_i(t)\exp(-d_i(t)) \tag{5.6.3}$$

To save calculation resources, instead of solving for each iteration the master equation with the time-dependent pumping light intensity, we use the analytic expression of 5.6.1, adapting the parameters in function of the time-dependent intensity,

$$\tau_i(t) = \tau_1 \frac{I_0}{I_i(t)} \tag{5.6.4}$$

$$K_i(t) = K_0 \frac{I_i(t)}{I(0)} \tag{5.6.5}$$

$$P_i^{(b)}(t) = \left(\frac{2}{3} - K_i(t)\right) e^{-\int_0^t \frac{d\zeta}{\tau_i(\zeta)}} + K_i(t) e^{\frac{t}{\tau_2}} \tag{5.6.6}$$

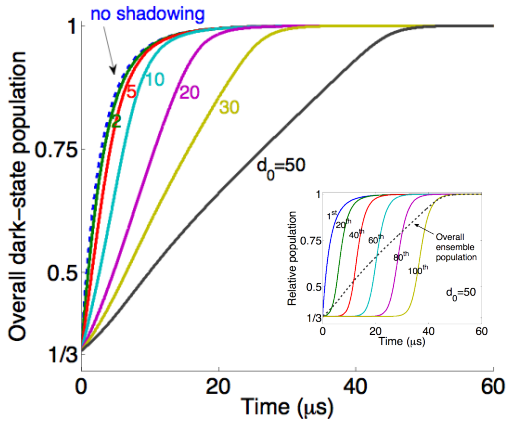

Figure 5.6.4. The shadowing effect. The dynamics of the population for the whole ensemble is simulated with different total optical depths, d_0= 2, 5, 10, 20, 30 and 50. In the inset, for the case of d_0=50, the dynamics of every 20 successive slices.

As shown in Fig. 5.6.4, the speed of the process is expected to be inversely proportional to the total optical depth. We see that the effects of shadowing are simply compensated by a slightly longer pump pulse, which is not a big problem for the range of optical depth, between 30 and 50, of our cloud.

CHAPTER 6

Testing the nonlinear probe in an experiment

With the experimental requirements satisfied and a solid theoretical framework to interpret correctly the results, we performed an experiment to directly use the nonlinear interaction established by atoms between probing photons for sensing an atomic quantity, and show that the sensitivity scales better than the Heisenberg limit when we increase the number of probing photons.

In this chapter we will describe the details of the experiment. First we will explain how the hard core of the experiment consists in a calibration procedure of the nonlinear probe making use of the linear one. Then, we will show how we fitted the numerical model presented in Chapter 4 to the experimental results. We will explain also how we excluded possible other sources of nonlinearity, which could have mimicked a better sensitivity scaling. Finally, we will analyze the possibility of judging the utility of the new nonlinear technique in terms of absolute sensitivity, as well as comment about comparing different probing techniques.

6.1. Calibration by sensing the same quantity

Our goal is to use a new metrological technique for measuring via paramagnetic Faraday rotation the quantity F_z of the atomic sample. By using the correct magic detuning, we expect that the polarization rotation of the nonlinear probe, ϕ_{NL}, will be proportional to the total number of photons in the nonlinear probing pulse, N_{NL}, and of course reproduce the quantity $\langle F_z \rangle$,

$$\phi_{\mathrm{NL}} = B\langle F_z \rangle \frac{N_{\mathrm{NL}}}{2}, \tag{6.1.1}$$

In chapter 4 we discussed several factors which are expected to determine B. Apart from the detuning, there is the geometry as well the temporal dynamics, both aspects that we know how to include via the numerical model. Here we explain how we tested that model and independently determined B. This we do by comparing to a trusted measurement, very much in the same way as we calibrate a new instrument by comparison to a older one.

As we stressed several times, a key point of our apparatus is that we can achieve very simply different regimes of probing. We know that the linear probing is a very well established technique for returning the value $\langle F_z \rangle$. In previous work we have demonstrated that the linear probe is sensitive enough to distinguish quantum fluctuation in the atomic angular momentum variables [Koschorreck et al., 2010b]. Moreover it provides a quantum non demolition measurement of F_z, i.e., after a linear probe, the quantity is ready to be measured once again, unmodified.

Consequently, we can imagine to interrogate successively the same atomic sample with the linear and the nonlinear probes. We thus get a linear Faraday rotation, ϕ_{L}, and use it as indicating the true value of $\langle F_z \rangle$ in correlation with the correspondent ϕ_{NL}, which we want to calibrate.

The experiment has the following sequence:

#1 Trap loading. We use 2 seconds to collect up to 7.5×10^5 atoms into the dipole trap.

#2 Optical pumping. We switch ON a guiding magnetic field along z and send circular polarized light, resonant to $1 \rightarrow 1'$ supported by optical repump light, for setting $\langle F_z \rangle = N_A$.

#3 Linear probing. F_z is precisely measured during 400 μs. We send a train of 1 μs pulses separated by 10 μs, each containing 3×10^6 photons at the detuning $\Delta_{\mathrm{L}} = +1.5$ GHz. The signals are summed and can be considered a single, modulated pulse. We get the rotation $\phi_{\mathrm{L}} = A\langle F_z \rangle/2$. The quantity A is independently

calibrated in a previous moment using quantitative absorption imaging. We have $A(\Delta_{\mathrm{L}}) = 3.3(1) \times 10^{-8}$ rad per atom.

#4 Nonlinear probing. A single, short and intense pulse containing N_{NL} photons, with the shape and the detuning as described in chapter 5 from which we get the rotation ϕ_{NL}.

#5 A second linear probing. We want to know the level of damage, to the atomic magnetization due to the intense nonlinear probe. We thus repeat a linear interrogation from which we get the rotation $\phi_{\mathrm{L}'}$, having $\overline{\eta} \equiv 1 - \phi_{\mathrm{L}'}/\phi_{\mathrm{L}}$, which is a reasonable experimental way to estimate the damage connected to the loss of fidelity between final and initial state.

#6 Thermalization. Any residual magnetization of the sample is cancelled by a thermalization procedure, shuffling the atoms with resonant light back and forth between $F = 1$ and $F = 2$, in a condition of no guiding field. This procedure also causes few atoms to escape from the trap.

#7 Ranging N_A. The sequence is repeated 20 times from step #2, allowing to collect calibration data in a range of varying number of atoms after each loading of the trap, because of the losses in step #6.

We want to show nonlinear behavior as a function of the total photon number in the nonlinear probe pulse and for this reason in the step #4 we change the value of N_{NL} in the range 10^5 to 10^8. In the same conditions, the whole experiment is repeated 100 times for gathering statistics.

Both the responses from the linear and the nonlinear probe are expected to be proportional to the number of atoms. We group the data according to the photons used in the nonlinear probe pulse, N_{NL}, and for each value we plot the results of the linear vs. the nonlinear probe in a kind of correlation plot. In Fig. 6.1.2 we show these correlation plots for some values of N_{NL}.

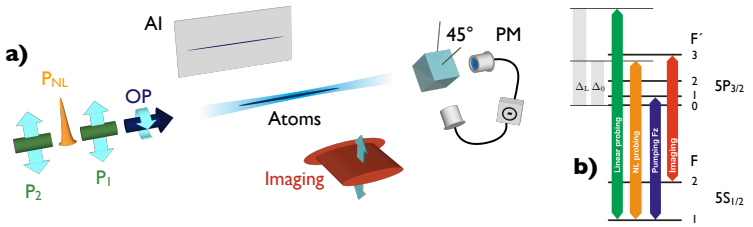

Figure 6.1.1. Schematic of the experiment. a) The light pulses interacting with the atoms: along the longitudinal trap axis and sequentially, the optical pumping, the first linear probe, the nonlinear probe and the second linear probe. Transversally the absorption imaging light. b) The detuning of all the light beams which interact with the atoms.

In each plot, we can identify three classes of data: The green points correspond to the data without atoms where both the linear and the nonlinear rotations are zero on average. Comparing the spreading of this dataset in the two measurement, one can extract information about the absolute level of noise and consequently of sensitivity. As we expect, the linear probe is more precise, and so it is a good reference for calibrating the unknown nonlinear probe.

The red points are data collected ranging the number of atoms from 1.5×10^5 to 3.5×10^5. In this range the proportionality of both estimation techniques with respect to the atoms is well established and these data are fitted to get the calibration factor at any specific value of N_{NL}. We can also estimate the underlying sample standard deviation, which we report in the plots as the grey region and we will consider later on for calculating the probe sensitivity.

The blue points are data corresponding to the largest number of trapped atoms. In these conditions, and in particular for the highest values of N_{NL}, the resulting rotation angles from the nonlinear probe are no longer proportional to the number of atoms. What is happening here is that the combination of large polarization rotation due to the many atoms, and high photon

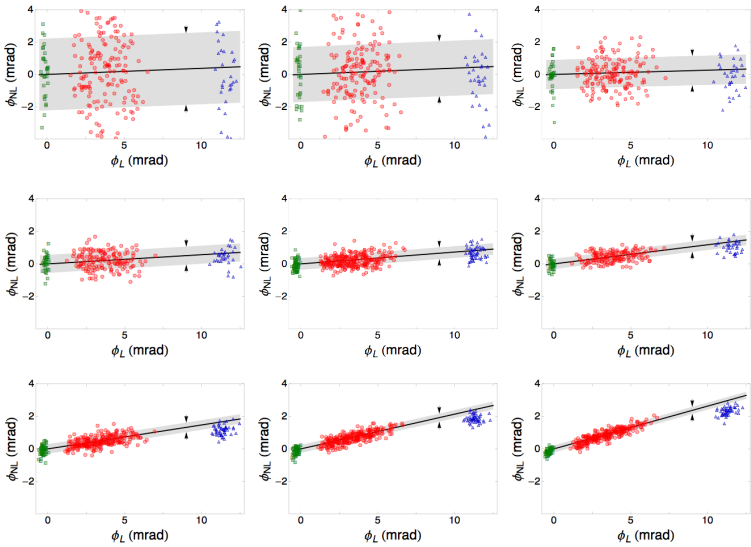

Figure 6.1.2. Calibration plots. $\phi_{\rm NL}$ vs. $\phi_{\rm L}$ for various $N_{\rm NL}$, respectively from top-left: 0.69, 0.94, 2.2, 5.0, 7.9, 11, 15, 27, 37 millions. Green points are for $N_A = 0$. Red points are for N_A between 1.5 and 3.5×10^5. Blue points are for $N_A = 7 \times 10^5$. The gray areas show one standard deviation in the residuals of the red points from their linear regression (black line).

number, causes a signal too strong on the balanced detector, which simply saturates. These data are excluded from the fit.

As mentioned, we fit the data in each correlation plot with a line and from the resulting slopes we get the desired calibration. In particular we analyze the dependence of these calibration factors on $N_{\rm NL}$.

We show such dependance in Fig. 6.1.3, where each point is the slope of the corresponding correlation plot. The error bars are the uncertainties in the fitted slopes. The observed dependance on $N_{\rm NL}$ is well fit by a simple model of the nonlinear response including saturation:

$$\frac{d\phi_{\rm NL}}{d\phi_{\rm L}} = \frac{B(\Delta_0)N_{\rm NL}}{A(\Delta_{\rm L})}\frac{1}{1+N_{\rm NL}/N_{\rm NL}^{(\rm sat)}}, \tag{6.1.2}$$

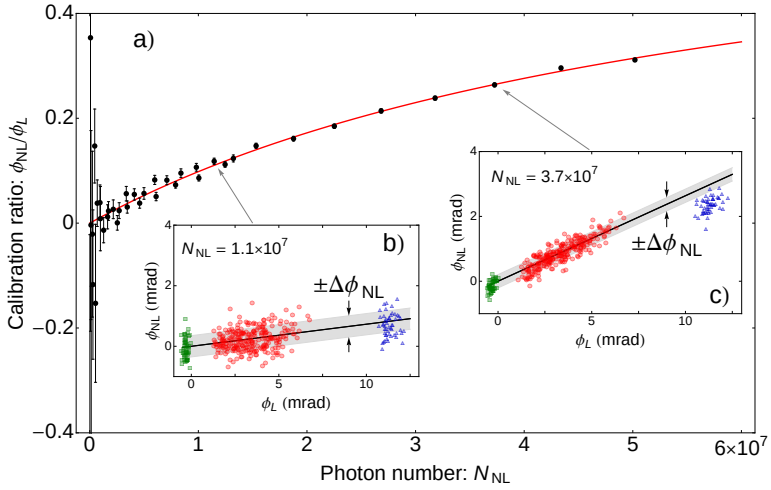

Figure 6.1.3. Calibration summary. a) Results of the fit for each calibration plot: slopes and their uncertainty. The red line is the analytic expression of eq. 6.1.2. b)-c) Two particular calibration plots, resulting in the indicated points.

with a saturation parameter $N_{\mathrm{NL}}^{(\mathrm{sat})} = 6.0(8) \times 10^7$ and the nonlinear coupling strength $B(\Delta_0) = 3.8(2) \times 10^{-16}$ rad per atom per photon.

6.2. Calculating the sensitivity scaling

From the analysis on the calibration of the nonlinear probe we can extract information about its sensitivity and how this scales with N_{NL}. We can easily understand that there are two main ingredients which contribute to the scaling: first we clearly see how the standard deviation $\Delta\phi_{\mathrm{NL}}$, the grey region below the scattered red points in the calibration plots (see insets of Fig. 6.1.3), diminishes with the increasing N_{NL}. This is the expected square root law of the shot noise, with a small contribution from electronic noise of the detector, ΔE, which we measure independently as explained in chapter 5 and which we can subtract. We have:

$$\delta\phi_{\mathrm{NL}} = \sqrt{(\Delta\phi_{\mathrm{NL}})^2 - (\Delta E)^2} \sim (N_{\mathrm{NL}})^{-1/2}. \tag{6.2.1}$$

Second, the fact itself that the calibration vs. ϕ_{L}, i.e., the true value of $\langle F_z \rangle$, gets steeper with the increasing N_{NL}, means a boost in the sensitivity which is genuinely an effect from the nonlinearity:

(6.2.2)

$$\phi_{\mathrm{NL}}\left[N_{\mathrm{NL}}, \langle F_z \rangle\right] = \frac{d\phi_{\mathrm{NL}}}{d\phi_{\mathrm{L}}} A(\Delta_{\mathrm{L}}) \langle F_z \rangle = \frac{B(\Delta_0) N_{\mathrm{NL}}}{1 + N_{\mathrm{NL}}/N_{\mathrm{NL}}^{(\mathrm{sat})}} \langle F_z \rangle.$$

The sensitivity in the estimated variable is thus:

$$\delta F_z^{(\mathrm{NL})} = \langle F_z \rangle \frac{\delta\phi_{\mathrm{NL}}}{\phi_{\mathrm{NL}}} \sim \frac{1}{N_{\mathrm{NL}}^{3/2}} \frac{1 + N_{\mathrm{NL}}/N_{\mathrm{NL}}^{(\mathrm{sat})}}{B(\Delta_0)} \tag{6.2.3}$$

In Fig. 6.2.1 we report the fractional sensitivity $\delta F_z^{(\mathrm{NL})}/\langle F_z \rangle$ for each value of N_{NL} in the experiment. We assume the whole polarized ensemble, $\langle F_z \rangle = 7 \times 10^5$. For each point the error, propagated from the errors in the calibration plots, is not visible because it is smaller than the marker.

On the log-log plot we appreciate a scaling of $-3/2$ to within experimental uncertainties in the range $N_{\mathrm{NL}} = 10^6$ to $N_{\mathrm{NL}} = 10^7$, and super-Heisenberg scaling, i.e., steeper than -1, over two orders of magnitude $N_{\mathrm{NL}} = 5 \times 10^5$ to $N_{\mathrm{NL}} = 5 \times 10^7$.

For photon numbers above $N_{\mathrm{NL}} \gtrsim 2 \times 10^7$, the saturation of the nonlinear response degrades the optimum scaling. This goes together with the behavior of the damage to the atomic magnetization, $\overline{\eta}$, measured making use of the third linear probe, and also shown in Fig. 6.2.1. We can clearly correlate substantial deviation from the optimum sensitivity scaling with damage above 10%.

Regarding the damage, the minimum non-zero damage found even for small N_{NL} is understandable as a combination of stray light and magnetic fields disturbing the atoms during the 20 ms period between the two linear measurements, time technically needed in the experiment to switch the position of a shutter.

6.3. Comparison to the theoretical model

Using the theoretical model of the nonlinear light-atom interaction, which we have presented in chapter 4, we can reproduce the experiment, in particular the scaling of the sensitivity

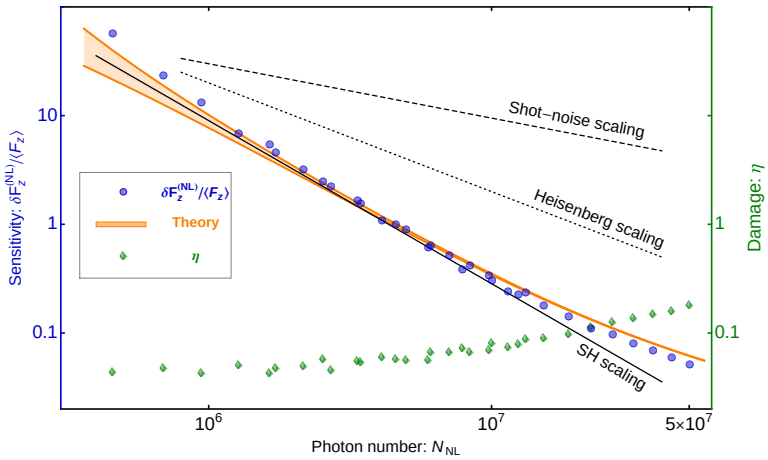

Figure 6.2.1. Sensitivity scaling. Blue points are the calculated fractional sensitivity. Their error bars, from the uncertainties in the calibration fits, are smaller than the marker and so are not visible. Orange curves are the model for detuning $\Delta_0 \pm 200$ kHz, and experimentally measured geometrical features of the interface. Green points are the damage from the comparison of the linear probes before and after the nonlinear pulse. We plot for visual comparison the power law corresponding to the shot-noise and Heisenberg scaling.

and how it correlates with the damage to the atomic state. The orange curves in Fig. 6.2.1 are fits of such theoretical model to the experimental point.

Let us recall the end of chapter 4, where we combined the results from homogeneous simulations with the spatial geometrical properties of the interface (see overlap integral in eq. 4.7.3). From that expression of the contribution of the whole cloud to $\langle S_y \rangle$, we can calculate the Faraday rotation and consequently the sensitivity:

$$\delta F_z^{(\mathrm{mod})} = \langle F_z \rangle \delta\phi_{\mathrm{NL}} \left(\frac{\int d^3x\, n(\mathbf{x})\, \Theta\left(N_{\mathrm{NL}}, M(\mathbf{x})\right)}{N_{\mathrm{NL}}} \right)^{-1}. \tag{6.3.1}$$

In particular we consider two runs of simulations of the single-atom dynamics, 200 kHz above and below the magic detuning, to account for the uncertainty in the probe laser detuning. Its effects are mostly evident at low photon number, where the nonlinear response is not dominant and any residual linear effect can play a role.

We use real parameters from the experiment, i.e., size of the cloud and waist of the probe mode, for calculating the overlap integral. These parameters are generally important in the correct location of the theoretical curve with respect to the photon number axis, and also in profiling the bending at high photon number. We only left as a free parameter the total number of atom, which basically means the position of the curve with respect to the vertical axis.

6.4. Excluding other sources of nonlinearity

In nonlinear experiments there is a risk that other undesired effects mimic the sought-after behavior. We put effort into checking that the signal we measured, and its dependence on the incoming number of photons, were indeed coming from the expected atomic dynamics.

Typical sources of such unwanted nonlinearities are passive optical elements in the path or photodetectors. Our experiment makes it easy to exclude such kind of systematic errors. As already explained, we noticed problems with a saturating photodetector in particular conditions of too many atoms under probing with high number of photons. We excluded those data from the analysis.

In addition, we performed an experiment with no atoms present at all. We mimic the Faraday rotation signal by using a wave-plate, in particular intentionally rotating the one in the normally balanced polarimeter. Everything else was exactly as in the experiment with atoms.

We choose the new angle of the wave-plate such that for the highest value of N_{NL} the signal on the detector was comparable to the case of the experimental data from the maximum atom number indeed used for the analysis, 3.5×10^5. As mentioned in the discussion about the blue points in the correlation plots, we

observed problems of electronic saturation when using instead the maximum achievable trapped atoms, 7×10^5.

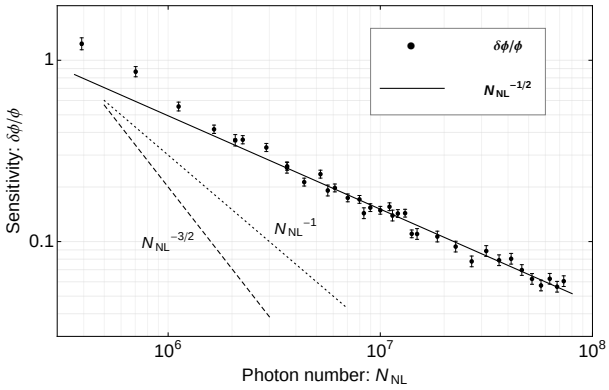

Figure 6.4.1. Verification of the apparatus linearity. Sensitivity results obtained as in Fig. 6.2.1, but with a waveplate in place of the atomic Faraday rotation. As expected the sensitivity shows SQL scaling, providing a direct verification of the linearity of the equipment and method of analysis. Error bars plotted are the standard errors of the measured rotation signal.

The resulting measured rotation without atoms shows no dependence on N_{NL}, and gives shot-noise scaling of the sensitivity, plotted in Fig. 6.4.1 over the same range of N_{NL} used in the experiment.

6.5. Sensitivity comparison, a scenario-dependent issue

Although the remarkable point of our research resides in having demonstrated the improved scaling of the sensitivity thanks to nonlinearities, it is understandable to ask a direct comparison in absolute terms of sensitivity between the two metrological approaches, the linear and the nonlinear, we use in our system.

The experimental results illustrate the subtle relationship between scaling and sensitivity in a nonlinear system. For an ideal nonlinear measurement, the improved scaling would guarantee better absolute sensitivity for sufficiently large number of probes.

Conversely, in a real system higher order dynamics, such as the optical pumping effects we experimented in our apparatus, are a strong limitation because they constrain to work below a certain level of probe particle number. So how can we judge the performances of a nonlinear metrological approach in an absolute way?

Quantum metrology problems are fundamentally resource-optimization problems: given a finite resource, e.g. N probes, how can we best use them to achieve measurement sensitivity. When comparing linear vs. nonlinear metrology, the measurement systems are necessarily different, and it is not obvious what is the relevant resource. In contrast, entanglement can be used or not used in one-and-the-same measurement system, making that comparison very simple.

Taking our experiment as an example, the linear and nonlinear probe necessarily have different detuning, leading to a difference in strength of interaction with the atoms, affecting both the desired effect of optical rotation, and undesired effects of scattering and decoherence of the atomic state. In this context, it is not clear what is the limited resource to consider, if the photon number or a level of damage of the atomic state or even something else.

In fact, nonlinear measurements may be possible in regimes that are inaccessible to linear measurement. In optics, a linear measurement implies a limited intensity and (for a given geometry) a limited flux of photons. Increasing N then means increasing the duration of the measurement. High-speed linear measurements, or linear measurements limited by some decoherence time, would have limited N and thus limited sensitivity. A nonlinear measurement would not be limited in the same way. In an atomic context, very similar considerations would concern atomic density and spatial resolution.

When we look at our experiment in a scenario when the time is a limiting factor, the relevant figure of merit is a "sensitivity-per-unit-time", $\delta F_z \tau^{1/2}$, and the measurement duration τ is $\tau_{\mathrm{L}} = 40\ \mu$s or $\tau_{\mathrm{NL}} = 54$ ns for the linear or nonlinear measurement, respectively. Combining this with the results reported above,

we find

$$\delta F_z^{(\mathrm{L})}\tau_{\mathrm{L}}^{1/2} = \langle F_z\rangle \frac{\delta\phi}{\phi_{\mathrm{L}}}\tau_{\mathrm{L}}^{1/2} = \frac{2}{A(\Delta_{\mathrm{L}})}\frac{N_{\mathrm{L}}^{-1/2}}{2}\tau_{\mathrm{L}}^{1/2} = \tag{6.5.1}$$
$$= 1.9\times 10^{5}\,\mathrm{Hz}^{-1/2} N_{\mathrm{L}}^{-1/2}$$

and

$$\delta F_z^{(\mathrm{NL})}\tau_{\mathrm{NL}}^{1/2} = \langle F_z\rangle \frac{\delta\phi}{\phi_{\mathrm{NL}}}\tau_{\mathrm{NL}}^{1/2} = \frac{2}{B(\Delta_0)N_{\mathrm{NL}}}\frac{N_{\mathrm{NL}}^{-1/2}}{2}\tau_{\mathrm{NL}}^{1/2} = \tag{6.5.2}$$
$$= 6.1\times 10^{11}\,\mathrm{Hz}^{-1/2} N_{\mathrm{NL}}^{-3/2}$$

Given an equal number of photons $N_{\mathrm{L}} = N_{\mathrm{NL}} = N$, the nonlinear technique surpasses the linear at $N = 3.2\times 10^{6}$, well within the super-Heisenberg portion of the curve in Fig. 6.2.1.

Conversely, in a scenario with only limitation to the number of probes, the relevant figure of merit is a "sensitivity-per-measurement". Already we can expect that in our experiment this will always be better in the linear measurement, because it is required for calibration of the nonlinear one. From the data in the calibration plots, we can see this fact looking at the green points, which are the measurements without atoms: the horizontal spread, i.e., the uncertainty in the linear measurement, is always smaller than the vertical spread.

Specifically, when time is not a limited resource, the sensitivity per measurement is $\delta F_z^{(\mathrm{L})} = 3\times 10^{7} N_{\mathrm{L}}^{-1/2}$, and $\delta F_z^{(\mathrm{NL})} = 2.6\times 10^{15} N_{\mathrm{NL}}^{-3/2}$. Extrapolating, the ideal crossover point of $\delta F_z = 3.2\times 10^{3}$ spins, where the nonlinear technique would surpass the linear at $N_{\mathrm{NL}} = 8.7\times 10^{7}$, is never actually reached, due to the higher-order nonlinearities.

Conclusions and perspectives

The work presented in this dissertation is a study, both theoretical and experimental, about a specific nonlinear dynamics in a polarization-based light-atom interface and its implications and uses for quantum metrology.

From a theoretical perspective, we focussed our attention on the perturbative approach for calculating effective interaction Hamiltonians starting from the collective operators of spin ensembles and pulses of polarized photons, interfaced one with the other. This gives analytic expressions for the fourth-order (in field strength) terms in the perturbation series, the first extension of the collective operators model [Geremia et al., 2006; Kupriyanov et al., 2005; Deutsch and Jessen, 2010] to nonlinear optical processes. In this way it is now possible to calculate for example the detuning dependance of phenomena such as saturation, fast-electronic nonlinearities or four-wave mixing.

The nonlinear terms we developed for describing such photon-photon interactions mediated by the atoms, are similar in form to nonlinear Hamiltonians proposed by Boixo and coworkers [Boixo et al., 2007, 2008a] as a possibly useful resource in quantum metrology. We adapted their argumentation for our system, in particular we looked at the role played by the quantum noise, concluding that also in our system, at least analytically, nonlinearity would lead to an improved scaling of the sensitivity with the number of probing photons.

Moreover we studied the nonlinear dynamics from a microscopic point of view, i.e., we simulated the single-atom dynamics under the effect of the probing light by numerically solving the system of Maxwell-Bloch equations. In this way we were able to

include in the analysis other effects, such as spontaneous emission and optical pumping, not accounted by the Hamiltonian. We also developed a method for calculating the macroscopic effects of a real interface, including geometrical issues and atom density or light intensity inhomogeneities, starting from the simulations for the single-atom.

Our apparatus in the lab has already demonstrated, in other experiments about spin squeezing [Koschorreck et al., 2010a; Sewell et al., 2012], the high quality of the interface between the light and the atomic system. We adapted it in order to be able to work with shorter and more intense probing pulses. We find the way to achieve detunings where to null linear contributions and perform pure nonlinear interrogations of the atomic variables. We were able to calibrate the nonlinear probing technique against the trusted linear one on the same physical quantity. We did experiments to exclude other possible sources of nonlinearities.

We found what theoretically predicted that the nonlinearities under our study were able to achieve a scaling of the sensitivity better than the scaling of the Heisenberg limit for one order of magnitude in the photon number, and better than the scaling of the shot-noise limit within two orders of magnitude. We also found that when the probing duration was taken into account, there are situations where the sensitivity-per-time of the nonlinear probe outperforms the linear one. On the other hand, the sensitivity-per-measurement of the nonlinear probe, as well as the overall advantage of having a better scaling, was limited by damaging processes on the atomic state, which were happening at photon number higher than 20 millions per pulse.

In our opinion there is still room for more investigation about the nonlinear behavior of polarization-based light-atom quantum interfaces. In the future, the same experimental apparatus could also be used to study other nonlinearities of the optical probing. For example dynamics driven by the tensorial terms in the Hamiltonian should also result in a nonlinear dependance of the probe response on the photon number, because of the the mutual action of the atom to the light and viceversa. This could

led to improved sensitivity scaling, in a similar way as described in this dissertation.

The analytic expression, which we have developed for the interaction, includes terms of self-rotation type. Future studies could be focussed on using these kind of effects. These terms are good candidates to be useful to measure selectively quantities related with the $m_F = 0$, magnetic-insensitive sublevel in the ground state, once the correct probing condition in terms of detuning will be found, together possibly with the right combination of alternating orthogonal polarizations and post-processing.

Moreover, with the idea of looking for better probe performances in a time-limited regime, it would be interesting to study even faster pulsed interactions, e.g., below the nanosecond scale.

Another remarkable thing to mention is that this research is part of a debate about the notion of Heisenberg limit, and in general about the existence and the meaning of a possible ultimate limit. During these years several theoretical groups somehow revised and more deeply considered these concepts.

There are those who think that the ambiguity about having a better scaling of the sensitivity with respect to the generally-considered-ultimate Heisenberg limit is solved if the resources used in the estimation are counted not as simply as the probe number [Zwierz et al., 2010, 2012]. There are also those who, making consideration about entropy, say that super-Heisenberg sensitivities can only work locally, with respect to the phase to estimate, while on the global range, i.e., for a previously unknown random phase, only Heisenberg limited sensitivity will remain possible [Hall et al., 2012; Hall and Wiseman, 2012; Berry et al., 2012].

In both cases, it appears that a reconsideration of the term "Heisenberg limit" is underway within the scientific community, and a move away from the 2007 definition. Although we never took active part in the theoretical debate, humbly we are happy to think that our experiment pushed this change of point of view.

Finally, to conclude with some humor, I can not avoid to mention here the thread "Heisenberg Limit Broken", posted in

march 2011 on a forum about philosophical questions,[1] which I found while searching for comments on our experiment in the web. The entry reported below, signed by the anonymous user Uno, does not need further comments. It says "Trust me, please - if someone really disproves Heisenberg's Principle, this would be a theoretician with a pen and paper, not just a group of ambitious *majos* bombarding the "atoms" with photons from a Chinese laser pointer. Spain does not have any serious research centre, their scientists are mostly involved with studying olive oil and wine production."

[1] http://forums.philosophyforums.com/threads/heisenberg-limit-broken-46558.html

Bibliography

Appel, J., MacRae, A., and Lvovsky, A. I. (2009). A versatile digital GHz phase lock for external cavity diode lasers. *Measurement Science and Technology*, 20(5):055302.

Bachor, H.-A. and Ralph, T. C. (2004). *A Guide to Experiments in Quantum Optics*. Wiley-VCH.

Barker, L. M. (1972). Laser interferometry in shock-wave research. *Experimental Mechanics*, 12(5):209–215.

Baudon, J., Mathevet, R., and Robert, J. (1999). Atomic interferometry. *Journal of Physics B: Atomic, Molecular and Optical Physics*, 32(15):R173–R195.

Beduini, F. A. and Mitchell, M. W. (2013). Optical spin squeezing: bright beams as high-flux entangled photon sources. *arXiv:quant-ph*, page 1303.5257.

Beltrán, J. and Luis, A. (2005). Breaking the Heisenberg limit with inefficient detectors. *Phys. Rev. A*, 72(4):045801.

Berry, D. W., Hall, M. J. W., Zwierz, M., and Wiseman, H. M. (2012). Optimal Heisenberg-style bounds for the average performance of arbitrary phase estimates. *Phys. Rev. A*, 86:053813.

Boixo, S., Datta, A., Davis, M., Flammia, S., Shaji, A., and Caves, C. (2008a). Quantum metrology: Dynamics versus entanglement. *Phys. Rev. Lett.*, 101(4):040403.

Boixo, S., Datta, A., Davis, M. J., Shaji, A., Tacla, A. B., and Caves, C. M. (2009). Quantum-limited metrology and Bose-Einstein condensates. *Phys. Rev. A*, 80:032103.

Boixo, S., Datta, A., Flammia, S., Shaji, A., Bagan, E., and Caves, C. (2008b). Quantum-limited metrology with product states. *Phys. Rev. A*, 77(1):012317.

Boixo, S., Flammia, S., Caves, C., and Geremia, J. (2007). Generalized limits for single-parameter quantum estimation. *Phys. Rev. Lett.*, 98(9):090401.

Bordé, C. J. (1989). Atomic interferometry with internal state labelling. *Physics Letters A*, 140(1–2):10–12.

Boto, A. N., Kok, P., Abrams, D. S., Braunstein, S. L., Williams, C. P., and Dowling, J. P. (2000). Quantum interferometric optical lithography: Exploiting entanglement to beat the diffraction limit. *Phys. Rev. Lett.*, 85(13):2733–2736.

Braginsky, V. B. and Khalili, F. Y. (1992). *Quantum Measurement*. Cambridge University Press.

Braunstein, S. L. (1994). Some limits to precision phase measurement. *Phys. Rev. A*, 49:69–75.

Braunstein, S. L. and Caves, C. M. (1994). Statistical distance and the geometry of quantum states. *Phys. Rev. Lett.*, 72:3439–3443.

Braunstein, S. L., Caves, C. M., and Milburn, G. J. (1996). Generalized uncertainty relations: Theory, examples, and Lorentz invariance. *Annals of Physics*, 247(1):135–173.

Carr, S. M., Lawrence, W. E., and Wybourne, M. N. (2001). Accessibility of quantum effects in mesomechanical systems. *Phys. Rev. B*, 64:220101.

Carruthers, P. and Nieto, M. M. (1968). Phase and angle variables in quantum mechanics. *Rev. Mod. Phys.*, 40:411–440.

Caves, C. M. (1980). Quantum-mechanical radiation-pressure fluctuations in an interferometer. *Phys. Rev. Lett.*, 45:75–79.

Caves, C. M. (1981). Quantum-mechanical noise in an interferometer. *Phys. Rev. D*, 23(8):1693–1708.

Caves, C. M. (1985). Defense of the standard quantum limit for free-mass position. *Phys. Rev. Lett.*, 54:2465–2468.

Chase, B. A., Baragiola, B. Q., Partner, H. L., Black, B. D., and Geremia, J. M. (2009). Magnetometry via a double-pass continuous quantum measurement of atomic spin. *Phys. Rev. A*, 79:062107.

Chaste, J., Eichler, A., Moser, J., Ceballos, G., Rurali, R., and Bachtold, A. (2012). A nanomechanical mass sensor with yoctogram resolution. *Nat Nano*, 7(5):301–304.

Cohen-Tannoudji, C., Dupont-Roc, J., and Grynberg, G. (1992). *Atom-Photon Interaction.* John Wiley & Sons, Inc., New York.

Crepaz, H. (2007). *Trapping and cooling rubidium atoms for quantum information.* PhD thesis, Leopold-Franzens-Universitat Innsbruck.

Cronin, A. D., Schmiedmayer, J., and Pritchard, D. E. (2009). Optics and interferometry with atoms and molecules. *Rev. Mod. Phys.*, 81(3):1051–1129.

D'Ariano, G. M. and Paris, M. G. A. (1994). Lower bounds on phase sensitivity in ideal and feasible measurements. *Phys. Rev. A*, 49:3022–3036.

de Echaniz, S. R., Koschorreck, M., Napolitano, M., Kubasik, M., and Mitchell, M. W. (2008). Hamiltonian design in atom-light interactions with rubidium ensembles: A quantum-information toolbox. *Phys. Rev. A*, 77:032316.

Dembo, A., Cover, T., and Thomas, J. (1991). Information theoretic inequalities. *Information Theory, IEEE Transactions on*, 37(6):1501 –1518.

Deutsch, I. H. and Jessen, P. S. (2010). Quantum control and measurement of atomic spins in polarization spectroscopy. *Optics Communications*, 283(5):681–694.

Dirac, P. A. M. (1927). The quantum theory of the emission and absorption of radiation. *Proceedings of the Royal Society of London. Series A*, 114(767):243–265.

Donley, E. A., Heavner, T. P., Levi, F., Tataw, M. O., and Jefferts, S. R. (2005). Double-pass acousto-optic modulator system. *Rev. Sci. Instr.*, 76:063112.

Dorner, U., Demkowicz-Dobrzanski, R., Smith, B. J., Lundeen, J. S., Wasilewski, W., Banaszek, K., and Walmsley, I. A. (2009). Optimal quantum phase estimation. *Phys. Rev. Lett.*, 102:040403.

Dowling, J. P. (1998). Correlated input-port, matter-wave interferometer: Quantum-noise limits to the atom-laser gyroscope. *Phys. Rev. A*, 57:4736–4746.

Erbe, A., Krömmer, H., Kraus, A., Blick, R. H., Corso, G., and Richter, K. (2000). Mechanical mixing in nonlinear nanomechanical resonators. *Applied Physics Letters*, 77(19):3102–3104.

Essen, L. and Parry, J. V. L. (1955). An atomic standard of frequency and time interval: A cæsium resonator. *Nature*, 176:280–282.

Foot, C. J. (2005). *Atomic Physics*. Oxford University Press.

Geremia, J. M., Stockton, J. K., and Mabuchi, H. (2006). Tensor polarizability and dispersive quantum measurement of multilevel atoms. *Phys. Rev. A*, 73(4):042112.

Giovannetti, V. (2004). Quantum-enhanced measurements: Beating the standard quantum limit. *Science*, 306(5700):1330–1336.

Giovannetti, V., Lloyd, S., and Maccone, L. (2006). Quantum metrology. *Phys. Rev. Lett.*, 96(1):010401.

Grimm, R., Weidemueller, M., and Ovchinnikov, Y. (2000). Optical dipole traps for neutral atoms. *Adv. At. Mol. Opt. Phys.*, 42:95–172.

Hall, M. J. W., Berry, D. W., Zwierz, M., and Wiseman, H. M. (2012). Universality of the Heisenberg limit for estimates of random phase shifts. *Phys. Rev. A*, 85:041802.

Hall, M. J. W. and Wiseman, H. M. (2012). Does nonlinear metrology offer improved resolution? answers from quantum information theory. *Phys. Rev. X*, 2:041006.

Hammerer, K., Sorensen, A. S., and Polzik, E. S. (2010). Quantum interface between light and atomic ensembles. *Rev Mod Phys*, 82(2):1041–1093.

Hariharan, P. and Sanders, B. (1996). Quantum phenomena in optical interferometry. *Prog Optics*, 36:49–128.

Hedrick, E. R. (1913). A direct definition of logarithmic derivative. *The American Mathematical Monthly*, 20(6):pp. 185–187.

Heisenberg, W. (1927). Über den anschaulichen inhalt der quantentheoretischen kinematik und mechanik. *Zeitschrift für Physik A Hadrons and Nuclei*, 43(3):172–198.

Helstrom, C. and Kennedy, R. (1974). Noncommuting observables in quantum detection and estimation theory. *Information Theory, IEEE Transactions on*, 20(1):16 – 24.

Helstrom, C. W. (1976). *Quantum Detection and Estimation Theory*. Academic Press - New York.

Heslehurst, R. B. (2009). A review of holographic interferometry investigations of defects and damage in composite materials. *Journal of Advanced Materials*, 41(1):5–12.

Holevo, A. S. (1982). *Probabilistic and Statistical Aspects of Quantum Theory*. North-Holland - Amsterdam.

Holland, M. J. and Burnett, K. (1993). Interferometric detection of optical phase shifts at the Heisenberg limit. *Phys. Rev. Lett.*, 71:1355–1358.

Hong, C. K., Ou, Z. Y., and Mandel, L. (1987). Measurement of subpicosecond time intervals between two photons by interference. *Phys. Rev. Lett.*, 59:2044–2046.

Jozsa, R. (1994). Fidelity for mixed quantum states. *Journal of Modern Optics*, 41:2315–2323.

Kasevich, M. and Chu, S. (1991). Atomic interferometry using stimulated Raman transitions. *Phys. Rev. Lett.*, 67:181–184.

Kitagawa, M. and Ueda, M. (1993). Squeezed spin states. *Phys. Rev. A*, 47(6):5138–5143.

Klein, D. J. (1974). Degenerate perturbation theory. *Journal of Chemical Physics*, 61(3):786–798.

Korolkova, N., Leuchs, G., Loudon, R., Ralph, T. C., and Silberhorn, C. (2002). Polarization squeezing and continuous-variable polarization entanglement. *Phys. Rev. A*, 65:052306.

Koschorreck, M. (2011). *Generation of Spin Squeezing in an Ensemble of Cold Rubidium 87*. PhD thesis, ICFO - UPC.

Koschorreck, M. and Mitchell, M. W. (2009). Unified description of inhomogeneities, dissipation and transport in quantum light–atom interfaces. *Journal of Physics B: Atomic, Molecular and Optical Physics*, 42(19):195502.

Koschorreck, M., Napolitano, M., Dubost, B., and Mitchell, M. W. (2010a). Quantum nondemolition measurement of large-spin ensembles by dynamical decoupling. *Phys. Rev. Lett.*, 105:093602.

Koschorreck, M., Napolitano, M., Dubost, B., and Mitchell, M. W. (2010b). Sub-projection-noise sensitivity in broadband atomic magnetometry. *Phys. Rev. Lett.*, 104:093602.

Koschorreck, M., Napolitano, M., Dubost, B., and Mitchell, M. W. (2011). High resolution magnetic vector-field imaging with cold atomic ensembles. *Applied Physics Letters*, 98(7):074101.

Kozinsky, I., Postma, H. W. C., Kogan, O., Husain, A., and Roukes, M. L. (2007). Basins of attraction of a nonlinear nanomechanical resonator. *Phys. Rev. Lett.*, 99:207201.

Kubasik, M. (2009). *Towards Spin Squeezing in Cold Atomic Ensembles*. PhD thesis, ICFO - UPC.

Kupriyanov, D. V., Mishina, O. S., Sokolov, I. M., Julsgaard, B., and Polzik, E. S. (2005). Multimode entanglement of light and atomic ensembles via off-resonant coherent forward scattering. *Phys. Rev. A*, 71:032348.

Lane, A. S., Braunstein, S. L., and Caves, C. M. (1993). Maximum-likelihood statistics of multiple quantum phase measurements. *Phys. Rev. A*, 47:1667–1696.

Loudon, R. (1983). *The quantum theory of light*. Clarendon Press, Oxford, 2 edition.

Louisell, W. (1963). Amplitude and phase uncertainty relations. *Physics Letters*, 7(1):60–61.

Luis, A. (2004). Nonlinear transformations and the Heisenberg limit. *Phys Lett A*, 329(1-2):8–13.

Luis, A. (2007). Quantum limits, nonseparable transformations, and nonlinear optics. *Phys. Rev. A*, 76(3):035801.

Maji, A. K. (1995). Review of noninvasive techniques for detecting microfracture. *Advanced Cement Based Materials*, 2(5):201–209.

Mandelstam, L. and Tamm, I. G. (1945). The uncertainty relation between energy and time in non-relativistic quantum mechanics. *J. Phys. USSR*, 9(4):249.

Messiah, A. (1999). *Quantum Mechanics*. Dover Publications.

Metcalf, H. J. and van der Straten, P. (1999). *Laser Cooling and Trapping*. Springer.

Mitchell, M. W. (2009). Parametric down-conversion from a wave-equation approach: Geometry and absolute brightness. *Phys. Rev. A*, 79:043835.

Mølmer, K. and Madsen, L. B. (2004). Estimation of a classical parameter with Gaussian probes: Magnetometry with

collective atomic spins. *Phys Rev A*, 70(5):052102.

Ou, Z. Y. (1996). Complementarity and fundamental limit in precision phase measurement. *Phys. Rev. Lett.*, 77:2352–2355.

Ozawa, M. (1988). Measurement breaking the standard quantum limit for free-mass position. *Phys. Rev. Lett.*, 60:385–388.

Pegg, D. T. and Barnett, S. M. (1988). Unitary phase operator in quantum mechanics. *EPL (Europhysics Letters)*, 6(6):483.

Pezzé, L. and Smerzi, A. (2008). Mach-Zehnder interferometry at the Heisenberg limit with coherent and squeezed-vacuum light. *Phys. Rev. Lett.*, 100:073601.

Robertson, H. P. (1929). The uncertainty principle. *Phys. Rev.*, 34:163–164.

Sakurai, J. (1994). *Modern Quantum Mechanics*. Addison-Wesley Publishing Company, Inc., rev. edition.

Saleh, B. E. A. and Teich, M. C. (2001). *Photon Optics*. John Wiley & Sons, Inc.

Sanders, B. C. and Milburn, G. J. (1995). Optimal quantum measurements for phase estimation. *Phys. Rev. Lett.*, 75:2944–2947.

Sarma, G., Silberfarb, A., and Mabuchi, H. (2008). Quantum stochastic calculus approach to modeling double-pass atom-field coupling. *Phys. Rev. A*, 78:025801.

Schottky, W. (1918). Über spontane stromschwankungen in verschiedenen elektrizitätsleitern. *Annalen der Physik*, 362(23):541–567.

Schulz, M. (2002). *Tightly confined atoms in optical dipole traps*. PhD thesis, Leopold-Franzens-Universitat Innsbruck.

Scully, M. O. and Zubairy, M. S. (1997). *Quantum Optics*. Cambridge University Press.

Sewell, R. J., Koschorreck, M., Napolitano, M., Dubost, B., Behbood, N., and Mitchell, M. W. (2012). Magnetic sensitivity beyond the projection noise limit by spin squeezing. *Phys. Rev. Lett.*, 109:253605.

Sorensen, A. S. and Mølmer, K. (2001). Entanglement and extreme spin squeezing. *Phys. Rev. Lett.*, 86(20):4431–4434.

Steck, D. A. (2009). Rubidium 87 D line data.

Stockton, J. K. (2007). *Continuous Quantum Measurement of Cold Alkali-Atom Spins*. PhD thesis, California Institute of

Technology Pasadena, California.

Sullivan, D. (2001). Time and frequency measurement at nist: the first 100 years. In *Frequency Control Symposium and PDA Exhibition, 2001. Proceedings of the 2001 IEEE International*, pages 4–17.

Tan, S. M. (1999). A computational toolbox for quantum and atomic optics. *Journal of Optics B: Quantum and Semiclassical Optics*, 1(4):424.

The Ligo Scientific Collaboration (2011). A gravitational wave observatory operating beyond the quantum shot-noise limit. *Nat Phys*, 7(12):962–965.

Torgerson, J. R. and Mandel, L. (1996). Is there a unique operator for the phase difference of two quantum fields? *Phys. Rev. Lett.*, 76:3939–3942.

Vorontsov, Y. I. and Rembovsky, Y. A. (1999). The problem of the Pegg-Barnett phase operator. *Physics Letters A*, 254(1–2):7–10.

Wolfgramm, F., Cerè, A., Beduini, F. A., Predojević, A., Koschorreck, M., and Mitchell, M. W. (2010). Squeezed-light optical magnetometry. *Phys. Rev. Lett.*, 105:053601.

Wolfgramm, F., Vitelli, C., Beduini, F. A., Godbout, N., and Mitchell, M. W. (2013). Entanglement-enhanced probing of a delicate material system. *Nat Photon*, 7(1):28–32.

Woodruff, S. D. and Yeung, E. S. (1982). Refractive-index and absorption detector for liquid-chromatography based on fabry-perot interferometry. *Analytical Chemistry*, 54(7):1174–1178.

Woolley, M. J., Milburn, G. J., and Caves, C. M. (2008). Nonlinear quantum metrology using coupled nanomechanical resonators. *New J Phys*, 10:125018.

Yuen, H. and Lax, M. (1973). Multiple-parameter quantum estimation and measurement of nonselfadjoint observables. *Information Theory, IEEE Transactions on*, 19(6):740 – 750.

Yuen, H. P. (1983). Contractive states and the standard quantum limit for monitoring free-mass positions. *Phys. Rev. Lett.*, 51:719–722.

Zwierz, M., Pérez-Delgado, C. A., and Kok, P. (2010). General optimality of the Heisenberg limit for quantum metrology.

Phys. Rev. Lett., 105:180402.

Zwierz, M., Pérez-Delgado, C. A., and Kok, P. (2012). Ultimate limits to quantum metrology and the meaning of the Heisenberg limit. *Phys. Rev. A*, 85:042112.

List of publications

Work on nonlinear quantum metrology:
Napolitano, M. and Mitchell, M. W. (2010). Nonlinear metrology with a quantum interface. *New J Phys*, 12:093016. (Contents presented in Chapter 3 of this dissertation)

Napolitano, M., Koschorreck, M., Dubost, B., Behbood, N., Sewell, R. J., and Mitchell, M. W. (2011). Interaction-based quantum metrology showing scaling beyond the Heisenberg limit. *Nature*, 471(7339):486–489. (Contents presented in Chapters 4,5 and 6 of this dissertation)

Work on linear quantum metrology:
de Echaniz, S. R., Koschorreck, M., Napolitano, M., Kubasik, M., and Mitchell, M. W. (2008). Hamiltonian design in atom-light interactions with rubidium ensembles: A quantum information toolbox. *Phys. Rev. A*, 77:032316.

Kubasik, M., Koschorreck, M., Napolitano, M., de Echaniz, S. R., Crepaz, H., Eschner, J., Polzik, E. S., and Mitchell, M. W. (2009). Polarization-based light-atom quantum interface with an all-optical trap. *Phys. Rev. A*, 79:043815.

Koschorreck, M., Napolitano, M., Dubost, B., and Mitchell, M. W. (2010b). Sub-projection-noise sensitivity in broadband atomic magnetometry. *Phys. Rev. Lett.*, 104:093602.

Koschorreck, M., Napolitano, M., Dubost, B., and Mitchell, M. W. (2010a). Quantum nondemolition measurement of large-spin ensembles by dynamical decoupling. *Phys. Rev. Lett.*,

105:093602.

Sewell, R. J., Koschorreck, M., Napolitano, M., Dubost, B., Behbood, N., and Mitchell, M. W. (2012). Magnetic sensitivity beyond the projection noise limit by spin squeezing. *Phys. Rev. Lett.*, 109:253605.

Work on quantum non-demolition measurement:
Mitchell, M. W., Koschorreck, M., Kubasik, M., Napolitano, M., and Sewell, R. J. (2012). Certified quantum non-demolition measurement of material systems. *New Journal of Physics*, 14(8):085021.

Sewell, R. J., Napolitano, M., Behbood, N., Colangelo, G., and Mitchell, M. W. (2013). Certified quantum non-demolition measurement of a macroscopic material system. *Nat Photon*, 7(7):517–520.

Work on magnetometry:
Koschorreck, M., Napolitano, M., Dubost, B., and Mitchell, M. W. (2011). High resolution magnetic vector-field imaging with cold atomic ensembles. *Applied Physics Letters*, 98(7):074101.

Behbood, N., Martin Ciurana, F., Colangelo, G., Napolitano, M., Mitchell, M. W., and Sewell, R. J. (2013b). Real-time vector field tracking with a cold-atom magnetometer. *Applied Physics Letters*, 102(17):173504.

Work on other topics:
Dubost, B., Koschorreck, M., Napolitano, M., Behbood, N., Sewell, R. J., and Mitchell, M. W. (2012). Efficient quantification of non-Gaussian spin distributions. *Phys. Rev. Lett.*, 108:183602.

Behbood, N., Colangelo, G., Martin Ciurana, F., Napolitano, M., Sewell, R. J., and Mitchell, M. W. (2013a). Feedback cooling of an atomic spin ensemble. *Phys. Rev. Lett.*, 111:103601.